SANDIA REPORT
SAND2001-2944
Unlimited Release
Printed September 2001

AC-Current Burn-Through of 13-mm-Thick Aluminum and Steel

Douglas H. Loescher

Prepared by
Sandia National Laboratories
Albuquerque, New Mexico 87185 and Livermore, California 94550

Sandia is a multiprogram laboratory operated by Sandia Corporation, a Lockheed Martin Company, for the United States Department of Energy under Contract DE-AC04-94AL85000.

Sandia National Laboratories

Issued by Sandia National Laboratories, operated for the United States Department of Energy by Sandia Corporation.

Available to DOE and DOE contractors from
U.S. Department of Energy
Office of Scientific and Technical Information
P.O. Box 62
Oak Ridge, TN 37831

Telephone: (865)576-8401
Facsimile: (865)576-5728
E-Mail: reports@adonis.osti.gov
Online ordering: http://www.doe.gov/bridge

Available to the public from
U.S. Department of Commerce
National Technical Information Service
5285 Port Royal Rd
Springfield, VA 22161

Telephone: (800)553-6847
Facsimile: (703)605-6900
E-Mail: orders@ntis.fedworld.gov
Online order: http://www.ntis.gov/ordering.htm

SAND2001-2944
Unlimited Release
Printed September 2001

AC-Current Burn-Through of 13-mm-Thick Aluminum and Steel

Douglas H. Loescher
System Surety Assessment Department
Sandia National Laboratories
P.O. Box 5800
Albuquerque, New Mexico 87185-0830

Abstract

Cases and containers made of aluminum or steel are used to protect explosive components. It is possible in an accident that the cases and containers could contact parts of an ac power system. If such contact occurred, tens of kiloamperes of current might flow for tens to hundreds of milliseconds. This report shows that currents in the 20-to-40 kiloampere range lasting for tens to hundreds of milliseconds burned through both aluminum and steel with thickness up to 13 mm. Analyses of arc-to-metal heat transfer and experimental results are given.

Contents

Figures

Tables

Nomenclature

DoD	U.S. Department of Defense
DOE	U.S. Department of Energy
VNIIEF	Russian Federal Nuclear Institute for Experimental Physics

1. Summary

Cases and containers made from aluminum or steel are used to contain and protect explosive components. Various alloys and wall thicknesses up to at least 12.7 mm (one-half inch) are in use.

Electric power lines and other electric power equipment such as transformers and switch gear are located along transportation routes, at manufacturing and maintenance sites, and at various sites controlled by the U.S. Department of Energy (DOE) or the U.S. Department of Defense (DoD). In an accident, a case or container might be exposed to a power line or some other part of a power system. Loescher and Duran (1997) discussed electric power challenges to explosive safety. Their report points out that currents of tens of kiloamperes might flow for tens to hundreds of milliseconds between power sources and cases or containers.

Analyses and experiments were conducted to investigate ac current burn-through of 13-mm-thick aluminum and steel. Much of the work was done in cooperation with researchers at the Russian Federal Nuclear Institute for Experimental Physics (the Russian name leads to the acronym VNIIEF). Cooperation with VNIEEF provided access to special expertise and needed equipment. The analyses showed that important phenomena include arc stability, arc heating, and magnetic pressure. Six high-current burn-through-of-aluminum experiments and six high-current burn-through-of-steel experiments were conducted. Burn-through of 13-mm-thick aluminum was observed after 52 milliseconds, when the current was 19.4 kA. Burn-through of steel was observed after 125 milliseconds, when the current was 36.9 kA.

This report includes, in appendices A, B, and C, three reports submitted by VNIIEF.

2. Introduction

Aluminum and steel with thickness up to 13 mm are used by DOE as barriers to protect explosive components from unintended energy. Shipping containers and ordnance cases are examples of such barriers. As the result of an accident, a metallic barrier could contact electrical power conductors. Electric power challenges to nuclear explosive safety were discussed by Loescher and Duran (1997). They reported that fault currents of tens of kiloamperes could be available at the low-voltage side of secondary distribution transformers. When they wrote their report, they did not have data on the damage that such large currents could do to metallic barriers. This report provides information on the damage that could result from arcing between a source of high current and a metallic barrier.

Section 3 provides information on power systems and on the possibility of contact between ac power apparatus and cases or containers. Section 4, Cooperative Program with VNIIEF, describes work done under contract by VNIIEF. Researchers at VNIIEF submitted three reports (Appendices A, B, and C). The section provides a guide to the contents of these reports. The final two sections of this report discusses the results obtained and conclusions.

The author was the technical advisor for the contract placed with VNIIEF. Much of the work described in this report was done at VNIIEF. This report was written to ensure that a record of the work done at VNIIEF would be available in the library at Sandia National Laboratories.

3. Background

Many DOE explosive components have outer metal cases, and many are shipped and stored in metal containers. For most cases and containers, the metal is either aluminum or steel, and the wall thickness is less than 13 mm. Cases and containers do not normally come in contact with sources of electric current. However, contact might occur as the result of an accident.

An electric power system can be partitioned into facilities and equipment that have the principal functions of generation, transmission, sub-transmission, primary distribution, secondary distribution, and usage (Figure 1).

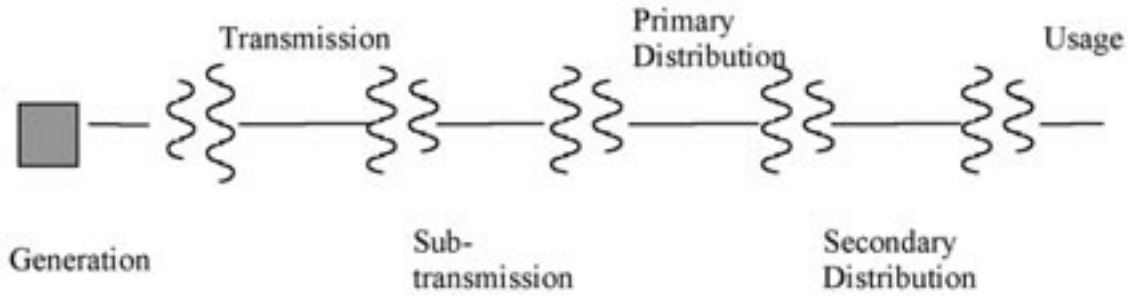

Figure 1. Partitioning of power systems.

Accidental contact between a DOE case or container and electric energy at a power-generation site is extremely unlikely because these DOE items are not transported through such sites.

Electric energy is most often transmitted from a generation facility at high voltages; the most common voltages are greater than 100 kV. For example, electric power is brought into the Albuquerque area at 115 kV and 345 kV. High-voltage lines are strung from tall towers or frames that are placed well away from the edges of roads. The frames used to transport power onto Kirtland Air Force Base at 345 kV are shown in Figure 2. Wherever possible, the DOE uses transport routes that follow interstate highways. Most high-voltage power lines are routed perpendicular to or well away from such highways. Even if a power line were to fall, the walls of transport vehicles would isolate cases and containers from electric power. For these reasons, accidental contact with high-voltage power lines because of a motor vehicle accident is unlikely. Contact might occur as the result of an aircraft accident because such accidents are most likely during take off or landing and because there can be power lines near the ends of runways.

Figure 2. High-voltage transmission lines on Kirtland Air Force Base.

High voltages used for transmission of electric power are stepped down to lower distribution level voltages at substations. Distribution level voltages range from a few kilovolts to a few tens of kilovolts. The level of 12,470 V is used extensively within Sandia National Laboratories sites, on Kirtland Air Force Base, and at the DOE Pantex plant. The level of 4600 V is common in older systems. Distribution wiring may be placed on single poles that are located close to the edge of roads. This is shown in Figure 3. It is credible that a vehicle transporting cases or containers could slide into a power pole located only a few feet from the edge of pavement.

Figure 3. Distribution-level power lines on Kirtland Air Force Base.

Distribution wiring on industrial and military sites often connects to transformers that step the voltage down to 480 V. Such transformers are used to supply power to industrial and commercial buildings. On a military base, such transformers might be used to supply power to offices, maintenance buildings, shopping centers, or fast food restaurants. Along transportation routes, one might be found at a truck-refueling plaza. The transformers are commonly located outside of buildings, but close to them. When in cabinets, such transformers are not considered a significant threat to public safety, and therefore, they are usually not placed behind fences or other barricades. Two cabinets that contain such transformers and two that contain switches are shown in Figure 4; the cabinets are located at Sandia National Laboratories just west of Building 836. Metal cabinets isolate the transformers from casual contact, but could be torn open if hit by a truck.

Figure 4. Cabinets for 480-V service transformers.

The principal threat from 480-V service transformers is the high current available to a short circuit across the output terminals. Representative values are shown in Table 1. These currents are up to two hundred times the currents used to arc weld 13-mm-thick aluminum or steel. Table 1 shows the current that could flow if the short circuit were at the output terminals of the transformer, and it shows the current that could flow if the short circuit were 100 feet away from these terminals. The assumed size of the wire between the transformer and the 100-foot distant short is shown in the table. Contact at a transformer could occur if a protective cabinet were torn open during an accident. Contact some distance from a transformer could occur if high-current wiring became exposed during an accident.

Loescher and Duran (1997) explain that circuit breakers and other protective equipment are designed to clear faults in tens of milliseconds to a few hundred milliseconds. The exact time depends on the fault current and design of the circuit breaker. They point out that power might be reconnected to a fault one or more times through the action of re-closers. (A re-closer reconnects power to a circuit after a specified interval. They are used in power systems because some faults, such as those caused by wind-blown tree limbs, clear themselves).

Table 1. Short-circuit currents for 480-V transformers (from Loescher and Duran 1977, Table 2).

Transformer Rating (Number and size of copper wires between transformer and fault)	**Distance to Fault**	**Fault Current**
225 kVA rms (1 @ 0.5 inch diam.)	0 (at transformer) 100 ft	7.5 kA rms 6.6 kA rms
750 kVA rms (2 @ 0.5 inch diam.)	0 (at transformer) 100 ft	20.5 kA rms 17.5 kA rms
1.5 MVA rms (2 @ 0.71 inch diam.)	0 (at transformer) 100 ft	40.0 kA rms 31.6 kA rms

The brief examination of power systems has shown that currents of tens of kiloamperes could be available for tens to hundred of milliseconds at or near the output terminals of 480-V transformers. It was also shown that such transformers are relatively common and not always protected against vehicle impact.

Contact between a case or container and a source of power could be direct metal-to-metal contact or arcing contact. More damage is expected from arcing contact because a high-current electric arc is a source of large amounts of heat. The voltage drop across an arc is approximately independent of the current. A reasonable initial estimate of the voltage is 100 V. Lower voltage drop and, therefore, less power and less heat flux are expected at a metal-to-metal contact.

The damage that a high current arc might do can be estimated. Welding engineers estimate that 10% to 20% of the power in an arc is transferred to the metal to be welded. Make the following assumptions: the current is 20 kA, the voltage drop is 100 V, 10% of the power is transferred as heat flux, and the material is aluminum. For these assumptions, the heat flux is 200 kilowatts. The specific heat of aluminum is about 900 joules per kilogram-degree centigrade, and the melting temperature is about 500˚C. The exact value of the specific heat depends on the temperature, and the exact melting temperature depends on the alloy. Exact values are not needed for this discussion. For the values given, approximately 400 grams (a little less than one pound) of aluminum would be melted in 1 second. A 2-inch-diameter by 0.5-inch-thick plug of aluminum weighs about 36 grams. The assumed heat flux would provide the energy required to melt this amount of aluminum in less than 100 milliseconds.

The energy-balance calculations show that there might be enough energy for burn-through. They provide no insight into the geometric and other conditions for which it would occur. The author knows of no published information, other than this report, on arcs and burn-through that applies to the conditions of interest.

Before a study of burn-through could be conducted, the importance of case or container contents had to be determined. Dean Dobranich of the Fluid and Thermal Analysis Department (Dobranich 1996) provided essential judgement. He pointed out that because the time of heating would be at most a few hundred milliseconds, there would be very little heat transfer between the metal walls of a case or container and its contents right up to the time of burn-through. His judgement was confirmed by results, reported later in this report, from experiments on hollow cylinders that simulated cases or containers.

4. Cooperative Program with VNIIEF

Although there was interest in environments that could challenge the safety of cases and containers, there was no funding to do a burn-through study at Sandia, or to pay for tests at a domestic test facility. Staff at one facility estimated that testing would cost at least $5,000 per day. Furthermore, they pointed out that work on burn-through would be different from the work usually done at the facility and, therefore, might be much more expensive. Along with the lack of money, there was was a lack of experience with electric arcs. The author did not have the technical knowledge required to plan and conduct burn-through tests.

While looking for away to proceed, the author mentioned his needs to a program manager for cooperative programs between the United States and Russia. The U.S. Congress had set aside money for cooperative programs between DOE laboratories and Russian nuclear laboratories. The program manager introduced the author to two researchers at VNIIEF, Dr. Boris Skripnik, the senior member of the team, and Dr. Nicolai Prudkoi, who were interested in the work and who had experience with electric arcs. These researchers also had access to test equipment located at the All Russia Electrotechnical Institute. After discussions with Skripnik and Prudkoi and after obtaining a commitment of financial support, the author submitted a Request-for-Quote to VNIIEF. After some negotiation, a contract was placed for a study of burn-through. Drawings and visual aids were submitted for classification review and were approved as unclassified before they were presented to the Russian team. The author learned that all material provided by the Russian team underwent an equally rigorous classification review by authorities at VNIIEF.

The work was divided into five tasks. Task 1 was to provide a detailed plan for analyses and experiments. Task 2 was divided into Subtasks 2A and 2B. Subtask 2A, required that the researchers assemble and report information that was needed to design experiments. Subtask 2B required that the researchers investigate and report on the relation between damage and parameters such as electric current and electrode-to-cylinder spacing. Task 3 was to conduct experiments, and Task 4 was to compare results with expectations derived in Task 2. Task 5 was to prepare and deliver a final report.

In accordance with the provisions of the contract, Skripnik and Prudkoi prepared three reports. The first two reports were required by Subtasks 2A and 2B, and the third and final report was required by Task 5. The contents of these reports, which are reproduced in Appendices A, B, and C, respectively, are discussed below.

Subtask 2A Report (Appendix A)

A copy of the report submitted to complete this subtask is contained in Appendix A. The report addresses four principal topics: arc stability, current source, temperature measurement, and design of experimental fixtures.

Section 1 of the report addresses the stability of arcs between 20-mm-diameter copper electrodes and cylinders of aluminum or steel. The diameter of the copper electrode was chosen to approximate the diameter of electrical connections on transformers. Skripnik and Prudkoi calculated that for a current of 30 kiloamperes and a time of 0.3 second, the end of the electrode would recede by 23 mm. If the electrode nearly touched the cylinder at the beginning of the arc event, the total arc length would be about 36 mm if burn-through occurred near the end of the interval. The value of 36 mm is the sum of the distance that the end of the electrode would move away from the surface, 23 mm, and the thickness of the metal removed, 13 mm. They concluded that an arc of this length would not be stable; that is, it would move away from the initial strike point. In fact, they concluded it would move until the arc length became so long that the arc would extinguish. The author does not know enough about the behavior of arcs to comment on the correctness of the analyses done by Skripnik and Prudkoi. The analyses led to an experimental design, described in Section 4 of their report, that produced stable arcs.

Sections 2 and 3 of the Subtask 2A Report describe work done to select a source of ac impulse current and the method used to measure temperature. Section 4 describes the experimental fixture designed to assure a stable arc attachment point.

Subtask 2B Report (Appendix B)

In the Subtask 2B Report, Skripnik and Prudkoi show that an arc to a flat plate is a good approximation to an arc to a cylinder with an outer diameter of 30 cm and 13-mm-thick walls. This obtains because the estimated lateral dimensions of arcs and the thickness are small compared to the diameter.

They show that heat input from the arc will be much greater than heat input from resistive losses in the metal. They introduce a way to treat the arc as a heat source. In particular, they assert from references in Russian publications that the radius of the arc will be approximately proportional to the square root of the current (Equation 2.8 in the Subtask 2B Report). This result is equivalent to stating that the current density is approximately constant in arcs between a given anode and a given cathode. In Equation 2.9 of the report, they provide values for the constant of proportionality.[1]

---

[1] The value shown in the report with a superscript plus ($^+$) refers to the cylinder at positive potential with respect to the copper electrode.

They further assert that the heat flux from the arc will be proportional to the area of the arc, and they provide values for the constant of proportionality between heat flux and arc area (Equation 2.11 in Subtask 2B Report).[2] The assertion that the arc area is proportional to the current and the assertion that heat flux is proportional to arc area combine to an assertion that heat flux is proportional to arc current.

If the equations and constants of proportionality for arc area and heat flux per unit area are combined, one obtains q^+ equal to 8 watts per ampere and q^- equal to 11 watts per ampere. The quantities q^+ and q^- are defined on page 7 of the report. These are close to the result of 10 watts per ampere obtained for assumptions that the arc voltage drop is 100 V and that 10% of the arc power goes into heating metal. The agreement does not mean either is correct, but it does increase confidence. The calculation results in q^+ smaller than q^-,which is inconsistent with the information given in Equation 2.11 of the report. It is also inconsistent with information from a welding engineer (Knorovsky 2001), who reported that greatest heating occurs when metal being welded is at positive potential with respect to the welding electrode. The author does not have an explanation for the discrepancy but thinks it possible that the values listed for k^+ and k^- in Equation 2.9 were reversed. In any case, it is expected that the most heat will be deposited when the cylinder is at positive potential with respect to the copper electrode.

In Section 3 of the Subtask 2B Report, they examine one-dimensional and three-dimensional solutions for arc-to-plate heat transfer. They show close agreement between results from the two methods.

In Section 4 of the Subtask 2B report, they present a thermal model that includes loss of material as the arc burns through the plate. They state early in this section that loss of material will be driven by strong electrodynamic forces. They use the model to calculate times of burn-through for a range of assumptions on the melt temperature and temperature at which the metal is removed. Results are given in Table 4.2 of their report (see Appendix B, Table 4.2).[3] They also used the model to calculate the temperature profiles shown in Figure 4.1 of their report. Figure 5 is a copy of this figure. It is seen in Figure 5 that their model predicts steep temperature profiles. For example, the model predicts that the metal only 2-mm behind the arc front will be only slightly above the initial temperature. This same prediction is shown in a different way in Figure 6, which is a copy of Figure 4.2 from the report. It is seen in Figure 6 that the temperature at the back surface of the plate remains almost constant until the arc front reaches the back surface.

---

[2] The value shown in the report with a superscript plus ($^+$) refers to the cylinder at positive potential with respect to the copper electrode.

[3] In the reports from VNIIEF, tables and figures are designated by numbers of the form #.#, e.g., Table 4.2. In this SAND report, tables and figures are designated by an integer, e.g., Figure 2.

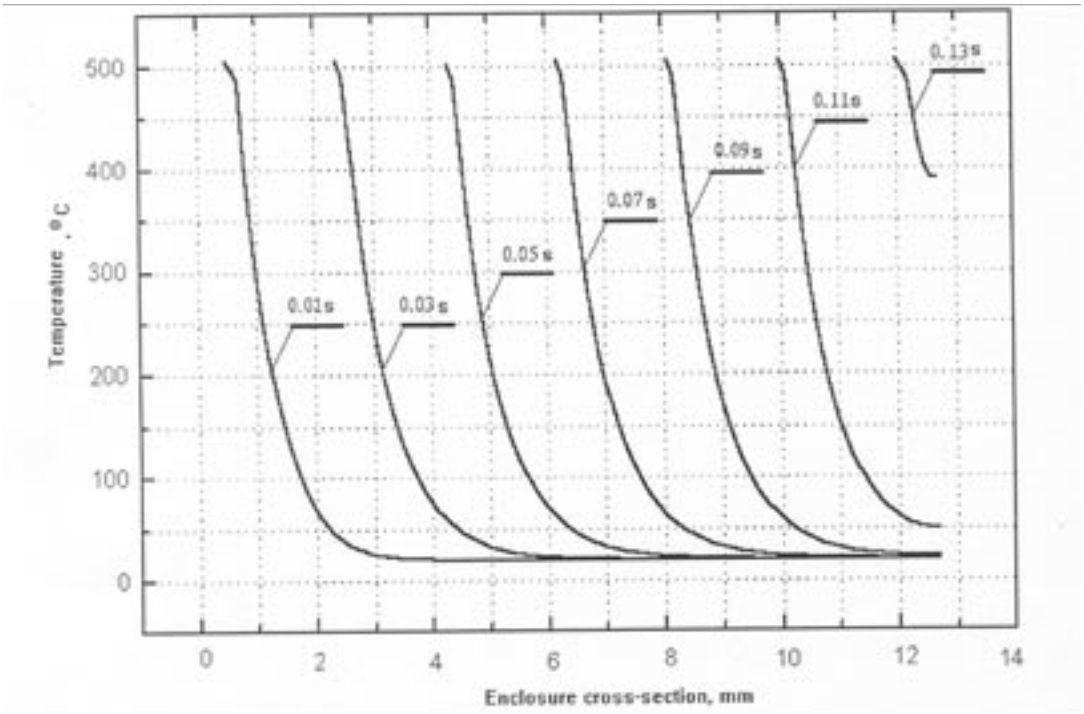

Figure 5. Predicted temperature profiles.

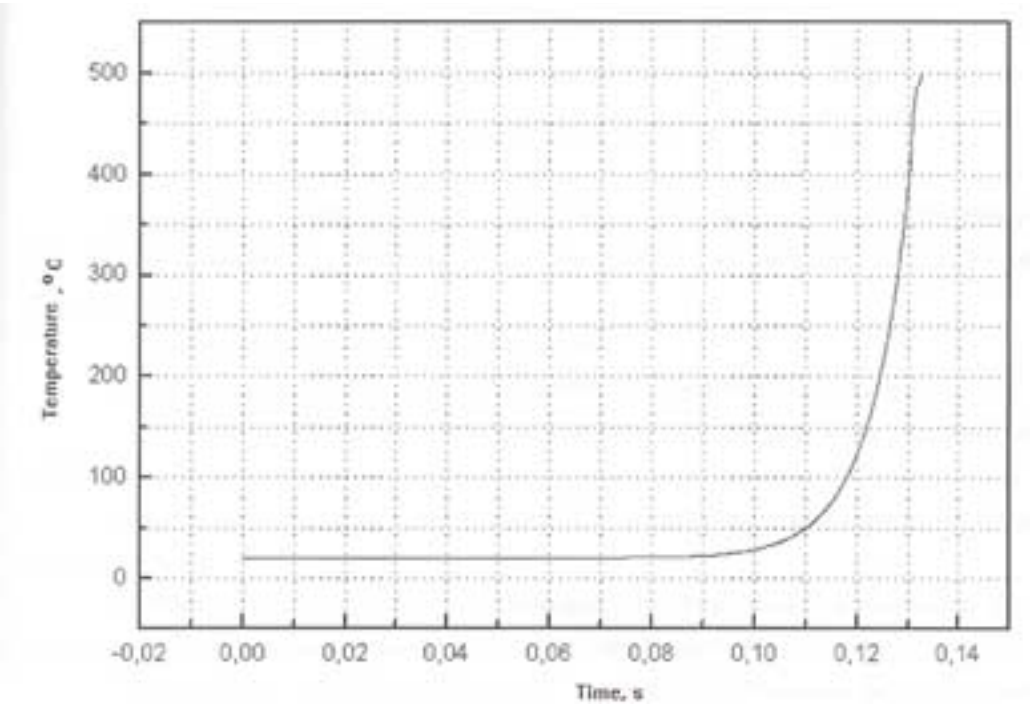

Figure 6. Time versus temperature at the back surface of the plate.

Section 5 of the report is difficult to understand. It addresses the effect of electrode-to-arc attachment point spacing on burn-through and the effect of current amplitude on time to burn-through. Skripnik and Prudkoi estimate that during most of a high-current burn-through event, the electrode-to-surface spacing will be greater than the spacing that would produce the fastest burn-through. They refer to Russian references to support their conclusions. The author was not able to confirm their conclusions. In this section, they also assert that the time to burn-through will be independent of current. They base their assertion on information in Russian language publications. The author was not able to confirm their assertion.

Final Report (Appendix C)

The final report supplied by Skripnik and Prudkoi contains information on the experiments that were conducted, results from the experiments, a discussion of heat transfer, and a comparison of results from the experiments with expectations derived from the analyses.

The arrangement of a copper electrode, a metal cylinder, and the power supply buses is shown in Figure 7, which is a duplicate of part of Figure 1.1 in the Final Report. Photographs of the arrangement are given in Figures 1.2 and 1.3 of the Final Report. The arrangement provided stable arc attachment points. The set up was designed so that a metal cylinder could be used for more than one test. Multiple use is seen in Figure 1.3 of the Final Report.

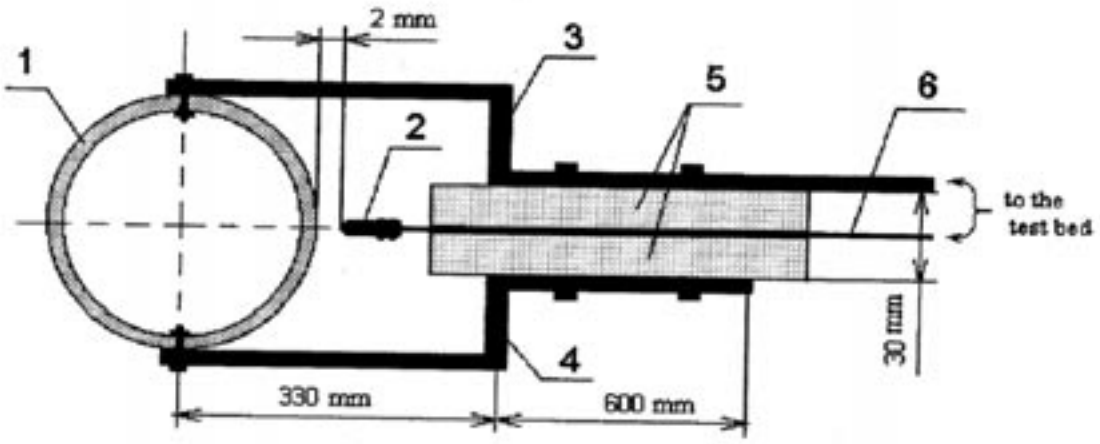

Figure 7. The test fixture, the test object, and electrical connections are shown. Designations: (1) test cylinder, (2) initial arc-to-cylinder spacing, (3&4) return circuit conductors, (5) insulator, (6) electrode conductor.

A photograph of the impulse generator at the All Russian Electrotechnical Institute is shown in Figure 1.4 of the report. The impulse generator consists of a motor, shown in the lower left part of the photograph, and a generator. The motor, although quite large, takes a few minutes to get the generator up to speed. When the generator is at speed, a large amount of energy is stored as kinetic energy of rotation in the armature. This stored energy is used to generate very large currents for fractions of a second. Some energy is also stored in the armature of the motor, but most is stored in the generator. Information on the capability of the generator is contained in Section 2 of the Subtask 2A Report. Both the motor and the generator are quite large. The author does not have dimensions of the equipment, but remembers that the motor-to-generator drive shaft was about head height — about 180 cm above floor level. The generator supplies current at 50 Hz. This frequency is common to power generation in all of Europe. The difference between 50 Hz and 60 Hz, which is used throughout the United States, is not important for the experiments. A circuit schematic for the current supply and monitoring is shown in Figure 1.5. Instrumentation is discussed in Sections 1.3 through 1.5 of the report. The arrangement of the experiment in a test bay is shown in Figure 1.10.

Six high-current burn-through experiments were conducted on aluminum cylinders, and six experiments were conducted on steel cylinders. Details for each experiment, along with results, are shown in Table 2. This table is a slightly augmented version of Table 2.1 in the Final Report. The values of current and voltage in this table are peak values. For each experiment, the Final Report contains time-amplitude records of current and voltage, records of back surface temperatures, and photographs of the damaged region. The scale markers in the Final Report for the time-current traces (for examples, see Figure 2.4) are easy to interpret because the symbols used to indicate amperes, A, and seconds, s or S, are the same as are used in English. However, on the time-voltage traces, (for example see Figure 2.5), a symbol that looks like the letter B written in Italics is used to indicate volts.

The peak current was 18.5 kA in experiment 1, it was 11.3 kA in experiment 2, it was 19.4 kA in experiments 4, 5, and 6, and it was 36.9 kA in the rest of the experiments. The intent was to test at two level of peak current. The lower than intended level of 11.3 kA may have been the result of an incorrect setting of the controls on the impulse generator. The peak current values of 18.5 kA and 19.4 kA are essentially the same; the difference arose from a variation in the operation of the generator.

Table 2. Data from experiments

Shot No.	14	Current Peak kA	Arc Voltage (V)	Time (ms)	Damage	Time to Burn-Through (ms)	Peak T (˚C) Inner Surface	Post Arc Photo (Final Report)
1	Steel	18.5	81-96	170	Crater: 40 mm diameter, 10.5 mm deep	N.A. **	160	Fig. 2.7
2	Steel	11.3	N.M.*	200	Crater: 34mm diameter, 9 mm deep	N.A.	196	Fig. 2.10
3	Steel	36.9	N.M.	200	Through hole: 57 mm top, 15 mm bottom	130 ± 10		Fig. 2.3
4	Alum.	19.4	N.M.	200	Through hole: 56 mm top, 38 mm bottom	52 ± 1		Fig. 2.14
5	Alum.	19.4	70-90	150	Through hole: 55 mm top, 31 mm bottom	79 ± 1		Fig. 2.2 Fig. 2.18
6	Alum.	19.4	55-85	100	Through hole: 38 mm top, 13 mm bottom	89 ± 1		Fig. 2.22
7	Alum.	36.9	85-95	50	Crater: 55.5 mm diameter, 12 mm deep	N.A.	145	Fig. 2.27
8	Alum.	36.9	85-100	70	Through hole: 55 mm top, 25 mm bottom	48 ± 1		Fig. 2.30
9	Alum.	36.9	85-85	60	Crater: 48 diameter, 12.5 mm deep	N.A.	195	Fig. 2.35
10	Steel	36.9	115-165	150	Through hole: 54 mm top, 8 mm bottom	126 ± 1		Fig. 2.38
11	Steel	36.9	100-135	130	Crater: 51 mm diameter, 12.5 mm deep	N.A.	200	Fig. 2.43
12	Steel	36.9	90-145	170	Through hole: 58 mm top, 10 mm bottom	125 ± 1		Fig. 2.46

* N.M. means the value was not measured for the shot.

** N.A. means that the column is not applicable for the shot.

Burn-through of 13-mm-thick aluminum[4] was observed for peak currents of 19.4 kA that lasted 100 milliseconds and for peak currents of 36.9 kA that lasted as long as 70 milliseconds. It was not observed for currents of 36.4 kA that lasted for 50 milliseconds or 60 milliseconds. However, these durations produced craters that almost penetrated the material. The outer diameter of the crater or penetration was in the range between 48 mm and 56 mm for all experiments except 6. It is not known why this experiment produced a crater with a diameter of only about 38 mm. The peak arc voltages measured in the experiments were in the range from 55 V to 100 V.

Skripnik and Prudkoi provide temperature-time data for the experiments in which burn-through did not occur. Data were not available for the experiments in which burn-through occurred because electrical noise from the arc was much larger than thermocouple signals. Temperature-time data were obtained in the two experiments with aluminum cylinders. The data for experiment 7 are given in Figure 2.26 of the VNIEEF report and the data for experiment 9 are given in Figure 2.34. The data in these figures are reproduced below in Figures 8 and 9, respectively. It is seen in Figures 8 and 9 that the temperature directly behind the arc attachment point reached, but did not exceed, 200˚C. It is also seen that the temperatures measured 25 mm out from the attachment point did not exceed 80˚C.

[4] Information on the composition of the aluminum is given on page 11 of the VNIIEF report.

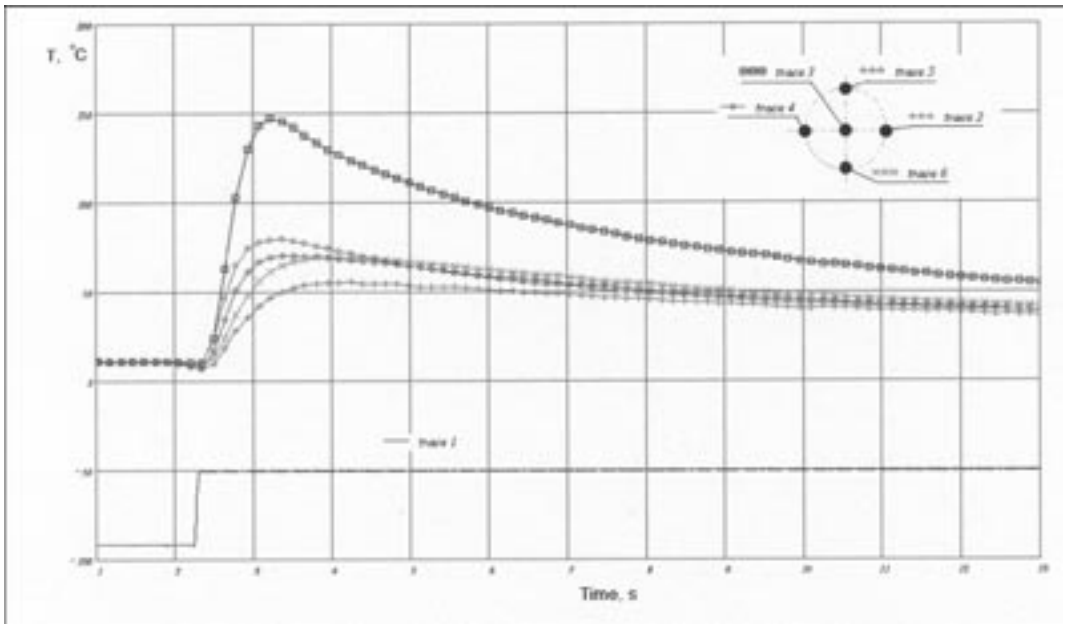

Figure 8. Back surface temperature-time data for aluminum cylinder, Shot 7. Conditions: 36.9-kA peak current, 50-milliseconds duration. Refer to Figure 2.26 in Appendix C for explanation of the thermal couple locations and of the traces.

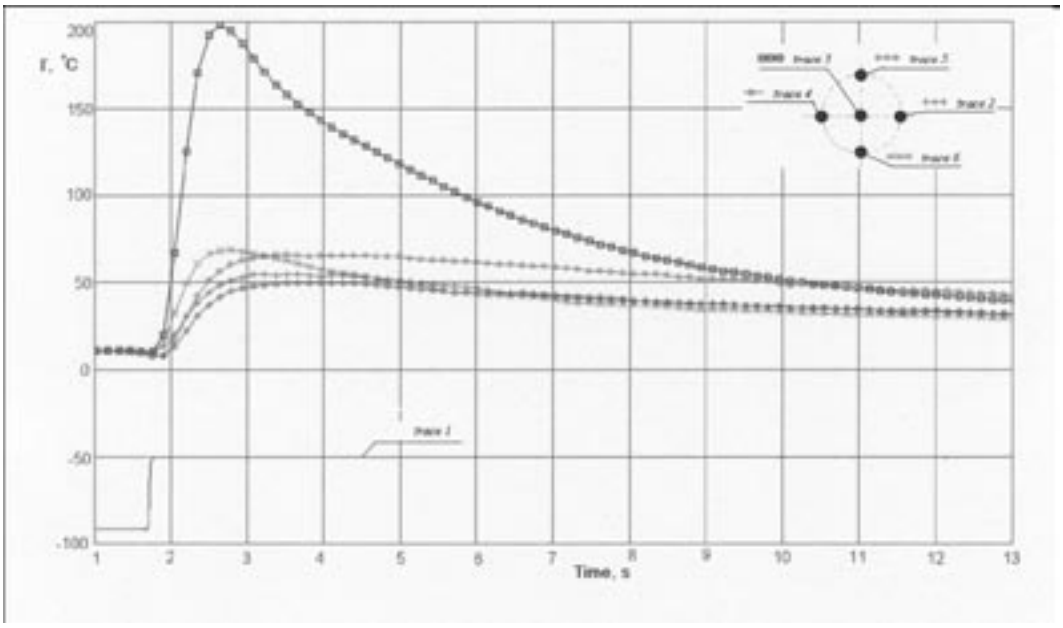

Figure 9. Back surface temperature-time data for aluminum cylinder, Shot 9. Conditions: 36.9-kA peak current, 60-milliseconds duration. See Figure 2.34 in Appendix C for explanation of the thermal couple locations and the traces.

Burn-through of 13-mm-thick steel[5] was observed for currents with peak amplitude of 36.9 kA and durations of 150 to 200 milliseconds. Burn-through was not observed for the following conditions: peak amplitude of 11.3 kA and duration of 200 milliseconds, peak amplitude of 18.5 kA and duration of 170 milliseconds, and peak amplitude of 36.9 kA and duration of 130 milliseconds. The holes had inner diameters between 8 mm and 15 mm and outer diameters between 54 mm and 57 mm. The current with peak amplitude of 36.9 kA and duration of 130 milliseconds produced a crater with a depth of 12.5 mm; that is, this combination of peak current and duration almost produced burn-through.

Temperature-time data were obtained for steel cylinder experiments 1, 2, and 11. The data are shown in Figures 2.6, 2.9, and 2.42 in the VNIIEF report. Peak back surfaces temperatures of about 180˚C were recorded in experiments 1 and 2 and peak temperature of about 200˚C was recorded in experiment 11. The highest temperature was recorded in the experiment that produced the deepest crater. Whereas, the highest back surface temperature was recorded on the experiment that produced the deepest crater, nearly the same peak temperatures were recorded in the other two experiments. There are not enough data to determine how the variables of arc current, arc duration, and crater depth individually affect back surface temperature. In all three of the experiments for which there were data, the off axis temperatures were lower than the on axis temperature. Also, the off axis temperatures showed slower rates of rise.

Section 3 of the Final Report shows analyses of heating by high-current arcs. The model presented in this section is the same as the one presented in the Subtask 2B report. The model includes heat of fusion, but does not include heat of vaporization. Heat of vaporization is not included in the model because it is assumed that molten metal is removed by magnetic forces rather than by evaporation. The finite difference method shown as Equation 3.9 in the report was not verified. The values for physical properties of aluminum alloys given in Section 3.2 of the report are consistent with values given elsewhere (Carslaw and Jaeger 1959).

Skripnik and Prudkoi used the model to calculate times to burn-through for two assumptions about heat of fusion and two assumptions about heat flux from the arc. They assumed that the heat of fusion was either nil or 3.9E4 J/kg, and they assumed that heat flux was either uniform across the arc or followed a Gaussian distribution. A burn-through time of 116 milliseconds was calculated for uniform heating and heat of fusion set to zero. The value of 154 milliseconds was calculated for the same heating, but with heat of fusion set equal to 3.9E4 J/kg. The values for a Gaussian distribution of heat were 58 milliseconds and 77 milliseconds respectively. These values are compared with data from experiments below. The model predicts very steep temperature profiles behind the melt zone. The profiles are consistent with those presented in the Subtask 2B report.

---

[5] Information on the composition of the steel is given on page 11 of the VNIIEF report.

Skripnik and Prudkoi also applied the model to the estimation of time to burn-through of steel shells. They obtained 420 milliseconds for uniform distribution of heat, and 211 milliseconds for a Gaussian distribution of heat. To obtain these results, they assumed that the heat of fusion was zero. Steep temperature profiles behind the melt zone were also predicted for steel shells. Calculated profiles are shown in Figures 3.9 and 3.10 of their report.

In Section 4 of their report, Skripnik and Prudkoi observe that burn-through of both aluminum and steel cylinders was achieved. They further observe that the time to burn-through did not have a strong dependence on the current. The data for both aluminum cylinders and steel cylinders show that burn-through time decreased by less than a factor of two when current was doubled. In fact, the shortest time to burn-through of 52 milliseconds for 19.4 kA was nearly the same as the time of 48 milliseconds observed for burn-through with 36.9 kA. They observe that the arc voltage was in the 55 to 100 volt range for arcs to aluminum and in the 81 to 165 volt range for arcs to steel. They also observe that the arc voltage increased as the arc length increased.

They conclude that there is satisfactory agreement between estimated and measured times to burn-through. This conclusion is explored further in the next section.

5. Discussion

Burn-throughs of 13-mm-thick sections of aluminum and of steel were observed for arc currents and arc durations that could occur in an accident. The observations imply that burn-through of thinner sections could occur for the same currents and durations or, possibly, for smaller currents or shorter durations. The data show that time to burn-through decreased as current increased; this relation was expected. However, the data do not support a simple reciprocal relation between current and time. That is, the data do not show that time to burn-through decreased by a factor of 1.9 when the current was increased by a factor of 1.9.[6] In fact, the time decreased by less than a factor of 1.9 when the current was increased by this factor. Data show that the outer diameters of burn-through holes were larger for larger currents. This observation is consistent with the result that arc diameter increases with increasing current that follows from the assumption that arc current density is approximately constant for a specified electrode pair.

The experiments did not explore the boundaries of arc stability. The issue of arc stability is discussed in the Subtask 2A Report. Concerns about stability led to the design of the fixtures used for the tests. Stable arcs were obtained with the fixtures. It is not known what variations in arc length, current return path, and other details would have led to loss of stability. The impulse generator was operated with an open circuit voltage of at least 2 kV so that a stable arc would be initiated. The minimum voltage for initiation of stable arcs was not determined. Skripnik and Prudkoi were interested in exploring the limits of stability, but there was no funding for such work.

During an accident, the voltage available to initiate arcing might be much larger than the nominal voltage because of inductive effects. An arc could be initiated when a conductor in contact with a metal shell pulls away from the shell. If current were flowing at the time of pull away, the voltage induced in circuit inductance could be much larger than the nominal voltage. Therefore, the use of 2 kV to initiate arcing in the experiments does not mean that stable arcing could not occur at lower voltages.

The thermal analyses done by Skripnik and Prudkoi, the photographs of craters and nearby surfaces, and the thermocouple records lead to following description of burn-through. Heat from the arc melts a layer of metal. There is pressure of the molten metal from magnetic forces. The pressure, which is greatest near the electrode, is in the direction to push the molten metal into the still solid metal. Because the pressure is greatest near the center, molten metal moves out from the center and flows away along the walls of a developing crater. The magnetic pressures are very large because the currents are very large. Therefore, molten metal and heat are rapidly removed from a developing crater. The arc supplies heat to melt a film of metal, and the

---

[6] The value of 1.9 is equal to the ratio of 36.9 kA to 19.4 kA.

molten metal is removed immediately. Therefore, little heat is applied to the metal behind the melt front. This expectation is consistent with all of the thermocouple records. The records for experiment 9 (Figure 2.34 in the Final Report) show that the temperature directly behind the bottom of the crater did not reach 200˚C even though the bottom of the crater came within one-half millimeter of the back surface.

Some of the molten metal ended up just beyond the edges of the crater, and some was sprayed quite far away. Metal close to the edge of a crater is seen in Figure 2.3 of the Final Report, and the spraying of metal can be deduced from comparison of Figures 1.2 and 2.3.

The times for burn-through estimated from the models, particularly for burn-through of steel, are longer than the measured times. This result is surprising because one might expect that processes not included in the simple models would reduce the efficiency of heat transfer and metal removal. To improve the agreement between calculation and experiment, Skripnik and Prudkoi assumed for some calculations that the heat of fusion was zero. This assumption is not consistent with the presence of re-solidified material outside of craters. Such material is seen in post-exposure photographs contained in the Final Report. A more credible explanation for the discrepancy between calculated and observed burn-through times is that their models underestimated arc-to-melt-zone heat transfer.

6. Conclusions

Electric arc burn-through of 13-mm-thick aluminum and steel was demonstrated. Experiments were conducted with 50 Hz ac arc currents with peak amplitudes between 11.3 kA and 36.9 kA and with durations between 50 milliseconds and 200 milliseconds. Burn-through of aluminum was observed after 52-millisecond exposure to a 19.4 kA current. Burn-through of steel was observed after 125-millisecond exposure to a 36.9 kA current. These current amplitudes and durations might occur in an accident in which an aluminum or steel container contacted a distribution-voltage-to-480-V step down transformer. Burn-through of less than 13-mm-thick aluminum or steel is certainly possible in such an accident.

Two phenomena make primary contributions to burn-through. Heat from the electric arc melts metal. Magnetic forces rapidly move molten metal away from the melt zone and out of the growing crater. A large amount of the heat deposited into the metal is carried away by the molten metal. Therefore, the metal near the crater does not get very hot until burn-through occurs.

The analyses, design and operation of fixtures and equipment, and reporting by Skripnik and Prudkoi were all excellent. Their willingness and ability to turn a request for quote into a technical program and then execute the program were essential to completion of the work described in this report.

References

Carslaw, H.S., and Jaeger, J.C., Conduction of Heat In Solids, (Oxford University Press, 1959).
Dobranich, D., Private communication, 1996.

Knorovsky, G., Private communication, June, 2001.

Loescher, D.H., and Duran, P.A., Electric Power Challenges to Nuclear Explosive Safety(U), SAND97-1317(U), Sandia National Laboratories, June 1997.

Appendix A

VNIIEF Report on Subtask 2A

RUSSIAN FEDERAL NUCLEAR CENTER

607190 Russia,
Nizhny Novgorod region
Sarov, Mira 37,
RFNC – VNIIEF

Document number 0613OTN3 – 98
Data 19 February, 1998

This report is accomplished within the framework of contract AV – 5840

Contractor
Institute of Experimental Physics
(VNIIEF)

ELECTRIC ARC EFFECT ON EXPLOSIVE SAFETY

(Task N2A – Interim Report)

The main regularities of the influence produced by the short – circuit currents on metallic enclosures are considered and an arrangement of experimental studies of the effect produced by the electric arc of the short – circuit currents on metallic enclosures is worked out in detail. Specification of a technique for modelling the short – circuit currents, measuring the internal enclosure surface temperature and arranging the arc effect on the object under study is justified.

Investigators:

B. F. Skripnik
N. A. Prudkoi

Intrpreter:

I. B. Kalatinskaya

CONTENTS

CHAPTER 1.

Main Mechanisms of the Short–Circuit Current Effect on Metallic Enclosures

Under fault condition (short–circuit) the pulse currents being much higher than rated occur in the power networks. The maximum magnitude of short–circuit currents may achieve many tens of kiloamperes with duration being tenth fractions of a second. The two physical phenomena form the basis of undesirable effects of the pulse currents flow: energy release in the form of heat in the conductors when the current is flowing through them and creation of magnetic field in the space around conductor and in the conductor itself as well. The pulse current flowing in the medium with a specified electrical causes heating of the medium which is often close to adiabatic heating. Under heating, mechanical properties of the medium and its thermophysical parameters change and phase transformations occur. A so–called "specific effect" is considered to be a generalized parameter describing the energy release in the pulse current flow:

$$A = \int_0^t j^2 dt \qquad (1.1)$$

where j – current density.

The temperature of conductor after the current has flown is defined by the value of "specific effect".

In many cases the pulse current flow is accompanied by the arc burning between metallic electrodes. In the contact points between the arc and the metal erosion is observed, which is manifested by evaporation, melting and spraying of metal /1/. Erosion processes are defined by the rate of the energy introduction in the electrode. In the majority of cases erosion is caused by a surface heat source coming from the near–electrode arc zone. Since the near–electrode voltage drop is slightly dependent on current, the energy coming into the electrode is proportional to the charge Q, carried by the current I:

$$Q = \int_0^t I dt, \qquad (1.2)$$

and erosion is usually associated with Q.

For a model of the arc effect on metallic enclosure, set in the contract (Fig. 1.1), the effective value of the short–circuit current is 30 kA at duration $\approx$ 0,3 s.

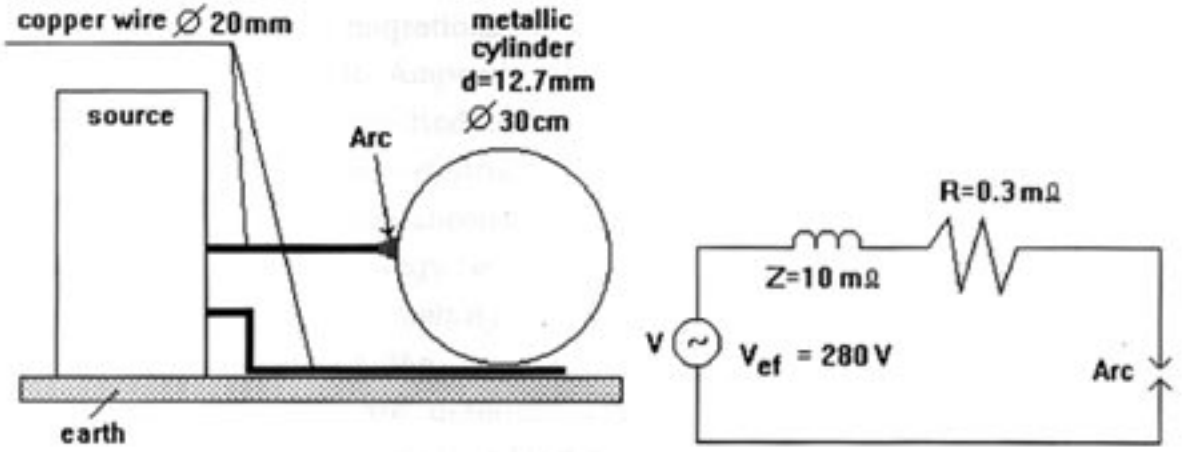

Fig 1.1

In a set model the arc burning, besides burn−through of the enclosure, is accompanied also by erosion of the copper electrode. As a result of erosion, the length of the copper electrode decreases. The copper electrode shortening may be estimated by extrapolating the results of experimental studies /2−3/ :

$$\Delta\ell_e \approx \frac{4m_{sp}I\cdot T}{\pi d^2\rho} = \frac{4\cdot 7\cdot 30\cdot 10^3\cdot 0.3}{\pi\cdot 20^2\cdot 8.9} = 23\text{mm} \quad , \qquad (1.3)$$

where m_{sp} =7mg/C − specific erosion of the copper electrode; d =20 mm − diameter of the copper electrode; ρ=8.9 mg/mm^3 − copper density; I=30·10^3 A− effective value of current; T=0.3 s −duration of current pulse.

In the experiments $\Delta\ell_e$ may serve as a step measure of variation of clearance between the electrode and the object.

The open arc column located between the electrodes is affected by: electrodynamic forces of the interaction between the arc current and surrounding magnetic field; force of the air resistance to a gas arc column motion; force of the inherent hear flux effect.

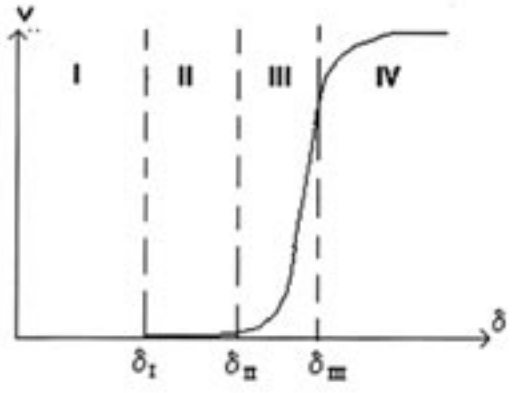

Fig 1.2 Influence of clearance on the rate of the reference arc points motion under magnetic field effect

Under the influence of these forces the reference points of the arc may move, and the arc itself may increase in the length.

For relatively short arcs, typical of our case, a decisive influence on the arc motion is produced by two factors: clearance and magnetic field. It follows from studies /4, 5/ that the influence of clearance on the arc motion is either determining (zones **I**−**III** Fig. 1.2) or is completely absent.

Zone I is characterized by the absence of directed shift of the arc reference

points, only spontaneous migrations of the arc channel near the point of its origin are observed. According to Ampere's law, the absence of reference points shift is explained by insufficient electrodynamic force affecting the arc. These conditions are characterized by intensive destruction of the enclosure.

The presence of spontaneous migrations results from the need to ensure a discharge at minimum energy consumption /6, 7/. Since, actually, the arc reference points are fixed, a melting zone forms on the enclosure, which is defined by the integral effect of the heat sources moving within the limited area. Dimensions of this area are determined both by the heat source power and duration of its application as well as by the enclosure material.

Zone **II** is characterized by the presence of directed shift of the arc reference points but in this case the shift rates are not significant. This shift is accompanied by a strong fusion of the enclosure surface.

It may be supposed that the rates of the reference points shifts are defined by the rates of advancement of the melting zone of material in front of the arc reference point which depend both on the material thermophysical properties and the heat source power. Since in this case a distance between the electrode and the enclosure is short and "rigidity" of the arc channel is high, the interaction between the arc reference points and the enclosure material produces a decisive effect on the arc shift character. To specify the boundaries of Zone **II** origin, the following criterion may be used /8/.

$$HI\delta^2 > k, \tag{1.4}$$

where **H** – magnetic intensity; **I** – arc current; δ – clearance; k – constant dependent on material and state. The estimated value is $k \sim 10\ A^2 \cdot m$.

Zone **III** is characterized by a rapid increase of the rate. It follows from the numerous studies that this zone is described by the marked instability of the arc behavior.

Zone **IV** corresponds to the arc movement rate defined by the experiment conditions. In this case, despite continuous increase of a distance between the electrodes, the growth of the rate does not occur /8/ gives a criterion which allows to specify a boundary of this zone origin:

$$H\delta^3 > k_1, \tag{1.5}$$

where k_1 – constant. The estimated value is $k_1 \sim 10^{-4}\ A \cdot m^2$.

As applied to a set model of the effect produced by the arc on the enclosure and considering that the external magnetic field affecting the arc may be estimated by the formula

$$H = \frac{I}{2\pi D} \tag{1.6}$$

conditions (1.4) and (1.5) may be written as follows:

$$\delta > \frac{\sqrt{2\pi Dk}}{I} = \frac{\sqrt{2\pi \cdot 0.3 \cdot 10}}{30 \cdot 10^3} \approx 0.15 \cdot 10^{-3}\,\text{m} = 0.15\,\text{mm} \qquad (1.7)$$

$$\delta > \sqrt[3]{\frac{2\pi Dk_1}{I}} = \sqrt[3]{\frac{2\pi \cdot 0.3 \cdot 10^{-4}}{30 \cdot 10^3}} \approx 2 \cdot 10^{-3}\,\text{m} = 2\,\text{mm} \qquad (1.8)$$

These estimations are, of course, rather approximate but they allow to get some idea of the character of processes occurring during the arc burning between the electrode and the enclosure.

The relationships (1.7, 1.8) show that at any initial clearance the major part of total time of the arc burning is favourable to the arc movement.

In these conditions it may be thought that, when moving in the magnetic field, the arc column behaves somewhat like a rigid body, since due to a high temperature in the column the penetration of gas through it is difficult. To approximately estimate the arc column movement, the following empirical dependencies /9/ may be used:

$$v = 40\sqrt[3]{IH^2 / (1 + 0{,}4H^{0{,}3})^2}, \qquad (1.9)$$

$$v = 37\sqrt[3]{I} \qquad (1.10)$$

where I – arc current, A; H – magnetic intensity, A/cm, v – velocity, sm/s; and where the latter relationship is the lower boundary estimate for the rate of free-burning arcs movement.

The estimates based on (1.9, 1.10) show that the average velocity of the arc movement is higher than tens of meters per second.

As applied to the arc effect model (Fig. 1.1), it means that if special measures to stabilize the arc reference point on the enclosure surface are not taken, the reference point will shift within ≈ 10 ms to the upper section of a cylinder after which the shift will take place with fixed reference point. The expected character of the arc movement is given in Fig.1.3.

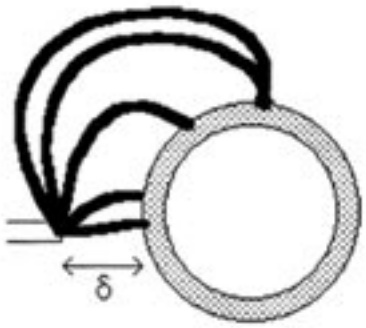

Fig. 1.3

In this case a scenario of the arc development depends on the relationship between the arc resistance and the source voltage.

Experimental studies have shown that the arc voltage gradient does not practically depend on current and, according to /10–14/, the arc active resistance, Ohm, is advised to be defined using the following formulae which differ in coefficient values and, sometimes, in their structure:

$$r_{eff} = 1050\frac{\ell_a}{I_{eff}}; \tag{1.11}$$

$$r_{eff} = 370\frac{l_a}{I_{eff}^{0,87}}; \tag{1.12}$$

$$r_{eff} = 27810\frac{\ell_a}{I_{eff}^{1,4}}; \tag{1.13}$$

$$r_{eff} = \frac{0,05}{I_{eff}}(U + 17v_w t); \tag{1.14}$$

$$r_{eff} = 2500\frac{\ell_a}{I_{eff}}; \tag{1.15}$$

$$r_{eff} = 28700\frac{l_a}{I_{eff}^{1,4}}; \tag{1.16}$$

where I_{eff} – effective arc current value in amperes in the formulae (1.11), (1.12), (1.13), (1.15), (1.16) and in kiloamperes in (1.14); l_a – arc length, m; U – voltage, kV; t – time, s; v_w – wind velocity, km/h.

In Russia, according to studies /11/, the arc voltage gradient, as being slightly dependent on current at its high values, is assumed to be constant and equal to 1100 – 1500 V/m.

The ac open arc extinction occurrs when the circuit voltage is not sufficient to maintain the arc burning. In this case the arc extends achieving a critical length, the circuit current gradually decreases and the circuit completely opens. The moment of the current opening coincides with the moment of its passage through zero.

At longitudinal gradient of the arc $E_a = 1500$ V/m and effective source voltage U = 280 V, the conditions favourable for the arc extinction are created at:

$$l_{cr} = \frac{U}{E_{eff}} = \frac{280}{1500} \approx 0.2 \text{ m} = 20 \text{ cm} \tag{1.17}$$

This means that the arc extinction will occur approximately within:

$$t = \frac{l_{cr}}{v} = \frac{0.2}{10} = 0.02 \text{ s} \tag{1.18}$$

i.e. after two half – periods of current.

Time of the arc burning set in the model (0.3s) may be achieved only at voltages higher than 4 kV.

If the arc reference point on the enclosure is stable, the arc will move with fixed reference point (Fig. 1.4). Under the influence of electrodynamic forces the arc column extends and the voltage in the gap increases. At a considerable value of length the gap break – down occurrs on the short path. A relationship between a complete arc length and a clearance may achieve $\frac{\ell}{\delta} \approx 5 \div 20$ /15/.

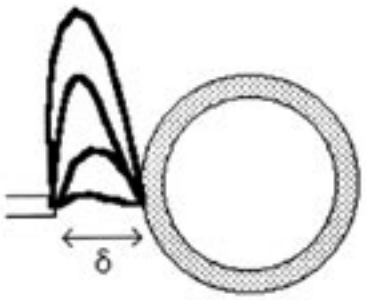

Fig. 1.4

Then, a critical clearance at which maintaining the arc burning is possible equals $\delta \approx 1 \div 4$ cm. This value is comparable with the copper electrode erosion, therefore it is likely that in this situation the time of the arc burning will also be less than set in the model.

The arc is also exposed to the influence of the upward heat flows occurring near the arc column. The rate of the upward heat flows, according to /16/, is 1.4 – 1.5 m/s and the effect produced by these flows on the arc is not significant as compared to the magnetic field effect.

The analysis made shows that:

– if the arc reference point is not stabilized on the enclosure, the time of the arc burning at a set in the model effect of the source voltage does not exceed ~ 20 ms at practically any clearances between the electrode and enclosure;

– if the arc reference point is stabilized on the enclosure, a rather long arc burning is possible at clearances $\delta \leq 1 \div 4$ cm, however, there is a good probability that this time interval will be several times less than set in the model;

– set in the model time of effect may be surely achieved only when using high voltages (several kilovolts) or with the arc column localization.

CHAPTER 2

Short−circuit current modelling

Pulse currents at comparatively low power in the load may be obtained directly from a circuit in conditions close to short−circuits. Thus, for connecting the load and switching off the current the switching equipment is required. The highest power in the load develops at the load resistance close to the internal source resistance. To comply resistances of the source and the load, step−down transformers are usually used. Such method of obtaining pulse currents is employed in various technological operations of manufacturing constant magnets, particularly for magnetic treatment, magnetization. However, in our case it is not applicable since, first, it is dangerous for a circuit and, second, the current durations required exceed the settings of short−circuit protection. High pulse current generators usually serve as the energy storages.

The most widely used storages include capacity, inductive, mechanical (e.g. impact−excited generators), chemical storages (pulse accumulators) and various combinations of storages. Each of the enumerated storages may serve as a source of pulse currents with specified magnitude, shape and duration. Capacity storages in combination with inductive storages and impact−excited generators are used to obtain oscillatory current pulses and all the rest storages, including capacity and inductive ones, are used to obtain unipolar pulse. The idea of potentialities of this or that source is presented in Fig.2.1 which shows the limits of achieved currents at specified pulse durations for conventional versions of storages. With additional operations for example reducing discharge circuit inductance of an impact−excited generator, using matching transformers, etc., it is possible to considerably expand the areas shown in Fig.2.1. Impact−excited generators are widely used in testing the high−voltage switching equipment /17, 18, 19, 20, 21,

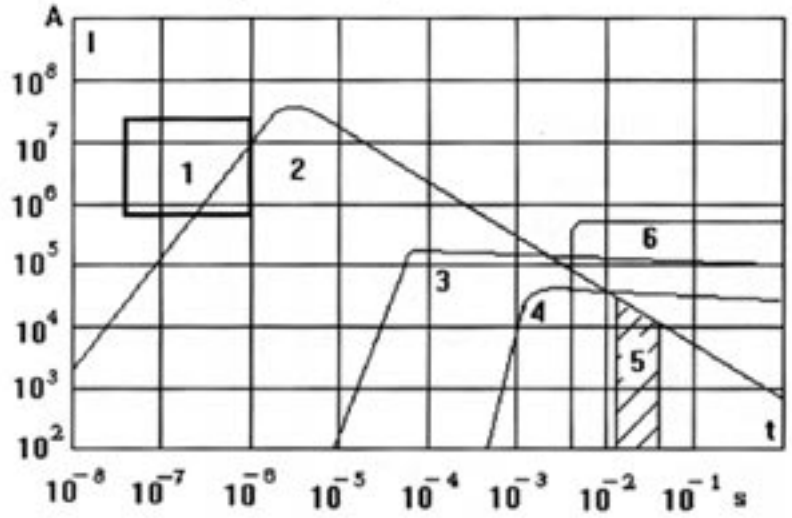

Fig 2.1 Maximum values and durations of pulse currents produced from different sources: 1−explosive generators; 2−capacity energy storages; 3−inductive energy storages; 4−pulse accumulators; 5−Gorev's contour; 6−impact−excited generators.

22, 23/. Switching capability testing of apparatus is carried out to control the performance of the switch during turning on and off the rated currents, overload and short−circuit currents up to the limiting values warranted by manufacturer.

Impact−excited generators are the upgraded three−phase turbogenerators having power up to 300 MV·A in which mechanical and electrical winding strength is improved, excitation system is modified and short−circuit power is considerably increased. In short−term conditions the power being one order of magnitude higher than rated is obtained from the impact−excited generators. With the power about 10^3 kW of the engine rotating the generator rotor with a flywheel having a total weight up to several hundreds of tons the generator develops the power up to 10^6 kV · A within tenth fractions of a second. Usually the impact−excited generators have the voltage 10−20 kV. To test the switches of various voltage classes, step−up transformers are used which allow to adjust voltage by means of various connections of transformer windings.

At the duration 10^{-1}−1 s the energy stored in the impact−excited generators achieves 10^9 J and maximum currents attain several hundreds of kiloamperes.

Fig. 2.2 gives a typical oscillogram of the abrupt short−circuit current and the voltage on the apparatus subjected to the switching capability test /24/.

At the moment of time t_1 a circuit with closed contracts of the apparatus under test is switched on the voltage source. The abrupt short−circuit current occurrs. The voltage falls practically to a zero. At the moment of time t_2 during the abrupt short−circuit current passage through a zero the apparatus contracts open. During one of the current passages through a zero the electric arc extinction occurrs (moment of time t_3).

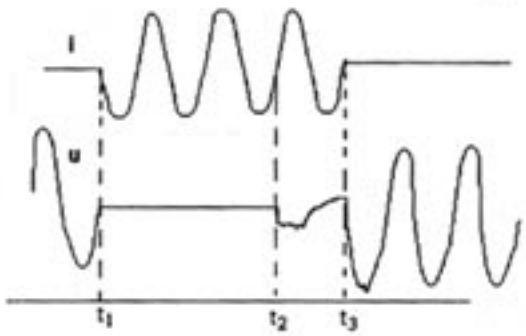

Fig 2.2 Oscillogram of abrupt short−circuit current and voltage at the switching apparatus contacts

The second mode of operation of the impact−excited generators includes testing the switchgears for the arc resistance. In this operation the explosive wires are used to initiate the arc. The wire explosion is followed by formation in the gap between the electrodes of a channel filled with neutral nonconducting vapor, liquid metal drops floating in it. The conductor explosion leads to a rapid increase of resistance in the gap between the electrodes and to discharge current fall. The overvoltage produced by the wire explosion results in a breakdown of gas clearance and formation of the arc. As the arc starts burning, the voltage falls to the minimum and remains practically constant up to the end of the current pulse. The fall of resistance in the process of the arc development is subordinate to the following empirical dependence /26/:

$$R_a = k\ell_a / \int_0^t i_a dt, \qquad (2.1)$$

where l_a – length of the gap between the electrodes; i_a – arc current; k – Tepler's constant being $3 \cdot 10^{-2}$ s·V/m for the air.

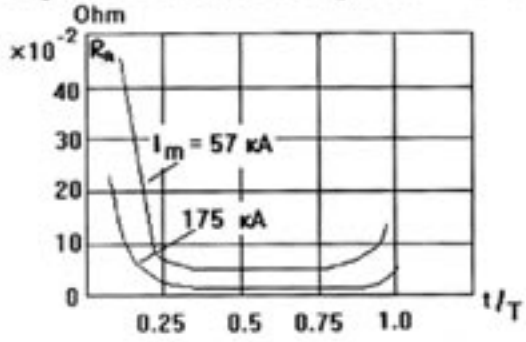

Fig. 2.3

Fig. 2.3 shows a variation of the arc channel resistance during a halfperiod of current /27/.

At the initial moments of time the arc has a high resistance and to prevent its extinction the source voltage should be sufficiently high. Experimental studies show that a reliable initiation of clearances with a length up to 10 cm may be achieved at the voltage ≈ 2 kV. /25/

To carry out experimental studies, we have chosen a test unit (Fig. 2.4) based on the impact – excited generator TI – 100 – 2. Besides the generator, the test unit also includes: set of transformers, reactors for controlling the current strength and switching equipment. The limiting characteristics of the test unit in modelling a single – phase short – circuit are given in Table 2.1.

Table 2.1 Characteristics of generator test unit TI–100–2

Voltage (effective value), kV	6	7.5	12	15	24	48	70
Current (effective value), kA	130	100	100	60	37	18	12
Power, MVA	780	750	1200	900	890	865	840

Maximum duration of the test unit current pulse is ≈ 0.3 s.

It follows from the characteristics of specified test unit that it ensures a required amplitude and duration of short – circuit current as well as the voltage sufficient to initiate the arc.

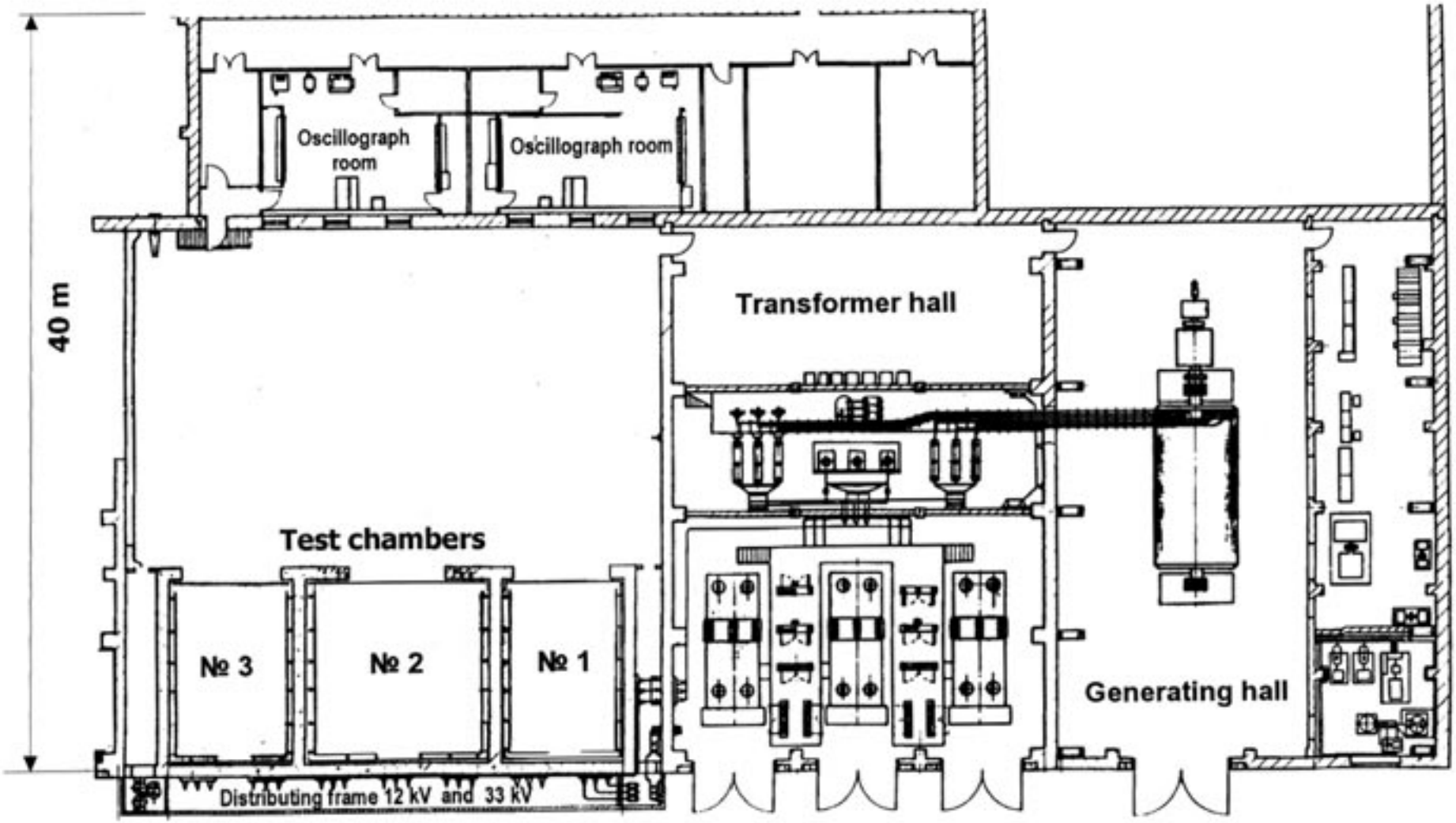

Fig. 2.4. The scheme of the arrangement of an equipment of the test unit

CHAPTER 3

Internal enclosure surface temperature measurement

3.1. Specification of scheme and method of temperature measurement.

To measure the surface temperature, thermocouples, plane resistance thermometeres (thin−film of wire−typed), thermosensitive pencils and paints, fuse links and pyrometers are more frequently used. Thermosensitive pencils and paints and fuse links are the single−action indicators and hence are not suitable for the set task.

The use of pyrometers is limited by sophisticated calibration, body surface state recording, scanning organization and external factor effect consideration.

The most simple way to measure the body surface temperature is using plane resistance thermometers or thermocouples. The temperature measured by resistor or thermocouple is actually a sensor temperature. Resistance thermometers designed to measure the surface temperatures resemble tensometers and are made of nickel and iron−nickel alloys using photochemical technique. Metal thickness is several micrometers and resistor thickness is of the order of 1 cm. Operating temperature range is −195° C ÷ 260° C for nickel and iron−nickel alloys and −260° C ÷ 1400° C for platinum. Sensors are applied to the surface the temperature of which is to be measured. High value of the ratio between a sensor surface area and its volume and small thermal resistance between a sensor and surface provide very small values of delay time (about 1 ms). It should be noted that a thermometer, in principle, like a tensometer, is sensitive to the deformation of a specimen which it is applied to. Irregular expansion of a sensor and specimen is another source of the error. This factor also causes the problems in mounting a sensor. Moreover, such sensors change the surface cooling conditions and impede fast filming of the surface.

In our opinion, the most acceptable way is to measure the object surface temperature using thermocouples. Since the measuring information comes from the junction which may be very small−sized, this ensures fast operation and allows to make point−by−point temperature measurements. Also, due to their small size, thermocouples are no barrier to the fact filming. Mentioned features define the advantage of using thermocouples, as compared to resistance thermometers.

To measure the object temperature we propose to use chromel−alumel thermocouples (chromel−alumel thermocouples have the limiting tempetature 1300°C and are the most heatproof among series−produced base metal thermocouples). Thermocouples are mounted by pressing in the depth being more than a thermocouple wire diameter. Measuring scheme is shown in Fig. 3.1. The signals from five thermocouples come to the input of a five−channel amplifier.

Every channel has a differential input for thermocouple connection. The signal from the amplifier outputs are supplied to the inputs a multichannel recorder H. In measuring temperature from 0° to 1000° C a thermocouple efficiency varies within 0÷45 mV. Since the range of recorder input signals is ±1 V, we assume the coefficient of amplification to be 20.

For time reference the sixth channel of recorder is used where a synchrosignal from the camera is supplied. The amplifiers and recorder are powered via the isolation transformer. A recorder is remote−controlled via decoupler based on the optoelectronic transistor. To reduce the interferences occurring at the arc discharge, the amplifier assembly and recorder are placed in the screened chamber.

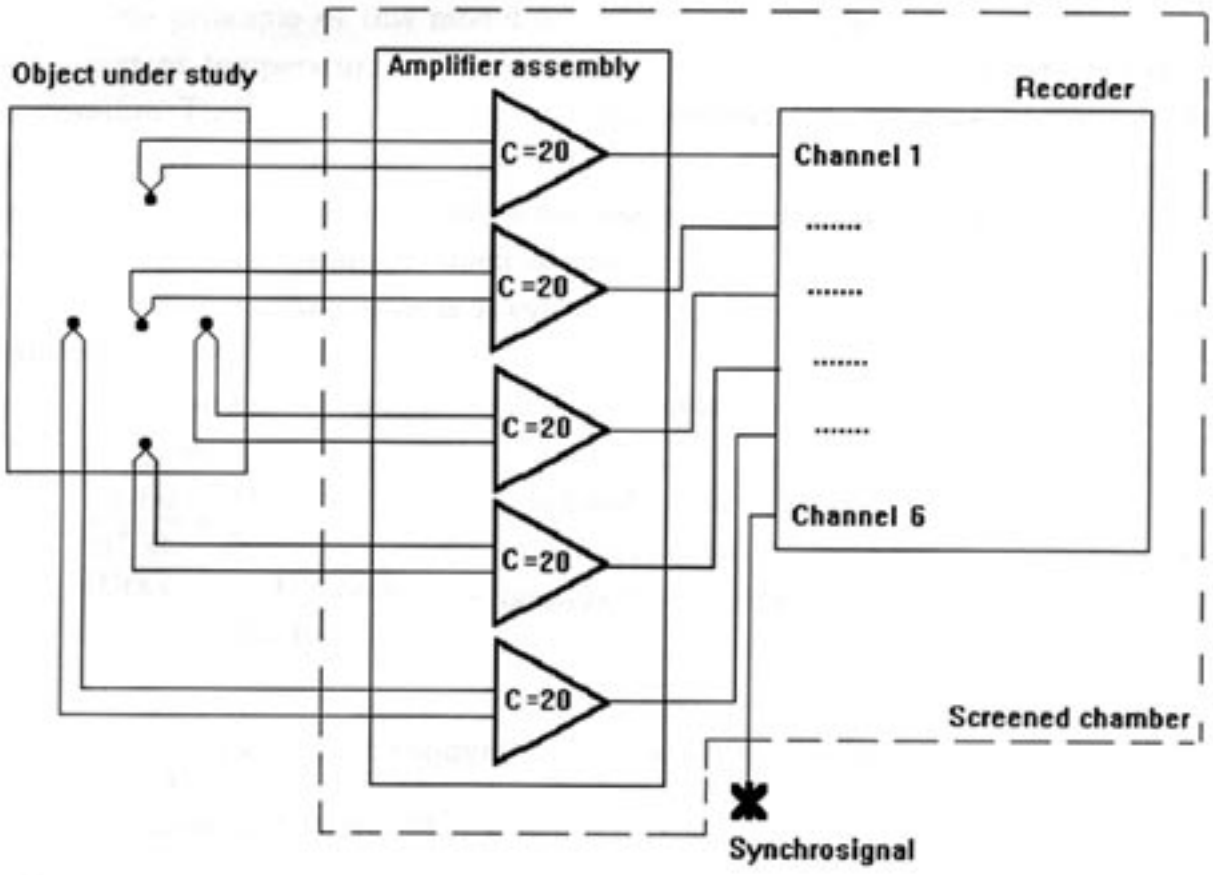

Fig 3.1

3.2. Estimation of thermocouple parameters

Time resolution of a thermocouple may be estimated using a model presented in Fig. 3.2.

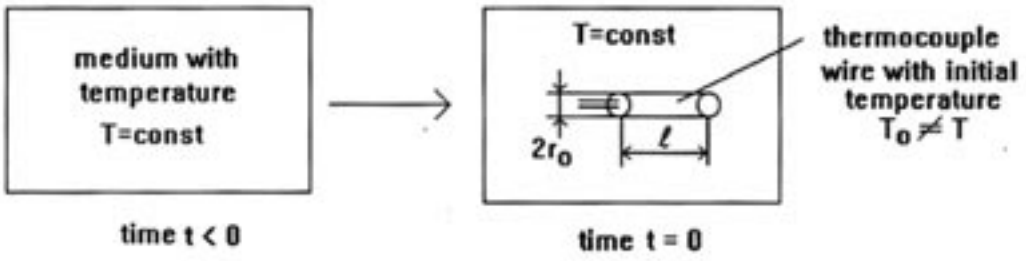

Fig. 3.2

The principle of this model is that if at the moment t=0 in the medium with constant temperature T a thermocouple is instantly placed, which has the temperature T_0 different from the medium temperature, the time of the junction temperature relaxation (from T_0 to T) will characterize the time resolution of thermocouple. The following approximations are assumed in the model:

а) T=const for any moment of time $t \geq 0$;

б) thermocouple wire is a cylinder with the length l being much longer than its radius r_0.

Distribution of temperature U in a cylinder section is described by the following system:

$$\begin{cases} \dfrac{1}{a^2}\dfrac{\partial U}{\partial t} = \dfrac{\partial^2 U}{\partial x^2} & - \text{heat conduction equation;} \\ U(x, t=0) = T_0 = \text{const} & - \text{initial condition;} \\ U(\pm\ell, t=0) = T = \text{const} & - \text{boundary condition;} \end{cases} \qquad 3.1)$$

where $a^2 = \dfrac{k}{\rho c}$ (k — heat conduction, ρ — density, c — heat capacity).

Solution of (3.1) is / 28 /:

$$U = T + 2(T_0 - T)\sum_{n=1}^{\infty} \frac{J_0\left(\mu_n^{(0)}\rho\right)}{\mu_n^{(0)} J_1\left(\mu_n^{(0)}\right)} e^{-\left(\mu_n^{(0)}\right)^2 \theta}; \quad \rho = \frac{r}{r_0}; \quad \theta = \frac{a^2 t}{r_0^2} \qquad (3.2)$$

In (3.2) J_0, J_1 — are first type Bessel functions of zero and first order, in $\mu_n^{(0)}$ — roots J_0 $\left(J_0\left(\mu_n^{(0)}\right) = 0\right)$.

The line in (3.2) quickly converges and, in particular, for r=0 we have:

$$U(r=0, t) = T + (T_0 - T)\cdot\left\{1{,}6e^{-5{,}760} + 0{,}34e^{-30{,}470} + \ldots\right\} \overset{\text{def}}{\approx} T + (T_0 - T)e^{-t/\tau}, \qquad (3.3)$$

whence it follows that relaxation time τ is:

$$\tau = \frac{r_o^2 c\rho}{5,76k}. \qquad (3.4)$$

Using relationship (3.3) we can define radius r_o at specified τ. The calculated values r_o for various materials for $\tau = 10^{-3}$ s are given in Table 3.1.

Table 3.1

Material	k, $W / m \cdot {}^{o}K$	c, $\frac{J}{kg \cdot {}^{o}K}$	ρ, $\frac{kg}{m^3}$	r_o, mm
Chromel	37,7	602	$8,7 \cdot 10^3$	0,2
Alumel	47,7	548	$8,5 \cdot 10^3$	0,24

We have chosen a thermocouple with diameter of wires d=0.2 mm that corresponds to the time constant $\tau < 0.24 \cdot 10^{-3}$.

The influence of the leads on the temperature measuring accuracy may be estimated using a model shown in Fig. 3.3.

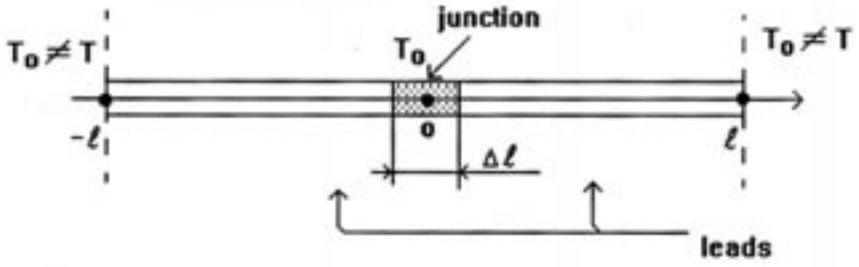

Fig. 3.3

The principle of this model is that if the sources with constant temperature $T \neq T_o$ are applied to the boundaries $x = \pm l$ a system uniformly heated up to the temperature T_o (see Fig. 3.3) at the moment t=0, the time τ during which the temperature T_o is maintained in the junction is considered to be a threshold time for the measuring system. The following approximations are assumed in the model:

а) $\Delta l << l$;

б) thermophysical characteristics of both thermocouple leads are the same.

It should be emphasized that since heat exchange between a thermocouple and an object is not considered in the model, it provides many times lowered values.

Distribution of temperature U along the length is described by the following system:

$$\begin{cases} \dfrac{1}{a^2}\dfrac{\partial U}{\partial t} = \dfrac{\partial^2 U}{\partial x^2} & - \text{heat conduction equation;} \\ U(x, t=0) = T_0 = \text{const} & - \text{initial conditions;} \\ U(\pm\ell, t=0) = T = \text{const} & - \text{boundary conditions;} \end{cases} \qquad (3.4)$$

where $a^2 = \dfrac{k}{\rho c}$.

Solution of (3.4) is:

$$\begin{cases} U(x,t) = T + 2(T_0 - T)\sum_{n=0}^{\infty} \dfrac{(-1)^n}{\omega_n \ell} e^{-a^2\omega_n^2 t} \cos\omega_n x \\ \omega_n = \dfrac{\pi\left(n + 1/2\right)}{\ell} \end{cases} \qquad (3.5)$$

The line in (3.5) slowly converges, therefore the estimation of the coefficient at t in the exponent for $n=0$ gives a rough result. Given in Table 3.2 are the results of calculating the time τ during which $|U(0,t) - T_0| \le 0.01 \cdot T_0$ for various materials and various lengths (ℓ) (the line in (3.6) was broken at $n=50$).

Table 3.2

Material	τ, s	
	ℓ=7 mm	ℓ=10 mm
Chromel	0.43	0.88
Alumel	0.31	0.62

Thus, the estimation analysis made shows that temperature measurements with sufficient accuracy and fast operation may be carried on using chromel–alumel thermocouples with diameter of wire 0.2 mm, pressed in the object surface at length 7 mm.

CHAPTER 4

Arrangement of experimental studies of the electric arc effect on metallic enclosures

It follows from the analysis of regularities of the short−circuit current effect on metallic enclosures that in the experimental studies measures should be taken on the arc reference points stabilization and the arc column localization.

Stabilization of the arc reference points allows to ensure a maximum possible effect on the enclosure and to arrange the influence on any enclosure area set beforehand.

localization of the arc column allows to avoid the early arc extinction and prevents from transfer of the arc column to the other enclosure areas.

In the experimental studies stabilization and localization can be achieved by taking simple enough measures:

- installation of dielectric barriers;
- using rational conductor design.

We propose to carry out experiments in a configuration shown in Fig.4.1.

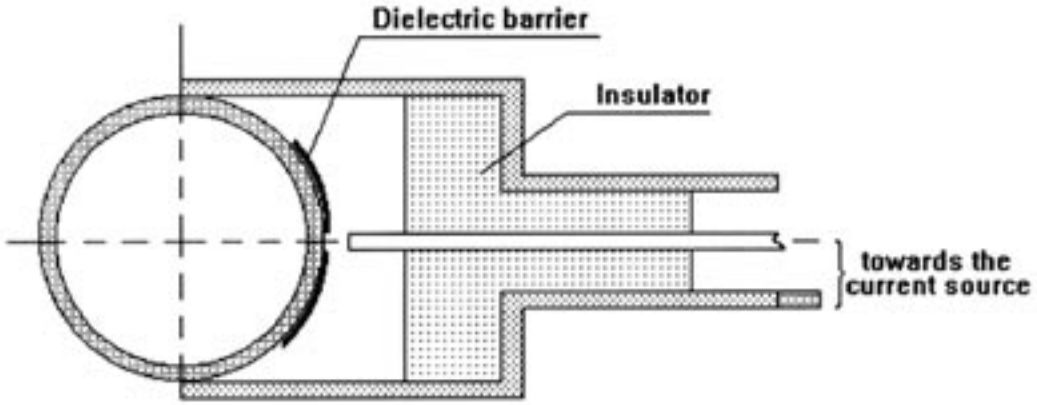

Fig. 4.1 Configuration of an experiment on the arc effect on metallic enclosure

In a configuration proposed the conductors form a balanced system that makes it possible to reduce magnetic field which moves the arc on several orders.

Dielectric barrier thickness is specified so that the time of its burn−out is 15−30 ms. In this case the presence of a barrier does not manifest itself on the

characteristics of the enclosure burn−out, however, it allows to ensure a reference point stability.

References

1. Буткевич Г.В., Белкин Г.С., Ведешенков Н.А. Электрическая эрозия сильноточных контактов и электродов. – М., Энергия, 1978.

2. Таев И.С. Электрические аппараты. Общая теория. М., Энергия, 1977.

3. Сугавара М. Испарение проволочных электродов под действием сильноточного дугового разряда на переменном токе. "Труды Института инженеров по электротехнике и радиоэлектронике", 1967, т.55, №7.

4. Брон О.Б. Электрическая дуга в аппаратах управления. М.,–Л., Госэнергоиздат, 1954, с.532.

5. Бабаков Н.А. Скорость движения короткой электрической дуги.– Электричество, 1948, №2, с.74–77.

6. Бакутко И.А., Бушик А.И., Некрашевич И.Г. Исследование эрозионных процессов на биметаллических электродах методом развертки в магнитном поле. – В кн.: Электрические контакты. М., Наука, 1972, с.82–86.

7. Burkhard G. Uber den Einfluss von Oxidschichten auf die Lichtbogenbewegung im Magnetfeld.– Elektrie, 1966, Bd 20, s.229–232.

8. Eidinger A., Rieder W. Das Verhalten des Lichbogens im transversalen Magnetfeld. – Archiv fur Elektrotechnik, 1957, Bd 43, s.94–114.

9. Таев И.С. Основы теории электрических аппаратов.–М.: Высшая школа, 1987.

10. Shier A. Resistance of electrical fanet arc in very high voltage networks.–Electrical India, 1970, N8.

11. Бургсдорф В.В. Открытые электрические дуги большой мощности.– Электричество, 1948, №10.

12. Отключение токов в сетях высокого напряжения : Пер. с англ./ Под ред. К. Рагаллераю– Мю: Энергоиздат, 1981.

13. Van A., Warrington C. Interesting facts about power arcs.– Relaying News (GEC), 1941, N20.

14. Neugebauer H. Selektivschutz, 1955.

15. Буткевич Г.В. Дуговые процессы при коммутации электрических цепей. Высшая школа, М., 1967.

16. Suits C.G. High pressure in common gases in free convection.– Phys.Rev., 1939, vol.55, N2.

17. Брон О.Б., Гальперин Л.Б. Основы отключения весьма больших токов короткого замыкания. – Электричество, 1940, №4, с.36–39.

18. Буткевич Ю.В. Лаборатория разрывных мощностей ВЭИ.– Электричество, 1946, №11, с.40–44.

19. Каплан В.В., Нашатырь В.М. Коммутационные испытания высоковольтных аппаратов. Л., Энергия, 1969.

20. Каплан В.В., Нашатырь В.М. О применении искусственных линий для испытания высоковольтных выключателей.– Электротехника, 1973, №10, с.55–58.

21. Современные лаборатории разрывных мощностей.– Электротехническая промышленность за рубежом, 1962, с.127.

22. Федченко И.К. Техника высоких напряжений. Киев: Высшая школа, 1969.

23. Шилин Н.В. Научно–исследовательский центр по испытанию высоковольтной аппаратуры.– Электричество, 1967, №9, с.1–10.

24. Болотин И.Б., Эйдель Л.З. Измерения в режимах короткого замыкания. Л., Энергия, 1973.

25. Сипайлов Г.А., Хорьков К.А. Генераторы ударной мощности.

26. Андреев С.И., Ванюков М.П. Применение искрового разряда для получения интенсивных световых вспышек длительностью 10^{-7} – 10^{-6}. ЖТФ, 1961, т.XXXI, вып.8, с.960–974.

27. Кашарский Э.Г., Пипко Р.М., Рутберг Ф.Г. Некоторые вопросы работы ударного генератора на дуговую нагрузку. – В кн.:Генераторы плазменных струй и сильноточные дуги. Л., Наука, 1973, с.121–130.

28. Тихонов А.Н., Самарский А.А. Уравнения математической физики. М., Наука, 1977.

Appendix B

VNIIEF Report on Subtask 2B

RUSSIAN FEDERAL NUCLEAR CENTER

607190 Russia,
Nizhny Novgorod region
Sarov, Mira 37,
RFNC-VNIIEF

Document number 0613OTN30-98
Data 4 November, 1998

This report is accomplished within the framework of contract AV-5840

Contractor
Institute of Experimental Physics
(VNIIEF)

ELECTRIC ARC EFFECT ON EXPLOSIVE SAFETY

(Final report)

(Theoretical estimates and experimental studies of electric arc thermal effect on metallic shells)

The paper presents the results of theoretical estimates and experimental studies of electric arc thermal effect on metallic shells, performed under the contract AV-5840

Investigators:

B. F. Skripnik
N. A. Prudkoi

CONTENTS

CHAPTER 1

Statement of the task

1.1 The objective of this stage was to develop theoretical models for estimating the effect of electric arc of the short circuit current on cylindrical enclosure (see Fig. 1.1).

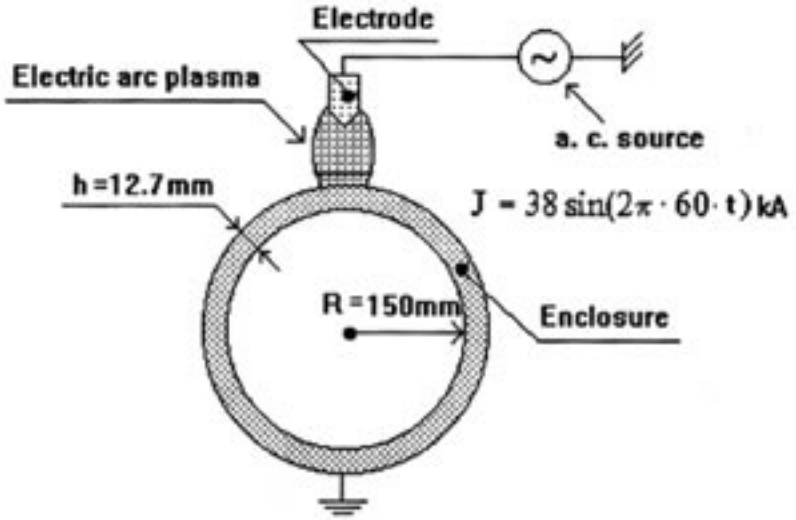

Fig. 1.1

1.2 For computation and theoretical estimations of the electric arc operation geometry of a set problem given in Fig. 1.1 may be simplified if a curvature of the cylinder lateral surface is neglected. It is quite permissible, since

$$h \ll R,\ \sqrt{\frac{k}{\rho c} t_p} \ll R \quad /1/$$

where k, ρ, c – heat conduction, density and heat capacity of cylinder material, respectively; t_p – short circuit current pulse duration.

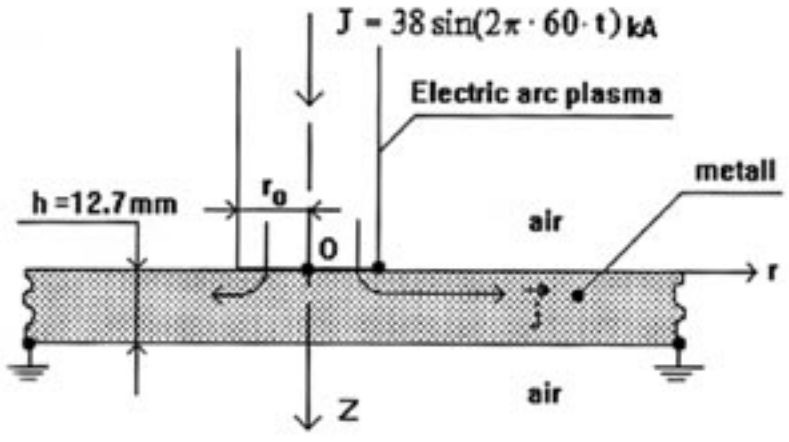

Fig. 1.2

Hence, when building theoretical models, we have limited ourselves to consideration of axially symmetric geometry (see Fig. 1.2).

CHAPTER 2

Theoretical model of a thermal action. Selection of defining parameters

2.1 When the current is flowing through the clearance between the enclosure and the electrode a concentrated energy release occurs in some cathode and anode sections (spots). At currents and durations which are typical of the short circuit a macrobath of melted metal is formed and evaporation and spraying of metal from the entire surface covered with spots begins in the region of the arc effect. As a result, with these conditions the task of estimating the arc effect is reduced to calculation of the average heating of enclosure within the surface covered with spots.

In general, the equation of heat conduction in a solid body, according to /2/, may be written as follows

$$T\frac{\partial S}{\partial t} = \mathrm{div}(k\ \mathrm{grad}T) + f \qquad (2.1)$$

where T – temperature, S – volume unit entropy, k – heat conduction factor, f – heat source density.

It is shown in /2/, that for a solid body with unfixed boundaries the equation (2.1) is reduced to the equation:

$$\rho c_v\left[1+\frac{c_p - c_v}{c_v}\right]\frac{\partial T}{\partial t} = \mathrm{div}(k\ \mathrm{grad}T) + f$$

which, since at constant volume c_v heat conduction in solid bodies is practically undistinguishable from heat capacity at constant pressure c_p, is reduced to the ordinary heat conduction equation

$$\rho c\frac{\partial T}{\partial t} = \mathrm{div}(k\ \mathrm{grad}T) + f\,, \qquad (2.2)$$

where $c = c_p \approx c_v$ – specific heat capacity, ρ – density.

The equation (2.2) is valid both for solid and liquid phase. In calculating the distribution of the temperature being above the melting temperature the equation (2.2) shold be added by the phase interface motion; or in (2.2) heat capacity C should be replaced by effective capacity /3, 4/:

$$\rho\left(c+\lambda\delta(T-T^*)\right)\frac{\partial T}{\partial t} = \mathrm{div}(k\ \mathrm{grad}T) + f \qquad (2.3)$$

where λ – melting heat, T^* – melting temperature.

2.2 For metallic enclosure shown in Fig. 1.2 the two channels of heat inflow can be distinguished, such as a 3–D heat source f defined by Joule–Thomson effects and a surface source q defined by the heat flow from the reference zone of the arc channel.

A 3D source f, according to /5/, is

$$f = \frac{j^2}{\sigma} - T\vec{j}\,\text{grad}\,\alpha \tag{2.4}$$

where σ – metal conductance and α, as shown in /6/ and /7/, may by represented as follows

$$\alpha = \frac{\pi^2 k_B^2 T}{e\varepsilon_F} \tag{2.5}$$

In (2.5) k_b – Boltzmann's constant, e – electron charge, ε_F – electron energy at Fermi level.

A surface source q, if δ – Dirac function is used, may be identified as three–dimensional and may be included in the right part of equation (2.3), however, introduction of q in the system of boundary and initial conditions may be more clearly represented for (2.3):

$$\begin{cases} T(r,z,t=0) = T_o = \text{const} \\ k\dfrac{\partial T}{\partial z} = \mu(T - T_o),\ z=0,\ r > r_o \\ -k\dfrac{\partial T}{\partial z} = q,\ z=0,\ 0 \le r \le r_o \\ -k\dfrac{\partial T}{\partial z} = \mu(T - T_o),\ z=h,\ 0 \le r \le \infty \end{cases} \tag{2.6}$$

In system (2.6) T_0 – initial temperature of the plates, μ – factor of heat exchange with the air.

2.3 To analyze the degree of the heat sources f and q influence on solution of the heat conduction equation, we use the data given in /8/ (see Table 2.1).

Table 2.1

Metall	$T_v(\infty)/T_s(\infty)$	
	$j = 10^8 \frac{A}{sm^2}$	$j = 10^7 \frac{A}{sm^2}$
Al	0.049	0.016
Cu	0.090	0.028
W	0.560	0.177

In Table 2.1 $T_v(\infty)$ and $T_s(\infty)$ – stationary temperatures of the surface, respectively, when heated by 3–D and surface heat sources; j – current density.

It is seen from Table 2.1 that for the high–conducting metals the contribution of 3–D heat source is perceptible only at current densities being higher than 10^8 A/cm^2.

According to theory, current density in the current–conducting channel of electric arc is practically constant and depends only on plasma temperature T_c but not on the magnitude of current flowing in the channel /9/:

$$j \sim \frac{J}{r_o^2} \sim T_c \tag{2.7}$$

This is also confirmed by experimental data /10/. In particular, it follows from /10/ that for pure aluminium and its alloys $j \sim 10^5$ A/cm^2, i. e. we can state that 3–D sources are not significant.

2.4 From (2.7) the radius of the arc channel reference zone may be written as:

$$r_o = k_c \sqrt{|J|} \tag{2.8}$$

The coeeficient k_c is independent on current /9/, and so it follows from (2.8) that with the change of the current magnitude J only the radius of the reference zone r_0 changes.

A comparative analysis of experimental values of k_c based on the data given in /10/ shows that the values of k_c for the alloys D16T, AMr–3M, 1420 differ slightly from the values of k_c for pure aluminium. Therefore, we may preliminary assume that for aluminium alloys

$$\begin{aligned} k_c^{(+)} &= 0.11 \cdot 10^{-3}\ \text{m}/\text{A}^{1/2} \\ k_c^{(-)} &= 0.14 \cdot 10^{-3}\ \text{m}/\text{A}^{1/2} \end{aligned} \tag{2.9}$$

The values $k_c^{(+)}, k_c^{(-)}$ correspond to the cases when a metallic plate–electrode is considered to be anode and cathode, respectively.

A surface heat source q in (2.6) has a power per unit of surface and, for quasidirect currents, is a constant dependent on material and electrode type. For alternate currents we may assume that

$$q \approx \begin{cases} q^{(+)}, & J < 0 \\ q^{(-)}, & J > 0 \end{cases} \tag{2.10}$$

where $q^{(+)}$, $q^{(-)}$ – heat fluxes in the cases when the plate is considered to be anode and cathode, respectively. Suppose that $q^{(+)}$, $q^{(-)}$ for aluminium alloys match the data for pure aluminium /8/

$$\begin{aligned} q^{(+)} &= 2.1 \cdot 10^8 \, W/m^2 \\ q^{(-)} &= 1.8 \cdot 10^8 \, W/m^2 \end{aligned} \tag{2.11}$$

Chapter 3

Linear analytical three and one−dimensional models

3.1 Let us solve the problem on heating and burn−through of metallic enclosure (see Fig. 3.1), assuming that heat conduction and heat capacity of enclosure are independent on temperature, without considering phase transition. The above mentioned limitations form the basis of linear model of the electric arc thermal effect for which one can easily find the analytical solution.

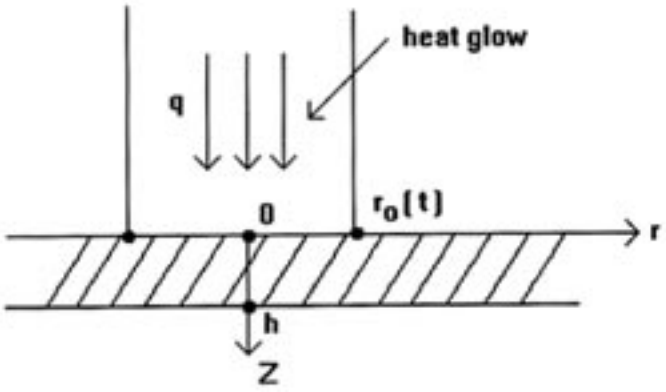

Fig. 3.1

So, assume in (2.3) that $\lambda=0$ and turn from the temperature T to the function $U=T-T_0$, then from (2.3) and (2.6) we obtain

$$\begin{cases} \dfrac{\partial U}{\partial t} = a^2 \Delta U; \;\; a^2 = k/\rho c \\ U(r,z,t=0) = 0 \\ -k\dfrac{\partial U}{\partial z} = q, \;\; z=0; \;\; 0 \le r \le r_0 \\ k\dfrac{\partial U}{\partial z} = \mu U, \;\; z=0; \;\; r > r_0 \\ -k\dfrac{\partial U}{\partial z} = \mu U, \;\; z=h; \;\; 0 \le r < \infty \end{cases} \tag{3.1}$$

Let us make a formal turn from a surface heat source to a 3−D one

$$F = \frac{q}{\rho c}\delta(z) \cdot \begin{cases} 1, \; 0 \le r \le r_0 \\ 0, \; r > r_0 \end{cases} \tag{3.2}$$

and let us distribute conditions of natural heat exchange in the ring $z=0$, $r > r_0$ that is quite permissible, since $\mu \cdot U << q$ up to the temperature of metal evaporation. As a result, we obtain

$$\begin{cases} \dfrac{\partial U}{\partial t} = a^2 \Delta U + F \\ U(r,z,t=0) = 0 \\ k\dfrac{\partial U}{\partial z} = \mu U, \ z = 0 \\ -k\dfrac{\partial U}{\partial z} = \mu U, \ z = h \end{cases} \tag{3.3}$$

Applying Hankel transformation for (3.3) and(3.2), we obtain:

$$\begin{cases} U(r,z,t) = \int\limits_0^\infty p U_p(z,t) J_o(pr) dp \\ F(r,z,t) = \int\limits_0^\infty p F_p(z,t) J_o(pr) dp \end{cases} \tag{3.4}$$

In (3.4) J_0 – zero order Bessel function of the first kind.

Let us substitute (3.4) into(3.3) and turn to cylindrical coordinate system, then after simple transformations we obtain:

$$\begin{cases} \dfrac{\partial U_p}{\partial t} = a^2\left(\dfrac{\partial^2 U_p}{\partial z^2} - p^2 U_p\right) + F_p \\ U_p(z,t=0) = 0 \\ k\dfrac{\partial U_p}{\partial z} = \mu U_p, \ z = 0 \\ -k\dfrac{\partial U_p}{\partial z} = \mu U_p, \ z = h \end{cases} \tag{3.5}$$

Note that for a source F set in (3.2) F_p is /11/:

$$F_p = \frac{q}{\rho c}\delta(z)\frac{r_o}{p} J_1(pr_o) \tag{3.6}$$

where J_1 – first order Bessel function of the first kind.

Let $\{\upsilon_i(z)\}_{i=1}^{\infty}$ be the orthogonal basis, then we may write

$$\begin{cases} U_p(z,t) = \sum\limits_{i=1}^{\infty} T_i(t)\upsilon_i(z) \\ F_p(z,t) = \sum\limits_{i=1}^{\infty} f_i(t)\upsilon_i(z) \end{cases} \tag{3.7}$$

Substituting (3.7) into (3.5) we obtain

$$\begin{cases} \sum_{i=1}^{\infty}\left\{\frac{dT_i}{dt}\upsilon_i - a^2T_i\frac{d^2\upsilon_i}{dz^2} + a^2p^2T_i\upsilon_i - f_i\upsilon_i\right\} = 0 \\ T_i(t=0) = 0 \\ k\frac{d\upsilon_i}{dz} = \mu\upsilon_i,\ z=0 \\ -k\frac{d\upsilon_i}{dz} = \mu\upsilon_i,\ z=h \end{cases} \tag{3.8}$$

Since up to now there existed an arbitrary rule in choosing the orthogonal basis $\{\upsilon_i\}$, suppose for definiteness that $\{\upsilon_i\}$ is a solution of the following problem on eigenfunctions and eigenvalues:

$$\begin{cases} \frac{d^2\upsilon_i}{dz^2} - p^2\upsilon_i = -\lambda_i\upsilon_i \\ k\frac{d\upsilon_i}{dz} = \mu\upsilon_i,\ z=0 \\ -k\frac{d\upsilon_i}{dz} = \mu\upsilon_i,\ z=h \end{cases} \tag{3.9}$$

Thus, substitution of (3.9) into (3.8) gives

$$\begin{cases} \frac{dT_i}{dt} + \lambda_i a^2 T_i = f_i(t) \\ T_i(t=0) = 0 \end{cases} \tag{3.10}$$

It is uneasy to check up, that a solution (3.10) is

$$T_i(t) = \int_0^t e^{-\lambda_i a^2(t-\tau)} f_i(\tau)d\tau$$

In (3.7) F_p is a known function and so, applying orthogonality property of $\{\upsilon_i\}$, we may write that

$$f_i(t) = \frac{1}{\|\upsilon_i\|^2}\int_0^h F_p(z,t)\upsilon_i(z)dz;\ \|\upsilon_i\|^2 = \int_0^h \upsilon_i^2(z)dz$$

Thus, distribution of temperature in the metallic plate is set by the following system

$$\begin{cases} U(r,z,t) = \int_0^\infty dp\, pJ_0(pr)U_p(z,t) \\ U_p(z,t) = \int_0^t d\tau \int_0^h dz'\, F_p(z',\tau)G_p(z',z) \\ G_p(z',z) = \sum_{i=1}^\infty e^{-\lambda_i a^2(t-\tau)} \dfrac{\upsilon_i(z)\upsilon_i(z')}{\|\upsilon_i\|^2} \\ F_p(z,t) = \dfrac{q}{\rho c}\delta(z)\dfrac{r_0}{p}J_1(pr_0) \end{cases} \tag{3.11}$$

Note that q and r_0 in F_p are one−parameter functions of t and the system (3.11) is defined only in the case when there exists a solution of (3.9).

To solve (3.9), we introduce a parameter $\gamma_i = \lambda_i - p^2$ and consider three cases: $\gamma_i < 0$, $\gamma_i = 0$, $\gamma_i > 0$. For the first two cases ($\gamma_i < 0$ and $\gamma_i = 0$) the analysis shows that (3.9) has no nontrivial solutions, and for $\gamma_i > 0$ it is easy to obtain that

$$\begin{cases} \upsilon_i = A_i\left(\cos\omega_i z + \dfrac{\alpha}{\omega_i}\sin\omega_i z\right);\ \alpha \stackrel{def}{=} \mu/k \\ \lambda_i = p^2 + \omega_i^2 \end{cases} \tag{3.12}$$

where the spectrum of λ_i is defined by a range of roots of the equation

$$tg(\omega_i h) = \frac{2\alpha\omega_i}{\omega_i^2 - \alpha^2},\ \omega_i > 0 \tag{3.13}$$

and the relationship $||\upsilon_i||^2/A_i^2$ is

$$\frac{\|\upsilon_i\|^2}{A_i^2} = \frac{h}{2}\left(1 + \frac{\alpha^2}{\omega_i^2}\right) + \frac{\alpha}{\omega_i^2} \tag{3.14}$$

In practice, to define a range of roots of the equation (3.13), it is enough to limit oneself to the approximate solution

$$\begin{cases} \omega_1 \approx \sqrt{\dfrac{2\alpha}{h}} \\ \omega_i \approx \dfrac{\pi i}{h},\ i = 2,\infty \end{cases} \tag{3.15}$$

Finally, substituting (3.12) and (3.14) into(3.11), we obtain that distribution of temperature in the metallic plate along r and z is set by the following formula (3−D linear analytical model):

$$\begin{cases} U(r,z,t)=\dfrac{1}{\rho c}\displaystyle\int_0^t d\tau q(\tau) r_0(\tau)\psi_\tau \sum_{i=1}^{\infty} e^{-a^2(t-\tau)\omega_i^2}\dfrac{\left(\cos\omega_i z+\dfrac{\alpha}{\omega_i}\sin\omega_i z\right)}{\dfrac{h}{2}\left(1+\dfrac{\alpha^2}{\omega_i^2}\right)+\dfrac{\alpha}{\omega_i^2}} \\ \psi_\tau=\displaystyle\int_0^\infty dp J_0(pr)J_1\left(pr_0(\tau)\right)e^{-a^2(t-\tau)p^2} \end{cases} \tag{3.16}$$

In practice, as a rule, of special interest is a calculation of U for $r=0$, therefore, for this case we note that ψ_τ is taken in squarings /12/:

$$\psi_\tau=\int_0^\infty dp J_1\left(pr_0(\tau)\right)e^{-a^2(t-\tau)p^2}=\frac{1}{r_0(\tau)}\left[1-\exp\left(-\frac{r_0^2(\tau)}{4a^2(t-\tau)}\right)\right] \tag{3.17}$$

3.2 In the cases when dimensions of the surface heat source exceed the thickness of metallic enclosure a $1-D$ model is most useful.

Solution of a $1-D$ model is made in the way similar to that described in 3.1 and is given by the following formula:

$$U(z,t)=\frac{1}{\rho c}\int_0^t d\tau q(\tau)\sum_{i=1}^{\infty} e^{-a^2(t-\tau)\omega_i^2}\frac{\left(\cos\omega_i z+\dfrac{\alpha}{\omega_i}\sin\omega_i z\right)}{\dfrac{h}{2}\left(1+\dfrac{\alpha^2}{\omega_i^2}\right)+\dfrac{\alpha}{\omega_i^2}} \tag{3.18}$$

The spectrum of ω_i in (3.18) matches the spectrum in a $3-D$ model, i. e. it is set by (3.15).

3.3 Let us make comparative calculations of the burn−through time of metallic enclosure manufactured from the alloy B93 (enclosures made of this alloy will be employed in experimental studies), using $3-D$ and $1-D$ models. We define the burn−through time as a moment of time when the temperature on the rare side of enclosure in the point $r=0$, $z=h$ will achieve the value of the melting temperature T^*.

In calculations the results of which are presented below in the Table 3.1 the following parameters were used:

$$q^{(+)}=q^{(-)}=\langle q\rangle=1.95\cdot10^8\,W/m^2\ (\text{см.}(2.11))$$
$$k_c^{(+)}=k_c^{(-)}=\langle k_c\rangle=0.125\cdot10^{-3}\,m/A^{1/2}\ (\text{see }(2.9))$$
$$J_0=38\ kA$$
$$T^*=480^\circ C,\ T_0=20^\circ C$$

The infinite sequence in (3.18) and (3.16) terminated at $i=50$.

Table 3.1

T, °C	ρ, $10^3 kg/m^3$	c, $\frac{J}{kg \cdot °C}$	k, $\frac{W}{m \cdot °C}$	burn−through time, s		$\varepsilon = \frac{t_{3d} - t_{1d}}{t_{1d}}$, %
				t_{1d}	t_{3d}	
20	2.84	795	163	0.340	0.349	2.6
200	2.80	963	172	0.392	0.405	3.3
400	2.76	1130	163	0.470	0.485	3.2

In Table 3.1 T is the temperature at which the values of density ρ, heat capacity c and heat conduction k were taken; t_{1d}, t_{3d} − burn−through time in 1−D and 3−D models.

Thus, in building nonlinear model in which a phase transition and melted metal release may be considered at enclosure thicknesses and short−curcuit current parameters typical of the problem under study, it is enough to limit oneself to the 1−D approximation.

Chapter 4

Nonlinear one–dimensional model in view of phase passage and ejection liquid metal

4.1 At currents typical of short circuit (amplitude ≥10 kA, duration ≥ 0.1 c) almost all melted metal formed under the arc effect is removed as a result of spraying defined by electrodynamic forces /1/.

Assuming that the entire energy entering the enclosure is spent only on the metal melting, we may obtain the following expression to estimate the depth of burn–through

$$\delta = \frac{\left(q^{(+)} + q^{(-)}\right)t_u}{2\left(\int_{T_o}^{T^*} c_v \rho dT + \rho\lambda\right)} \approx \frac{\left(q^{(+)} + q^{(-)}\right)t_u}{2\left(c_v\rho\left(T^* - T_o\right) + \rho\lambda\right)} \tag{4.1}$$

At thickness 13 mm the burn–through time for the alloy B93 is

$$t_u = \frac{2\left(10^3 \cdot 2.8 \cdot 10^3 \cdot 460 + 2.8 \cdot 10^3 \cdot 3400 \cdot 10^3\right)}{(2.1 + 18) \cdot 10^8} \approx 0.16c$$

In the small–scale experiments carried out during the instrumentation tests we obtained the burn–through of the aluminium enclosure 2 mm thick for the time 20 ms that agrees with the formula (4.1).

4.2 For numerical calculations a numerical model can be created based on equations (2.3) and (2.6) which for the 1–D case have the following form:

$$\begin{cases} \rho\left(c + \lambda\delta\left(T - T^*\right)\right)\dfrac{\partial T}{\partial t} = \dfrac{\partial}{\partial x}\left(k\dfrac{\partial T}{\partial x}\right),\ x_o \le x \le h \\ T(x, t=0) = T_o \\ -k\dfrac{\partial T}{\partial x} = q,\ x = x_o(t) \\ -k\dfrac{\partial T}{\partial x} = \mu\left(T - T_o\right),\ x = h \\ x_o(t):\ T\left(x_o(t)\right) = T_b \ge T^* \\ x_o(t=0) = 0 \end{cases} \tag{4.2}$$

In the system (4.1) T_b is the temperature at which the metal release occurs. In the finite difference analog (4.1) the release is made by removing the nodes in which $T \ge T_b$ from the calculating grid.

4.3 Before building the finite difference scheme for solving (4.2) we shall make some simplifications. First, let us ignore heat exchange with the air ($\mu=0$:calculations using analytical models with varying the values of μ show that the influence of heat exchange with the air on the temperature distribution picture is not significant). Second, let us introduce new designations and change of variables:

$$\begin{cases} c+\lambda\delta\left(T-T^{*}\right)\overset{def}{=}\tilde{c} \\ T\to U=T-T_{\circ} \\ U\to \upsilon(U)=\int\limits_{\circ}^{U}\rho\tilde{c}dU \end{cases} \tag{4.3}$$

In these designations the system (4.2), as related to the function υ, runs as follows:

$$\begin{cases} \dfrac{\partial\upsilon}{\partial t}=\dfrac{\partial}{\partial x}\left(a(\upsilon)\dfrac{\partial\upsilon}{\partial x}\right),\ a(\upsilon)=\dfrac{k}{\rho\tilde{c}} \\ \upsilon(x,t=0)=0 \\ -a(\upsilon)\dfrac{\partial\upsilon}{\partial x}=q,\ x=x_{\circ}(t) \\ \dfrac{\partial\upsilon}{\partial x}=0,\ x=h \\ x_{\circ}(t):\ \upsilon\left(x_{\circ}(t)\right)=\upsilon_{b}=\int\limits_{\circ}^{T_{b}-T_{\circ}}\rho\tilde{c}dU \end{cases} \tag{4.4}$$

4.3 Let τ be the time step and d be the mesh width, then the absolutely stable finite difference scheme for heat conduction equation in (4.4) is /14/:

$$\begin{cases} \dfrac{\hat{y}_{i}-y_{i}}{\tau}=\dfrac{1}{d}\left[a_{i+1}(y)\dfrac{\hat{y}_{i+1}-\hat{y}}{d}-a_{i}(y)\dfrac{\hat{y}_{i}-\hat{y}_{i-1}}{d}\right] \\ \hat{y}_{i}=y_{i}^{j+1};\ y_{i}=y_{i}^{j},\ a_{i}(\upsilon)=0{,}5\left(a\left(\upsilon_{i-1}\right)+a\left(\upsilon_{i}\right)\right) \end{cases} \tag{4.5}$$

where y_{i}^{j} – finite difference analog of the function υ in the spatial node i at the time layer t_{j}.

Adding (4.5) by finite difference analogs of the initial and boundary conditions from (4.4), we obtain

$$\begin{cases} & \upsilon(x,t=0) \to \left\{ y_i^\circ = 0 \right\}_{i=0}^{N} \\ x = x_\circ(t): & -a\dfrac{\partial \upsilon}{\partial x} = q \to \hat{y}_\circ = \hat{y}_1 + \dfrac{qd}{a_\circ(y)} \\ x = h: & \dfrac{\partial \upsilon}{\partial x} = 0 \to \hat{y}_N = \hat{y}_{N-1} \end{cases} \tag{4.6}$$

Ejection of metal in the finite difference scheme is made by removing the nodes in which the temperature exceeds the release temperature from the scheme. It is performed in a trivial way by introducing in the calculational mesh, instead of "0"−node in the spatial mesh, some reference node i_0 which "keeps track" of the boundary of the arc−metal contact, basing on criterion of the melted metal release (initial value is $i_0=0$). Bearing in mind this fact, further, for more simplicity, all formulas will be written for the stable mesh, since extrapolation for the case of unstable mesh (removing of nodes) does not represent any difficulties.

To solve (4.5), we use a sweep method.

If we introduce a parameter $\gamma=\tau/d^2$ and bring the finite difference analogs of the heat conduction equation and boundary conditions to canonical form:

$$A_i y_{i-1} - C_i y_i + B_i y_{i+1} = -F_i,\ i = 1, N-1$$
$$y_o = \chi_1 y_1 + \mu_1,\ y_N = \chi_2 y_{N-1} + \mu_2$$

then we may create a calculation scheme:

$$
\begin{cases}
j=0 \;:\; \left\{y_i^j\right\}_{i=0}^{N}=0 \\
j>1 \\
A_i=\gamma a_i\left(y^{j-1}\right);\; C_i=1+\gamma\left\{a_i\left(y^{j-1}\right)+a_{i+1}\left(y^{j-1}\right)\right\};\; B_i=\gamma a_{i+1}\left(y^{j-1}\right);\; F_i=y_i^{j-1} \\
\alpha_1=\chi_1=1;\; \beta_1=\mu_1=\dfrac{qd}{a_o\left(y^{j-1}\right)} \\
\chi_2=1,\; \mu_2=0 \\
\overset{(\rightarrow)}{\alpha_{i+1}}=\dfrac{B_i}{C_i-\alpha_i A_i},\; i=1,N-1 \\
\overset{(\rightarrow)}{\beta_{i+1}}=\dfrac{A_i\beta_i+F_i}{C_i-\alpha_i A_i},\; i=1,N-1 \\
\hat{y}_N=\dfrac{\mu_2+\chi_2\beta_N}{1-\alpha_N\chi_2} \\
\overset{(\leftarrow)}{\hat{y}_i}=\alpha_{i+1}\hat{y}_{i+1}+\beta_{i+1},\; i=N-1,0
\end{cases}
\tag{4.7}
$$

4.4 Of interest is the dynamics of the change of the time calculation results of the plate burn−through as various factors, such as nonlinearity of heat capacity, heat conduction, density, phase transition, are included in the calculation model. The results of these calculations are given in Table 4.1. Initial parameters in the calculations were the same as in chapter 3 (see 3.3).

Table 4.1.

t^*, s	remark on considered factors
0.640	phase transition ($\lambda \neq 0$); c(T); k(T); ρ(T)
0.434	$\lambda = 0$; c(T); k(T); ρ(T)
0.462	$\lambda = 0$; c, k, ρ were set at T = 400 °C

Note that the third line in Table 4.1 is a peculiar test for "identity" of the nonlinear numerical model with the linear ones described in chapter 3. Specifically, the results match with high accuracy (0.462 s and 0.470 s).

In calculations the results of which are given in Table 4.1 the release of metal was not considered. This factor was considered in calculations the results of which are given in Table 4.2. These calculations were made using all parameters: nonlinearity of c, k, ρ, plus phase transition. Table 4.2 is presented in a matrix form and illustrates the character of the burn−through time dependence on the

melting temperature T^* and the temperature of release T_b; the time is given in seconds and the temperature – in Celsium degrees.

Table 4.2

T_b \ T^*	480	500	520	540	560	580	600	620	640
480	0.1277	–	–	–	–	–	–	–	–
500	0.174	0.1326	–	–	–	–	–	–	–
520	0.178	0.178	0.1376	–	–	–	–	–	–
540	0.183	0.182	0.182	0.1391	–	–	–	–	–
560	0.187	0.187	0.186	0.186	0.1443	–	–	–	–
580	0.190	0.190	0.190	0.190	0.189	0.1488	–	–	–
600	0.196	0.194	0.194	0.194	0.194	0.193	0.1514	–	–
620	0.200	0.199	0.199	0.198	0.198	0.198	0.197	0.1556	–
640	0.201	0.202	0.203	0.202	0.201	0.201	0.201	0.201	0.1600
740	0.220	0.220	0.220	0.221	0.221	0.220	0.223	0.222	0.221
940	0.257	0.257	0.258	0.258	0.258	0.258	0.258	0.258	0.258
1140	0.293	0.293	0.294	0.294	0.294	0.294	0.294	0.295	0.295
1340	0.327	0.328	0.328	0.329	0.329	0.329	0.330	0.330	0.330
1540	0.360	0.361	0.361	0.362	0.362	0.363	0.364	0.364	0.364
1740	0.391	0.392	0.393	0.394	0.394	0.395	0.396	0.396	0.397
1940	0.421	0.422	0.423	0.424	0.424	0.425	0.426	0.427	0.428
2140	0.448	0.449	0.450	0.452	0.453	0.454	0.455	0.456	0.457

In calculations the temperature dependencies of heat conductivity and heat capacity factors were assumed as for the alloy B93 (Table 4.3).

Table 4.3

T °C	25	100	200	300	400
k, $\frac{W}{m \cdot °C}$	155	159	163	163	159
c, $\frac{J}{kg \cdot °C}$	–	921	1005	1047	1088

The values of k and c in Table 1.1 are taken from references /13, 14, 15/.

Temperature dependence of density is defined through the coefficient of linear expansion.

$$\rho \approx \frac{\rho_0}{1+3\alpha(T-T_0)}$$

where $\alpha = 26.8 \cdot 10^{-6} \cdot C^{-1}$ $\rho_0 = 2840 kg/m^3$ – density at $T_0 = 20°C$ (assumed as for the alloy B93 /1/).

Melting heat was taken to be 393488 J/kg /16/.

Confirmed by Prod Kone 1/15/01
Correct value was used in calculations.

Fig. 4.1 gives the temperature distributions in the enclosure cross−section at various moments (for the alloy B93 $T^* = 500°C$, $T_b = 500°C$).

As follows from the results, the front of enclosure erosion and the temperature front are moving practically in synchronism with each other. The temperature on the internal surface of the enclosure achieves practically significant values only at burn−through of almost the entire enclosure (at burn−through of 80% of enclosure the temperature reaches only 50°C). Also, we observe this effect experimentally (in scale experiments on developing the technique of experimental studies and recording means).

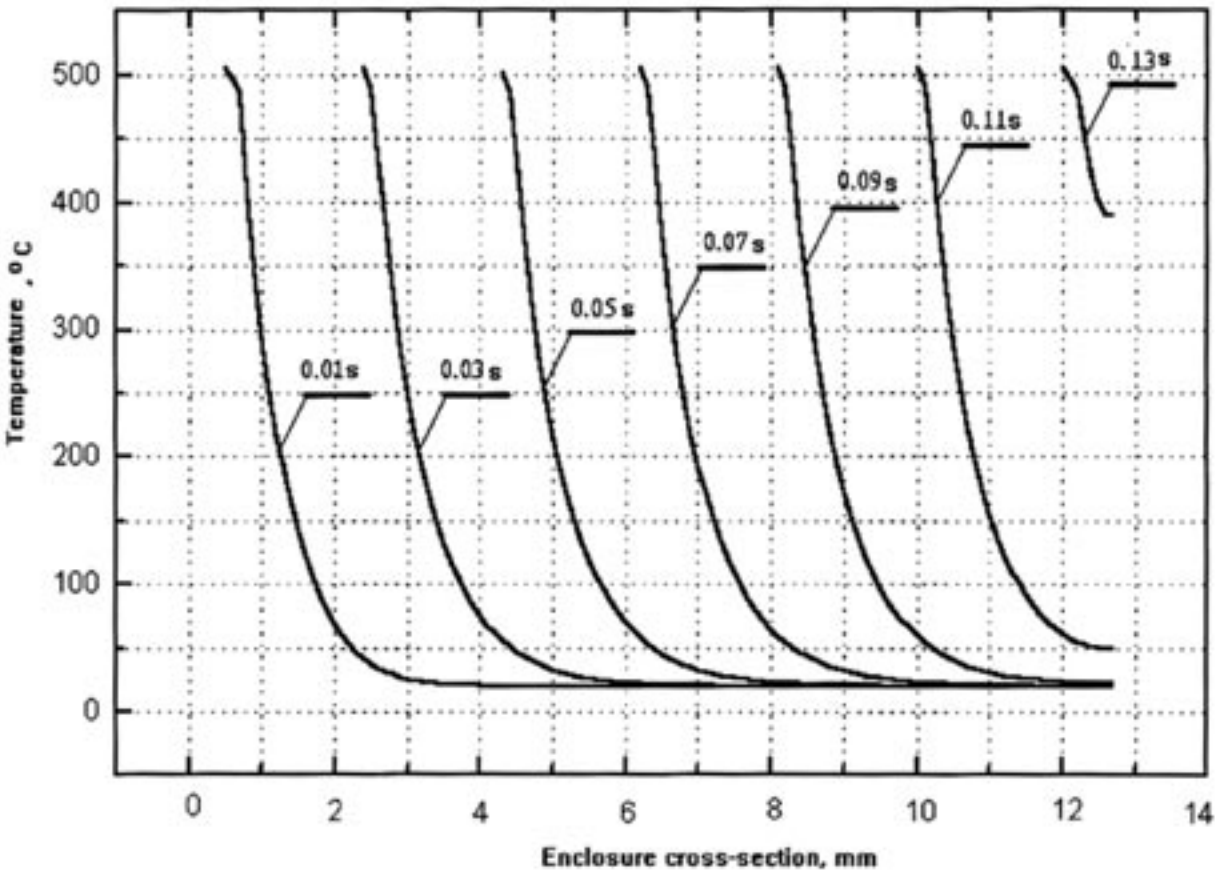

Fig. 4.1

Fig. 4.2 shows the time−temperature history on the internal surface of the enclosure made of the alloy B93 ($T^* = 500°C$, $T_b = 500°C$).

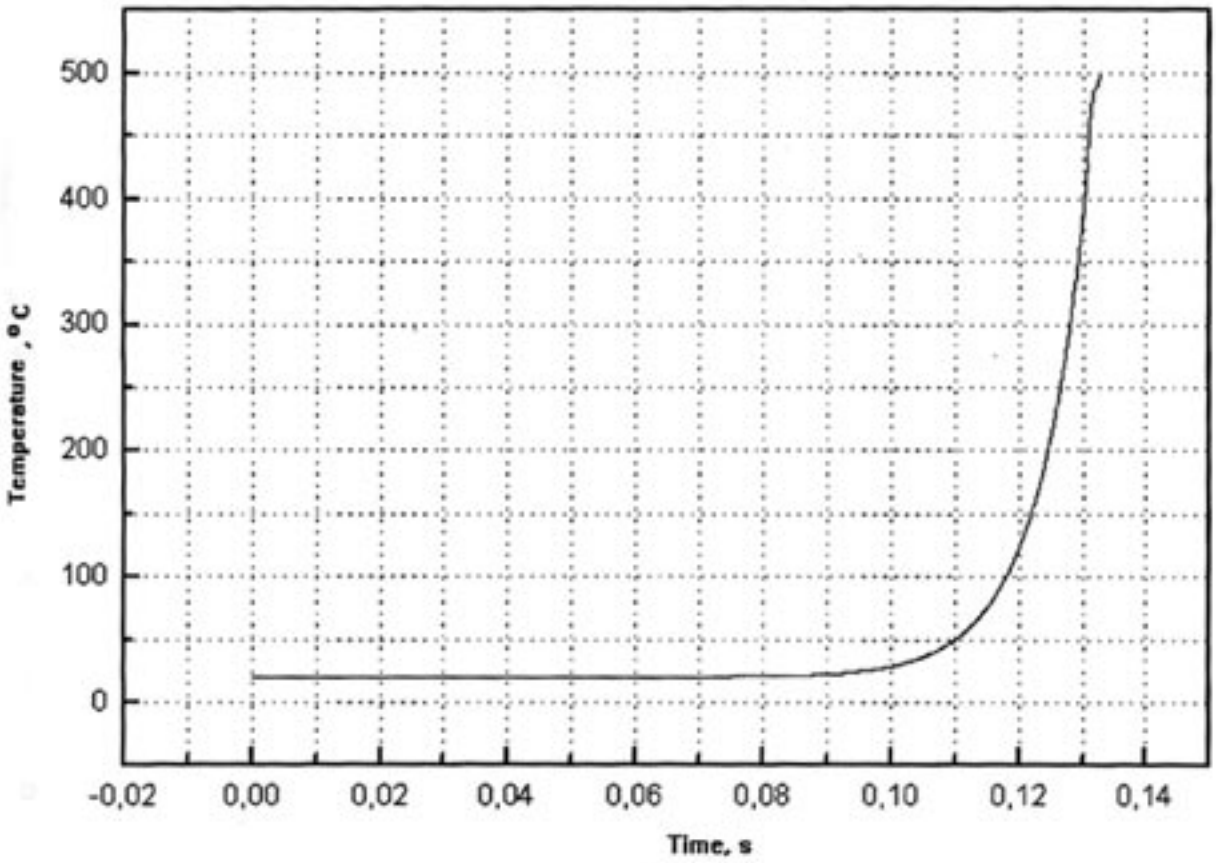
Temperature , °C
500
400
300
200
100
0
-0,02
0,00
0,02
0,04
0,06
0,08
0,10
0,12
0,14
Time, s

Fig. 4.2

CHAPTER 5

Influence of clearance and current on destroying effect of electrical arc

5.1 From energetic considerations follows, that with increase of clearance the energy released in electrical arc is increased. The increase of energy is stipulated by:

– increase of discharge channel length;

– decreasing of metal vapor concentration in plasma of discharge;

– deviation and scatter plasma jets from a direction of a channel of discharge.

On the other hand with the growing of clearance a part of energy running out is increased.

Besides with the growing of clearance the conditions of removing the products of erosion of envelope and electrodes are improved.

All these reasons indicate that with increase of a clearance before certain critical value the destroying effect of an arc will amplify.

Experimentally influence of a clearance was evaluated at researches of erosion of electrodes of switching instrumentation The basic results of these researches are the following. At currents ≈500 A /17/ the influence of a clearance is limited by the size ≈1 mm. At currents ≈10 kA the influence of a clearance is spread up to the sizes of ≈5 mm /18/. In theoretical models the influence of a clearance can be taken into account by introduction effective near–electrode voltage drop and factor of ejection of liquid metal (or temperature of ejection), which depend from a clearance.

However considered in this report a situation of effect (Figure 1.1) is characterized by significant changing a clearance in the process of effect. The total increase of a clearance makes ≈3 cm (1,3 cm – thickness of an envelope, 2 cm – erosion of an electrode /19 /). This size in some times exceeds a clearance, at which the maximum destroying effect is achieved. Therefore, on all visibility, in considered model of effect the relation born–through from a clearance will exhibit rather poorly and it can be not taken into account.

At a current and thickness characteristic of a specific situation of effect (Figure 1.1) theoretical models predict, that the burn–through time of an envelope does not depend on values of a current.

This conclusion will be qualitatively agreed results of experimental researches /20, 21/ of current lightning effect on metal envelopes. In these activities is indicated, that the burn−through charge has minimum value in range of normal currents and sharply is increased both for small, and for large currents. Normalizing border value of range of greater currents forms ≈200−500 A/mm (on evaluations /21/). Taking into account, that the thickness of an envelope makes ≈13 mm, we obtain for the boundary of range of large currents

$$I_{max} = 500 \cdot 13 = 7500A$$

This value is significant less currents specific in model of effect (38 kA).

References

1 Г.В. Буткевич и др. Электрическая эрозия сильноточных контактов и электродов. М., Энергия, 1978.

2 Л.Д.Ландау, Е.М.Лифшиц, Теория упругости, т.7, М., Наука, 1987.

3 А.Н.Тихонов, А.А.Самарский, Уравнения математической физики, М., Наука, 1977.

4 А.А.Самарский, Теория разностных схем, М., Наука, 1977.

5 Л.Д. Ландау, Е.М.Лифшиц, Электродинамика сплошных сред, Т8, М., Наука, 1982.

6 А.Г.Головейко, Теплофизические процессы на аноде в условиях мощного импульсного разряда, ИФЖ, т.XV, N6, 1968.

7 А.Ф.Иоффе, Полупроводниковые элементы, М—Л, изд. АН СССР, 1960.

8 Г.В. Буткевич, Г.С.Белкин, Н.А. Ведешенков, М.А.Жаворонков, Электрическая эрозия сильноточных контактов и электродов, М., Энергия, 1978.

9 Ю.П. Райзер, Физика газового разряда, М., Наука, 1987.

10 Н.Р.Абрамов, И.П.Кужекин, В.П.Ларионов, Характеристики проплавления стенок металлических объектов при воздействии на них молнии, Электричество, N 11, 1986.

11 Г.К.Корн, Т.К.Корн, Справочник по математике, М., Наука, 1977.

12 А.П.Прудников и др. Интегралы и ряды. Специальные функции. М., Наука, 1983.

13 Промышленные деформируемые, спеченные и линейные алюминиевые сплавы, под ред. Ф.И.Квасова и И.Н.Фридляндера, М., Металлургия, 1972.

14 Справочник по авиационным материалам под ред. А.Т.Туманова, т.2, ч.1, М., Машиностроение, 1965.

15 Теплопроводность твердых тел, Справочник под ред. А.С.Охотина, М., Энергоатомиздат, 1984.

16 В.С.Чиркин, Теплофизические свойства материалов, М., Г из—во физ.мат. лит., 1959.

17 El—Roshairy M.A.B. a. oth. Erosion of contacts by arcing. — "Proceedings IEE", Febr., 1961, vol. 108A, p.70—75.

18 Urbanek I. Massenverlust bei Starkstromkontakten. "III International Symposium on Electric Contact Phenomena". University of Maine, Orone, 1966, p.295–299.

19 Electric arc effect on explosive safety (Task N2A – Interim Report). Document number 0613.OTN3–98.

20 Базелян Э.М., Горин Б.Н., Левитов В.И. Физические и инженерные основы молниезащиты. Гидрометеоиздат, 1978.

21 Тихомиров Ю.В., Трунов О.К. Стойкость листовых металлических материалов к термическому воздействию молнии. Электричество, N9, 1986, с.60–61.

Appendix C

Final Report from VNIIEF

RUSSIAN FEDERAL NUCLEAR CENTER

607190 Russia,
Nizhny Novgorod region
Sarov, Mira 37,
RFNC-VNIIEF

Document number 0613OTN30-98
Data 4 November, 1998

This report is accomplished within the framework of contract AV-5840

Contractor
Institute of Experimental Physics
(VNIIEF)

ELECTRIC ARC EFFECT ON EXPLOSIVE SAFETY

(Final report)

(Theoretical estimates and experimental studies of electric arc thermal effect on metallic shells)

The paper presents the results of theoretical estimates and experimental studies of electric arc thermal effect on metallic shells, performed under the contract AV-5840

Investigators:

B. F. Skripnik
N. A. Prudkoi

CONTENTS

CHAPTER I

Experimental method for studying electric arc effect on metallic shells

1.1. Experimental set up

The analysis of short circuit (SC) current effect on metallic shells performed in /15/ showed that in accidents there could be situations in supply lines, when an electric arc can be very destructive. These situations are characterized by stabilization of reference points and localization of the arc column during the entire time of it arcing. Stabilization of the arc reference points allows the maximum possible effect on the shell to be implemented. Localization of the arc column prevents a before time arc failure and stops switchover of the arc column into other portions of the shell.

Thus the experiments implemented the situation of a localized effect. To stabilize arc reference points and localize the arc column the experiment met the requirements related to the option of rational electrode shape (end rounding) and rational design of current conductors.

The experimental schematic is shown in Fig.1.1.

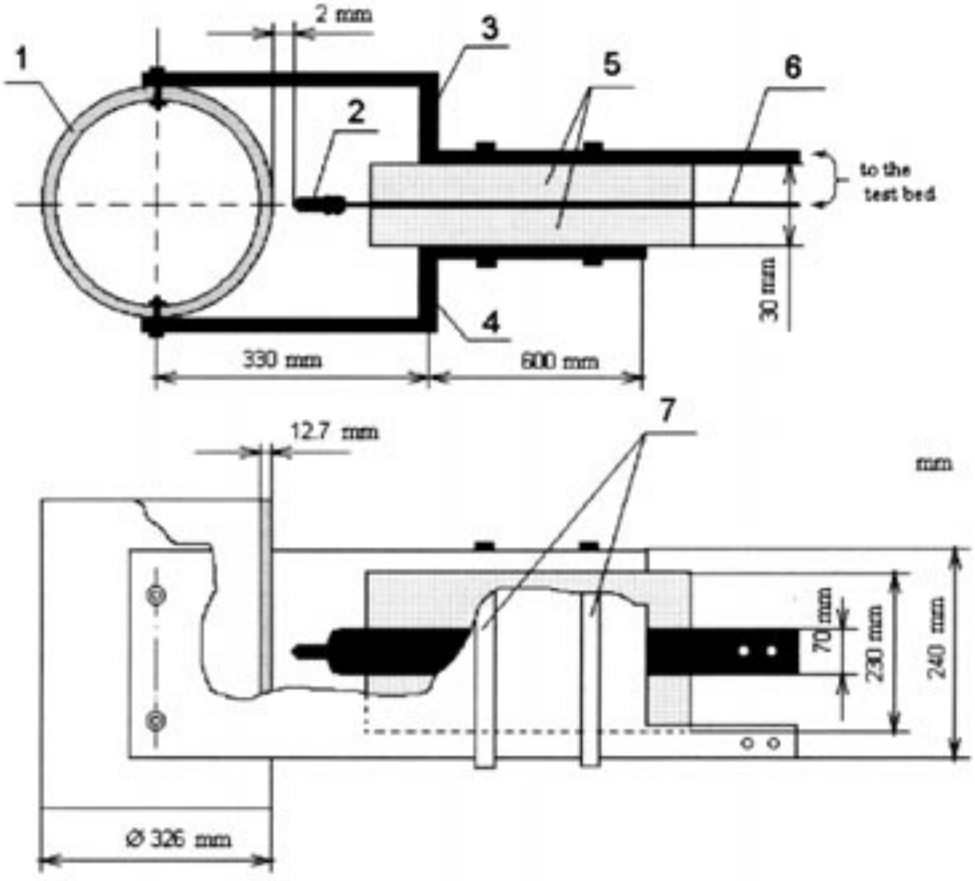

Fig.1.1 Experimental schematic. Arc effect on a metallic shape

In the experiment the arcing takes place between the copper electrode 20 mm diameter (position 2) and a metallic shell formed as a hollow cylinder (position 1). The electrode end facing the shell is made as a hemisphere 10 mm radius. The current is delivered to the arc by a bus system (positions 3,4,6), forming a symmetric strip line. A central bus (position 6) is made of copper strip with the cross section 70x6 mm^2. It is connected with the electrode (position 2). Lateral buses (3,4) are made of steel strips 4 mm thick and 240 mm width. They are fixed by jumpers (7) providing mechanical strength and electric contact between strips. Buses (3 and 6) have holes to be connected to the test bed. The layers of fiberglass laminate are used for insulation purposes

The picture of the gap, where arcing takes place, is given in Fig. 1.2. The total view of the experiment in situ is given in Fig.1.3.

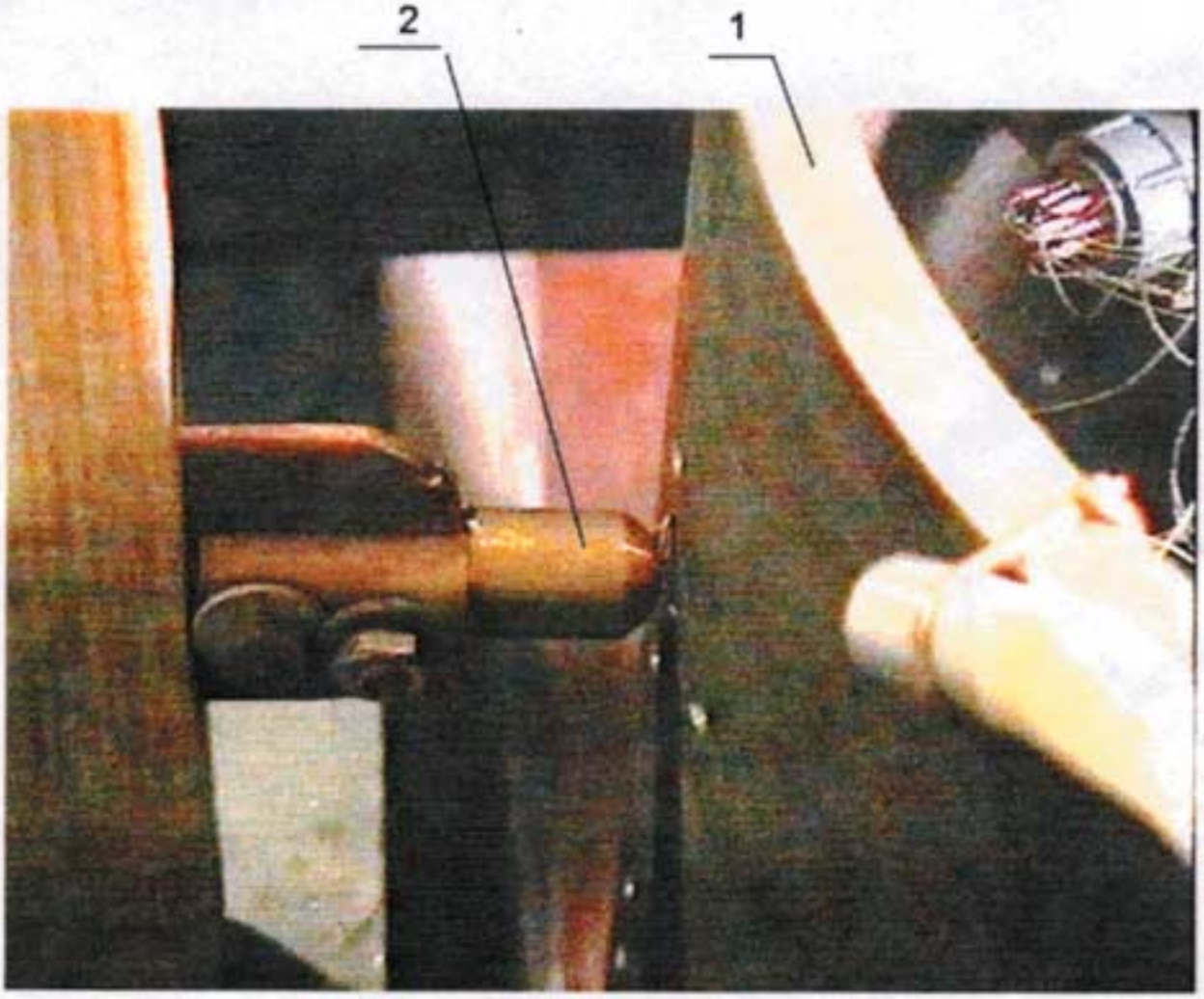

Fig. 1.2. Arc gap picture:
1 is metallic cylinder affected by an arc, 2 is electrode

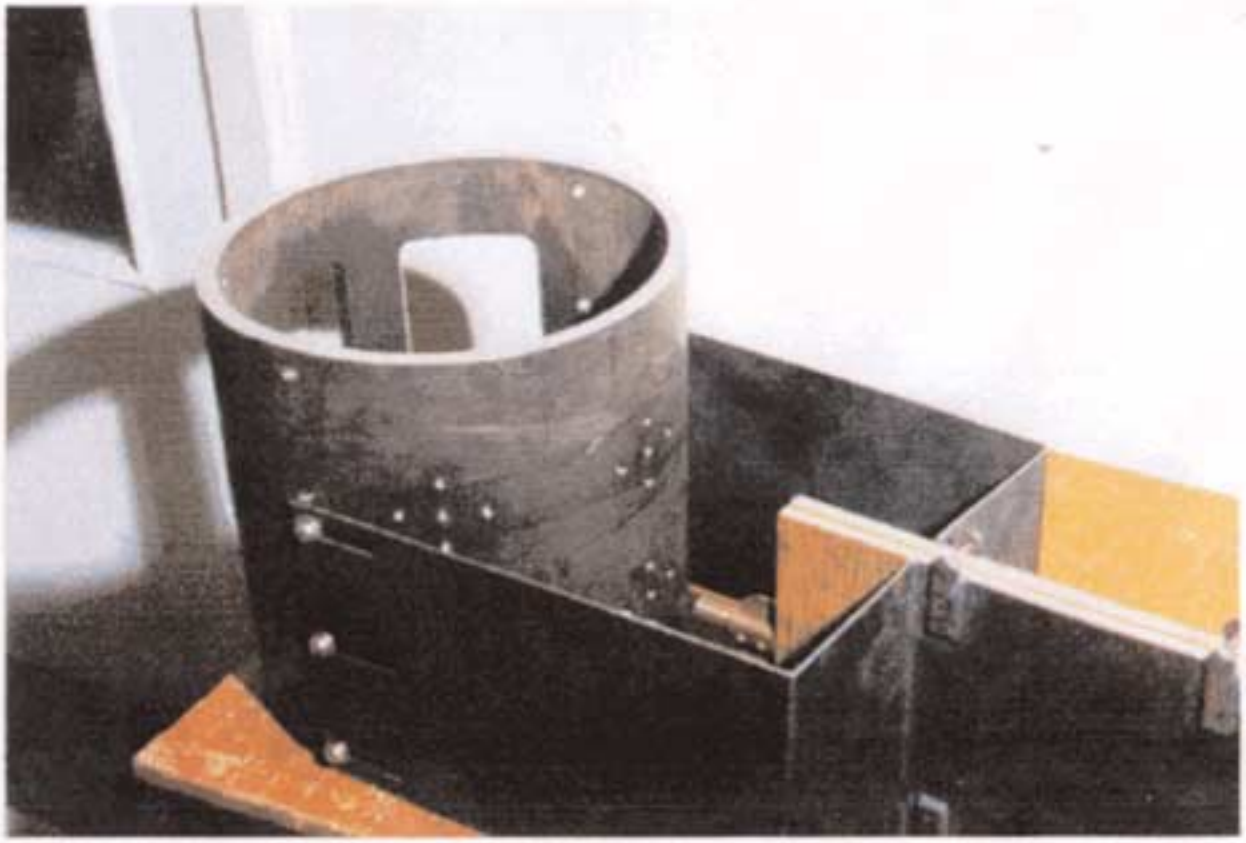

Fig. 1.3. General view of the experiment

1.2. Simulation of short closed currents

To simulate SC currents we used the test bed of All Russia Electrotechnical Institute (Moscow) based on the generator TI-100-2 (Fig. 1.4). The test bed provides the SC currents (working meaning) higher than 100 kA at a duration of $\leq$ 0.3 s. The system of SC simulating is shown in Fig.1.5. Current value is controlled by the change of reactor R inductance and of SG generator voltage (as a result of current excitation change). Switches S1 (on) and SO (off) provide the required duration of SC current. The arc was initiated by the exploding wire W (copper wire 0.2 mm diameter). At the initial moments of initiation the arc has high resistance. In order not to quench it the source voltage (operating value) was agreed to be 2 kV and more. During the test arc current and value were measured by standard measuring means (induction measuring device P, ohmic voltage divider D).

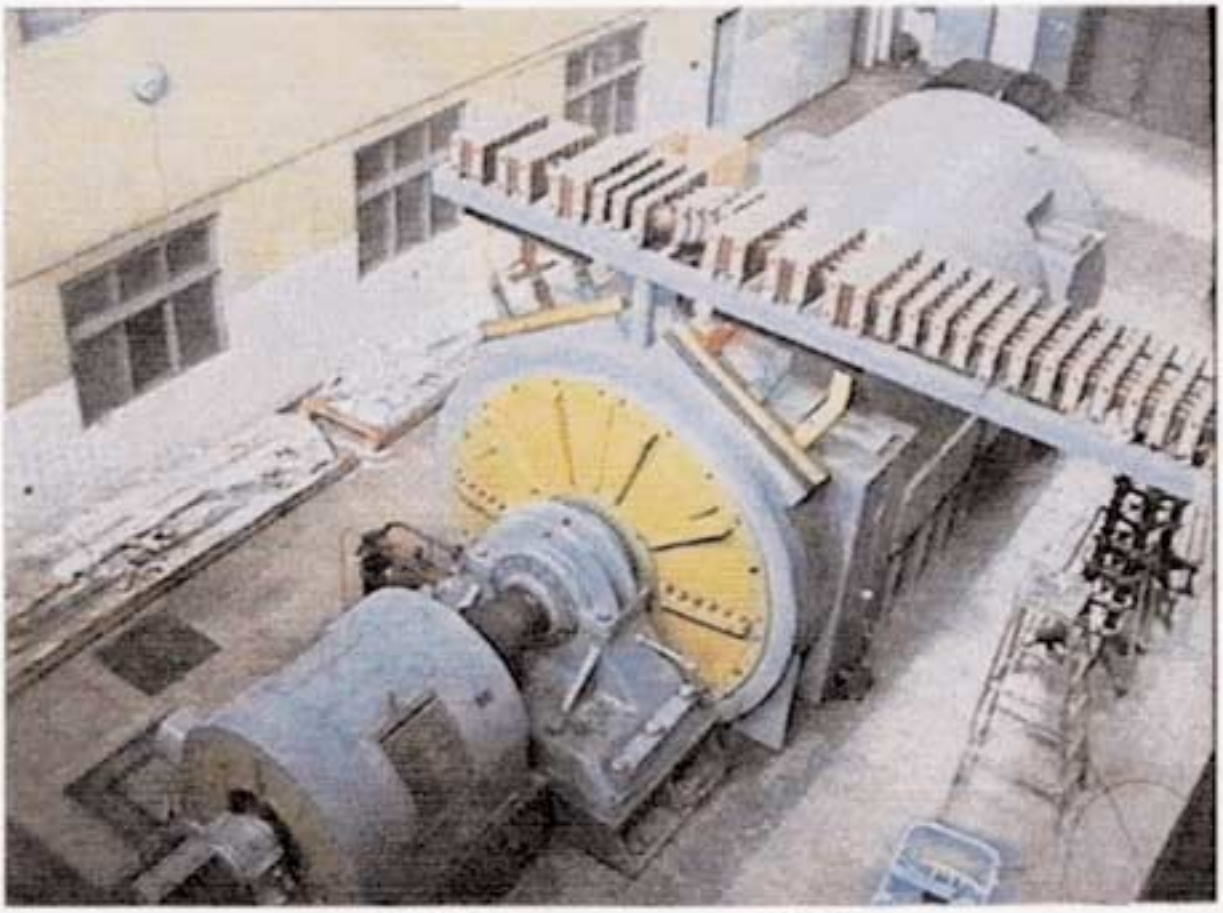

Fig.1.4. Short-circuit generator TI-100-2

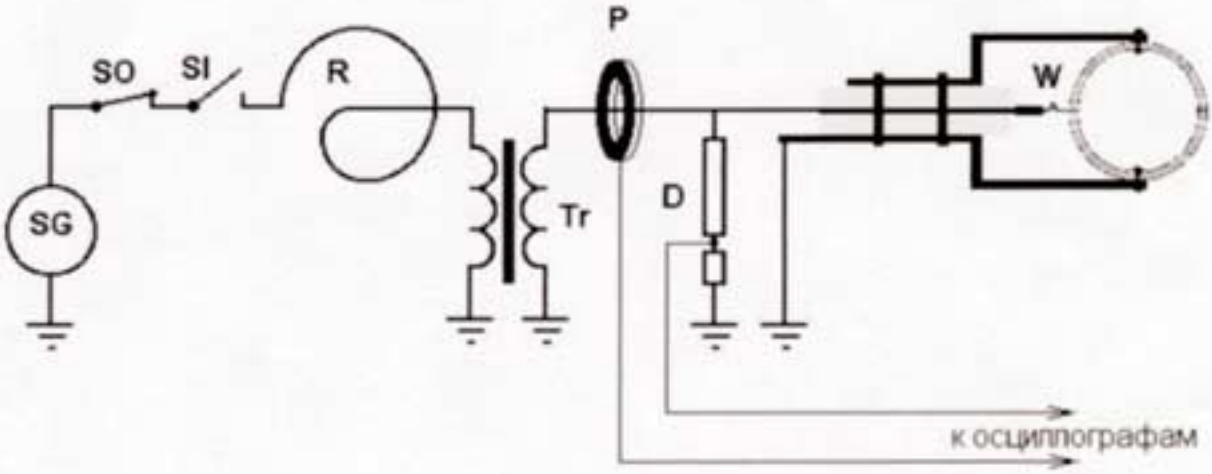

Fig.1.5. System of SC current simulation:

SG is short-circuit generator; R is current-limiting reactor with controlled inductance; SI is switch on; SO is switch off; W is initiative wire; P is a probe for arc current measuring; D is a divider for arc voltage measuring; Tr is matching transformer

1.3. Temperature measurement

When the arc affected the shell the temperature of the inner shell surface was measured. For that purpose we used probes made of thermocouple chromel-alumel with the diameter 0.2 mm. Thermocouples were fixed by molding at the length 7 mm for the depth 0.5 mm. 5 probes were located at each assumed point of effect. A schematic of probe location (cylinder inside) is shown in Fig. 1.6. The external view of the shell fragment with the probes is shown in Fig. 1.7.

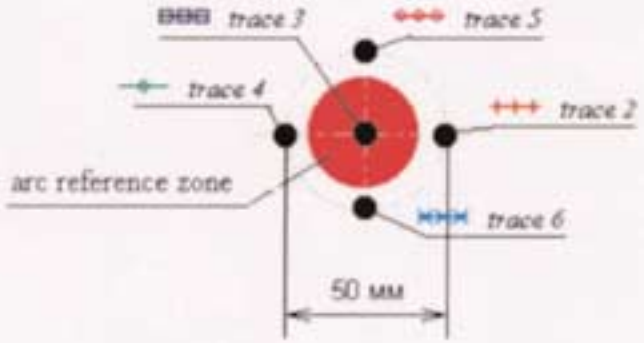

Fig. 1.6 Temperature probe location.

The numbers trace 2, trace 3 etc., correspond to the numbers of measuring channels with the probe connected.

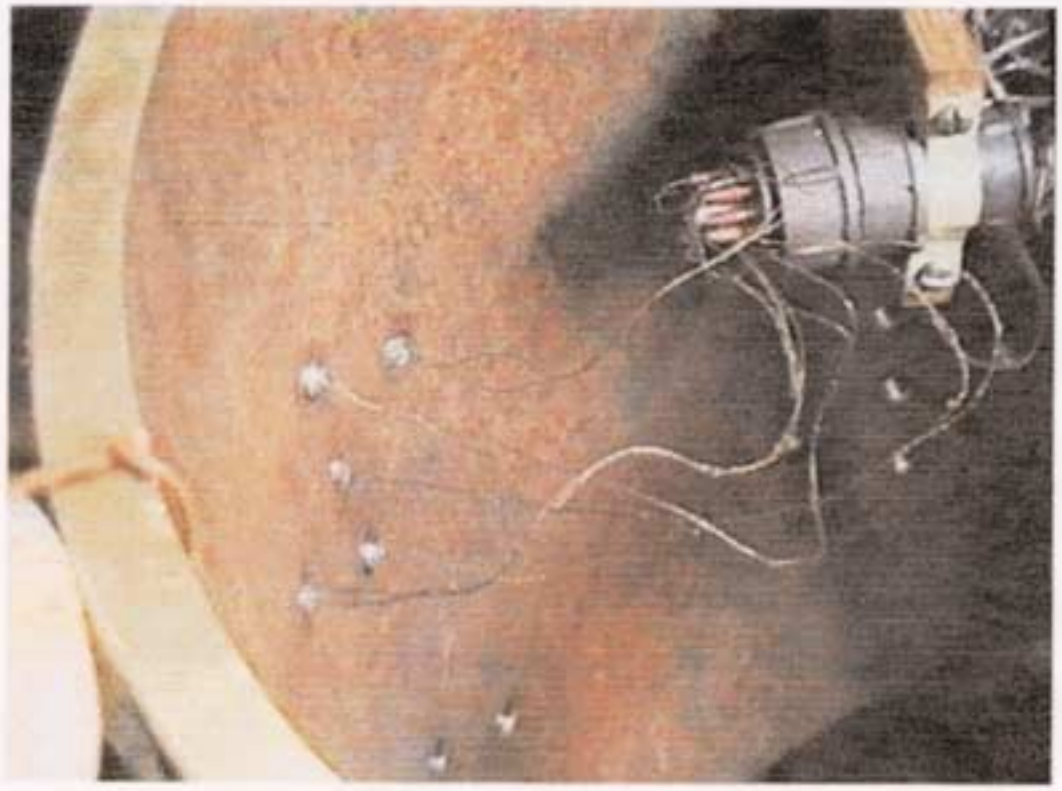

The measuring system is given in Fig. 1.8. The signals from five thermocouples came to the input of the channel amplifier with the gain 20. Each channel has a differential input for thermocouple connection. The signals from amplifier outputs were delivered to the inputs of a multichannel recorder. For timing we used the first channel of a recorder, where a synchronized signal came from the test bed. A dividing transformer provided power supply to amplifiers and a recorder. The recorder was controlled by a remote control using an isolation based on optical transistors.

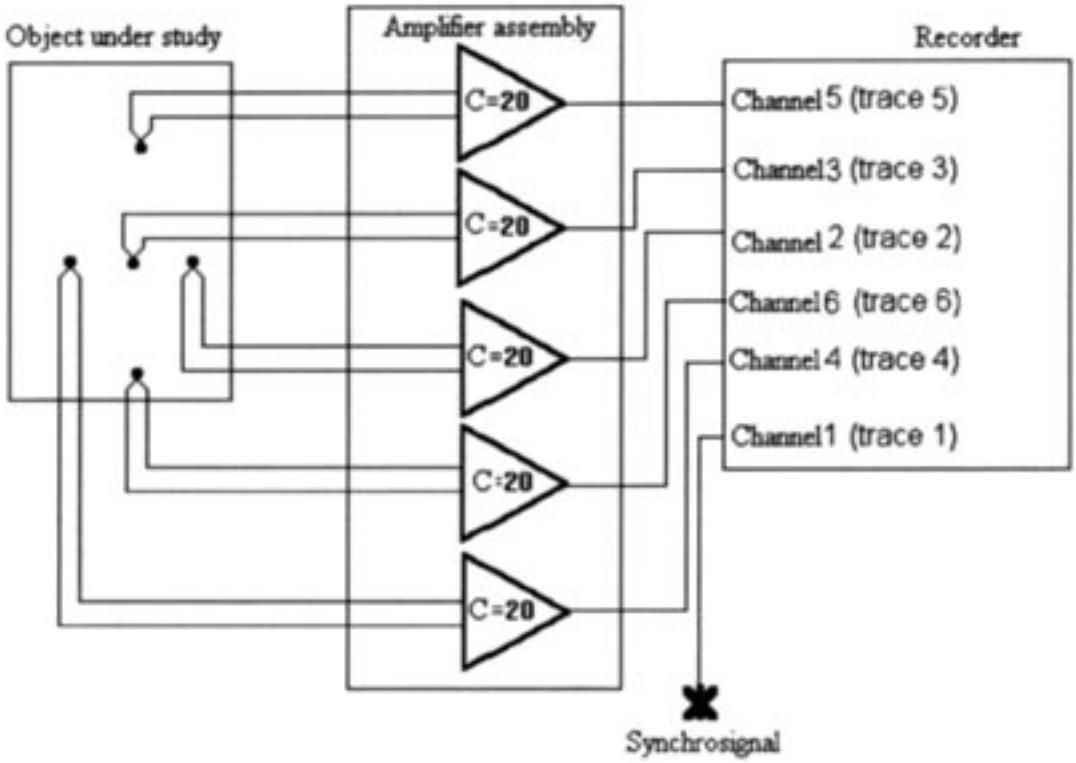

Fig.1.8. Temperature measuring system

1.4. Visualization of an arc effect

Visualization of electric arc effect on samples and the study of processes timing was made using a high speed movie camera. In the experiments we used Russian precision 16-mm video camera PUSK-16. The movie camera has an objective with the focusing distance F=15 mm and the relative opening 1:2.8. The frame size is 6.2x10 mm. We used a black and white film of a KH3 type with the light sensitivity 90. The frequency of operation was 1000 and 2500 frames/sec., relative pulse duration was 10. Exposure time was 100 and 40 μsec, respectively The frequency of crystal controlled markers was 1 kH. We used light filter FS-6 to remove extra light. The beginning of the process was determined by the moment of arcing.

A movie camera looked at the inner side of the sample through special windows (position 2 Fig.1.9) at the lateral surface. The burning through the sample wall was determined by the luminosity of the inner surface.

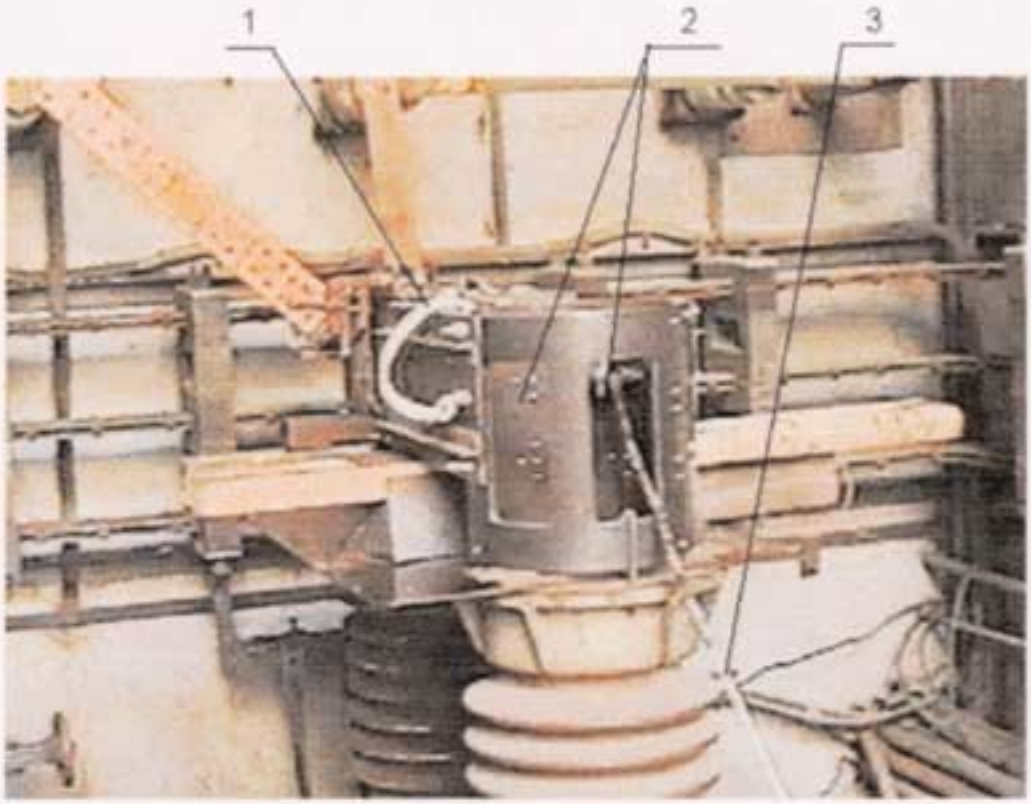

Fig. 1.9. Experimental assembly in situ:
1 - is fiber optic, 2- is windows for filming the fusion process; 3 - cables of temperature measuring channels

To avoid damage of a camera by drops of melted metal it was located at least 5 m from the sample which deteriorated the scale of shooting. The experiment was also filmed from the distance 25 m. After each shot the region of the sample affected by the arc charge was photographed.

1.5. Synchronization of equipment involved into experiment

Synchronization of diagnostic means and a test bed was performed the following way. First the high speed movie camera started operation. It gave the order to trigger the test bed. The test bed came into action with a delay of 20 to 30ms. At the same time with the test bed action the generator responsible for a test bed provided a synchronization pulse to fix measurements of temperature and arc current. The external view of the shell fragment with the probes is shown in Fig. 1.7. The spacing of the monitoring facility is given in Fig. 1.8. 10 -

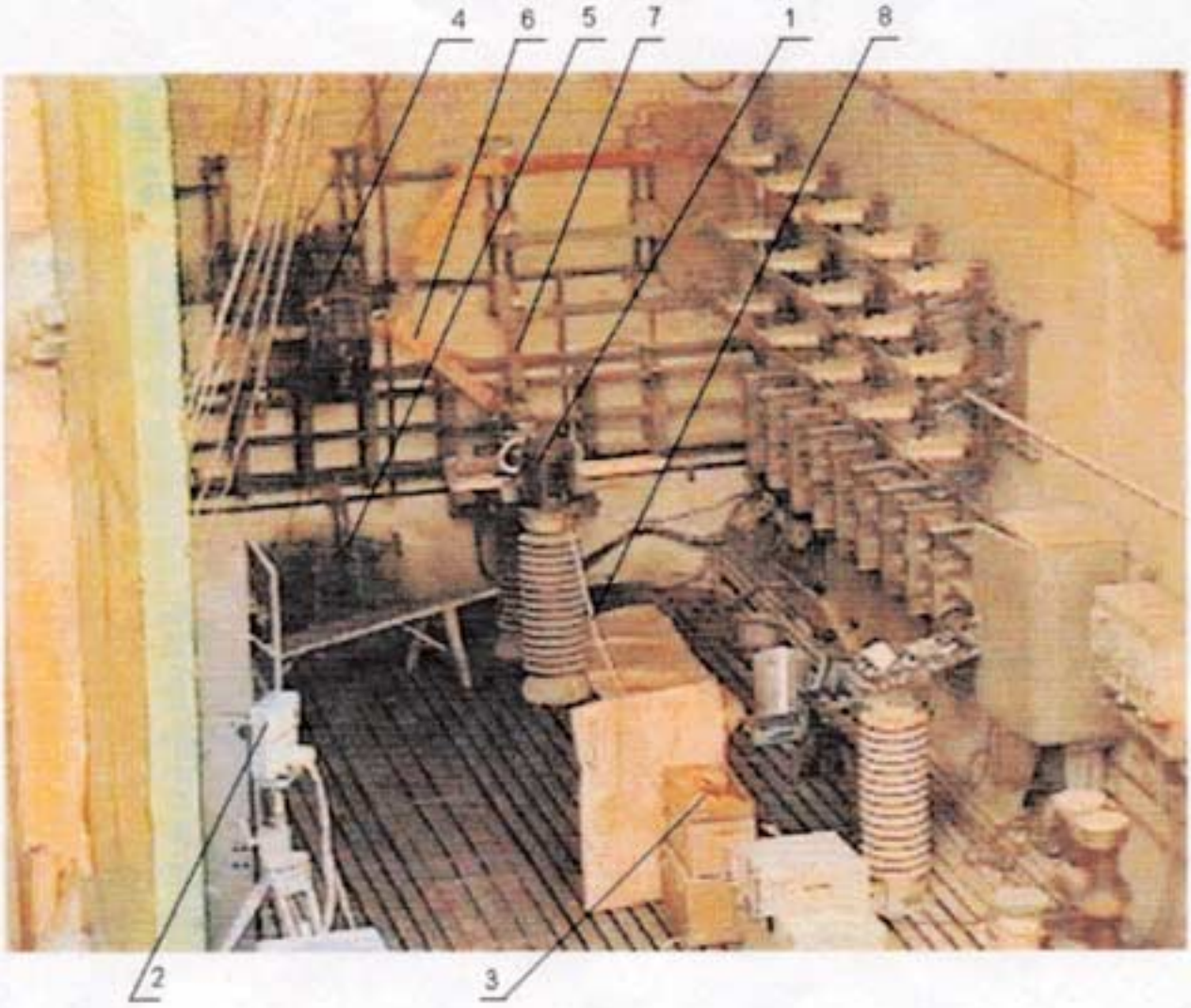

Fig. 1.10 The spacing of the monitoring facility:

1 is experimental assembly (test object);

2 is video camera;

3 is multichannel temperature recorder;

4 is current measuring device;

5 is voltage divider;

6,7 are buses connecting the experiment and the test bed;

8 are cables of temperature measuring channels

CHAPTER 2

Results of the experimental study

The experiments were performed with the cylinders made of steel (steel 12X18H10T, the percentage: chromium 18%, nickel 10%, titanium < 1%; carbon 0.12%)* and aluminum(alloy B93, the percentage: zinc 6.5 - 7.3%, magnesium 1.7 - 2.8%, copper , 1%; iron 0.2 - 0.4%)*. The current amplitude varied from 11 to 37 kA. We performed 12 shots; 6 with steel cylinders and 6 with aluminum. The sample under effect is shown in Fig. 2.1.

Fig. 2.1 Sample (aluminum cylinder) affected by the arc

It was determined that the shell affected by the arc is subject to the intensive destruction. In case of aluminum cylinders the holes were measured even when current duration was 50 and more ms. For the steel aluminum cylinders such holes were measured, when the duration was ≈130 ms. The typical sample damages affected by the arc are shown in Fig. 2.2 - 2.3. The summary of the experimental data is presented in the table 2.1. The detailed summary of the experimental data is presented in the sections 2.1-2.12.

* percent by mass

Fig. 2.2. Aluminum cylinder after the arc effect (I_{max}=19.4 kA, t=150 ms).
Internal appearance

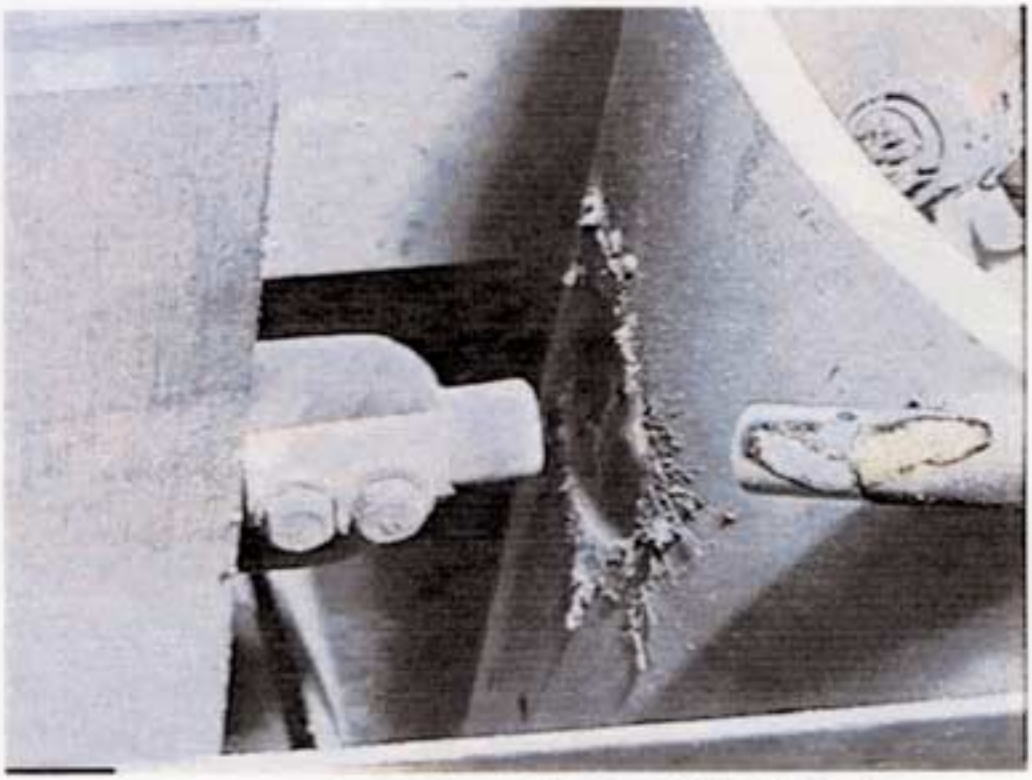

Fig. 2.3. Aluminum cylinder after the arc effect (I_{max}=19.4 kA, t=150 ms).
View from the side of the discharge gap. This picture should be compared with Fig. 1.2, where the same geometry is shown before arc effect.

Table 2.1

Data results

Shot №	Material	Current amplitude, кА	Arc voltage*, V	Current duration, ms	Damage	Time of burning through the hole, ms	Inner surface temperature °C
1	Steel	18.5	81-96	170	Crater: diameter** - 40 mm, depth - 10.5 mm	----------	160
2	Steel	11.3	Not measured	200	Crater: diameter **- 34 mm, depth - 9 mm	----------	196
3	Steel	36.9	Not measured	200	Through hole: outer diameter **- 57mm, inner diameter **- 15mm	130±10	----------
4	Aluminum	19.4	Not measured	200	Through hole: outer diameter **- 56mm, inner diameter **- 38mm	52±1	----------
5	Aluminum	19.4	70-90	150	Through hole: outer diameter**- 55mm, inner diameter **- 31mm	79±1	----------
6	Aluminum	19.4	55-85	100	Through hole: outer diameter**- mm, inner diameter **- 13mm	89±1	----------
7	Aluminum	36.9	85-95	50	Crater: diameter **- 55,5 mm, depth - 12mm	----------	145
8	Aluminum	36.9	85-100	70	Through hole: outer diameter**- 55mm, inner diameter **- 25mm	48±1	----------
9	Aluminum	36.9	85-95	60	Crater: diameter **- 48 mm, depth - 12.5mm	----------	195
10	Steel	36.9	115-165	150	Through hole: outer diameter**- 54mm, inner diameter **- 8mm	126±1	----------
11	Steel	36.9	100-135	130	Crater: diameter **- 51 mm, depth - 12.5 mm	----------	200
12	Steel	36.9	90-145	170	Through hole: outer diameter**- 58mm, inner diameter **- 10mm	125±1	----------

* During attack the arc voltage increases, since the length of an arc column increases as a result of erosion of a cylinder and an electrode.

** An average value betueen the smalest and largest hole diameters.

2.1. Shot # 1

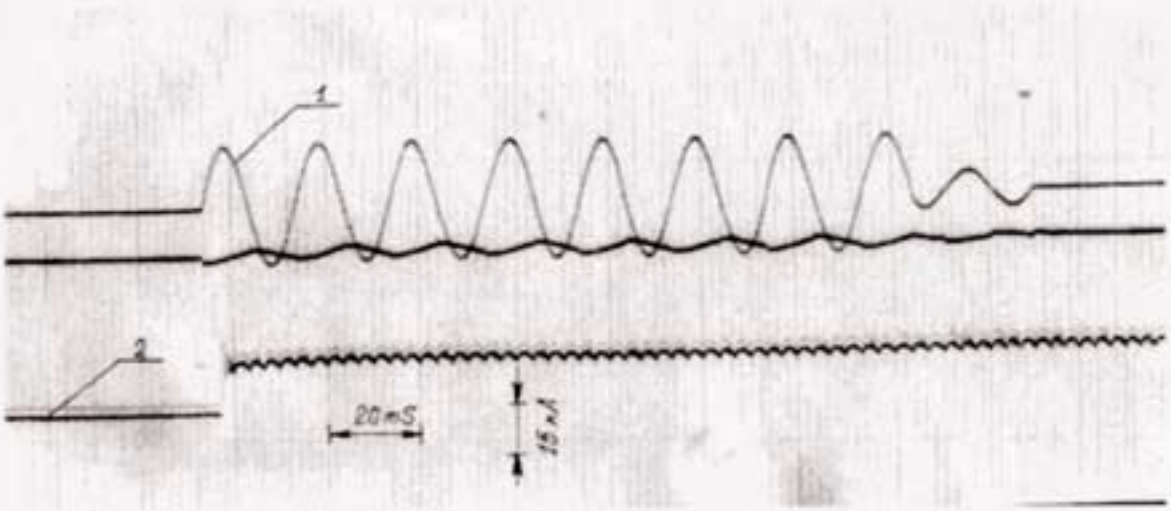

Fig.2.4. Shot # 1 (I_{max}=18.5 kA, t=170ms, steel).

Arc current oscillogram: 1 is arc current, 2 is sinchrosignal

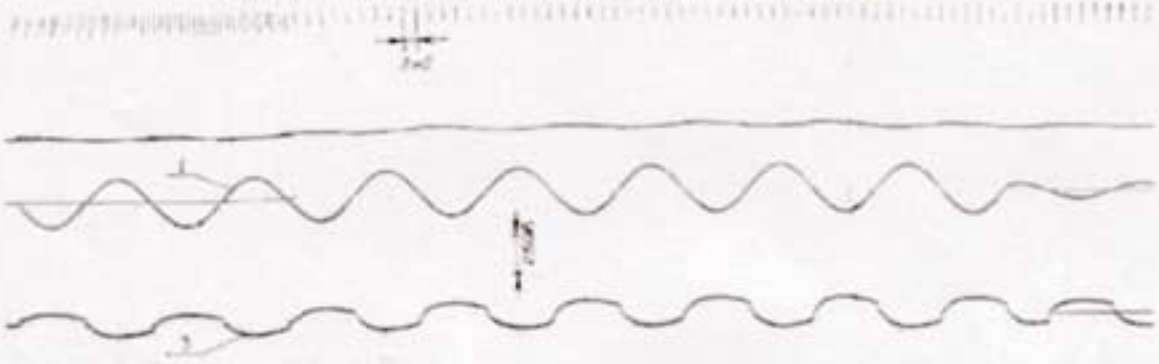

Fig.2.5. Shot # 1 (I_{max}=18.5 kA, t=170ms, steel).

Arc voltage oscillogram: 1 is arc current, 3 is arc voltage

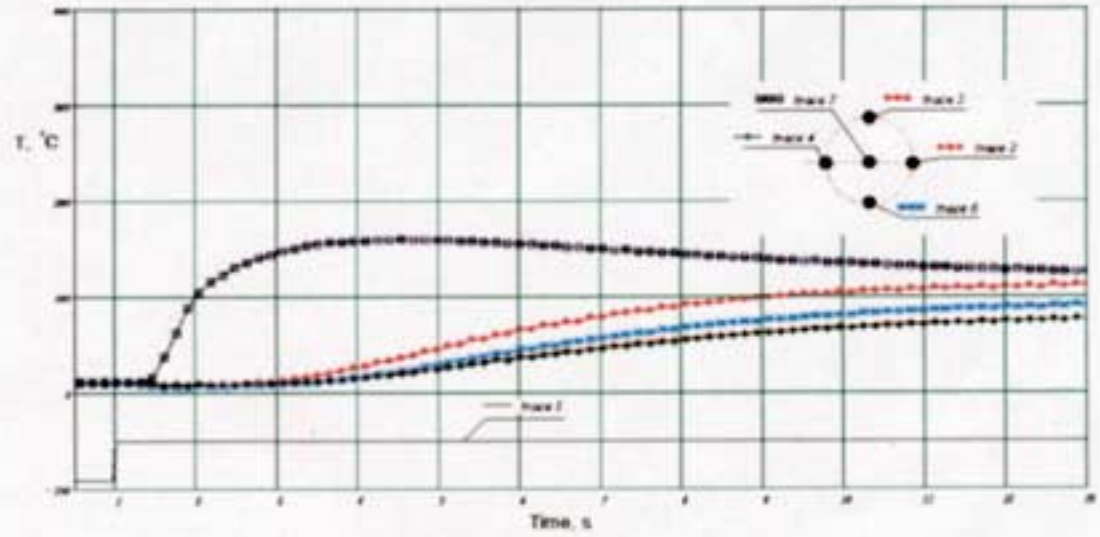

Fig.2.6. Shot # 1 (I_{max}=18.5 kA, t=170ms, steel).

Results of temperature measurement of the inner cylinder wall: trace 1 is sinchrosignal (pulse onset agrees with the beginning of the synchrosignal in the arc current oscillogram); trace2, trace 3, trace4, trace5, trace6 are temperature records at the probe locations (pointed by black circles)

Fig.2.7: Shot # 1 (I_{max}=18.5 kA, t=170ms, steel).
Picture of the cylinder region affected by the arc.

2.2. Shot # 2

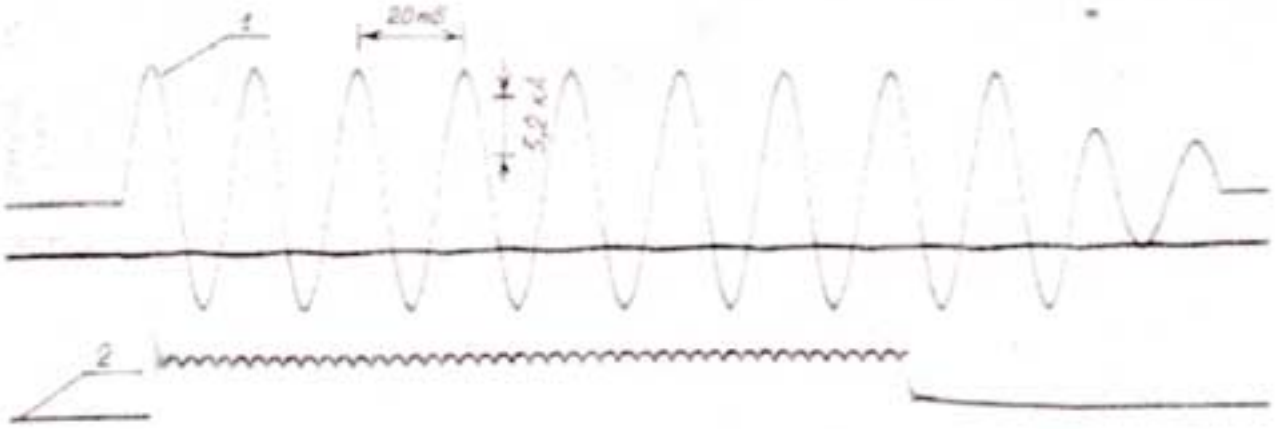

Fig.2.8. Shot # 2 (I_{max}=11.3 kA, t=200ms, steel).
Arc current oscillogram: 1 is arc current, 2 is sinchrosignal

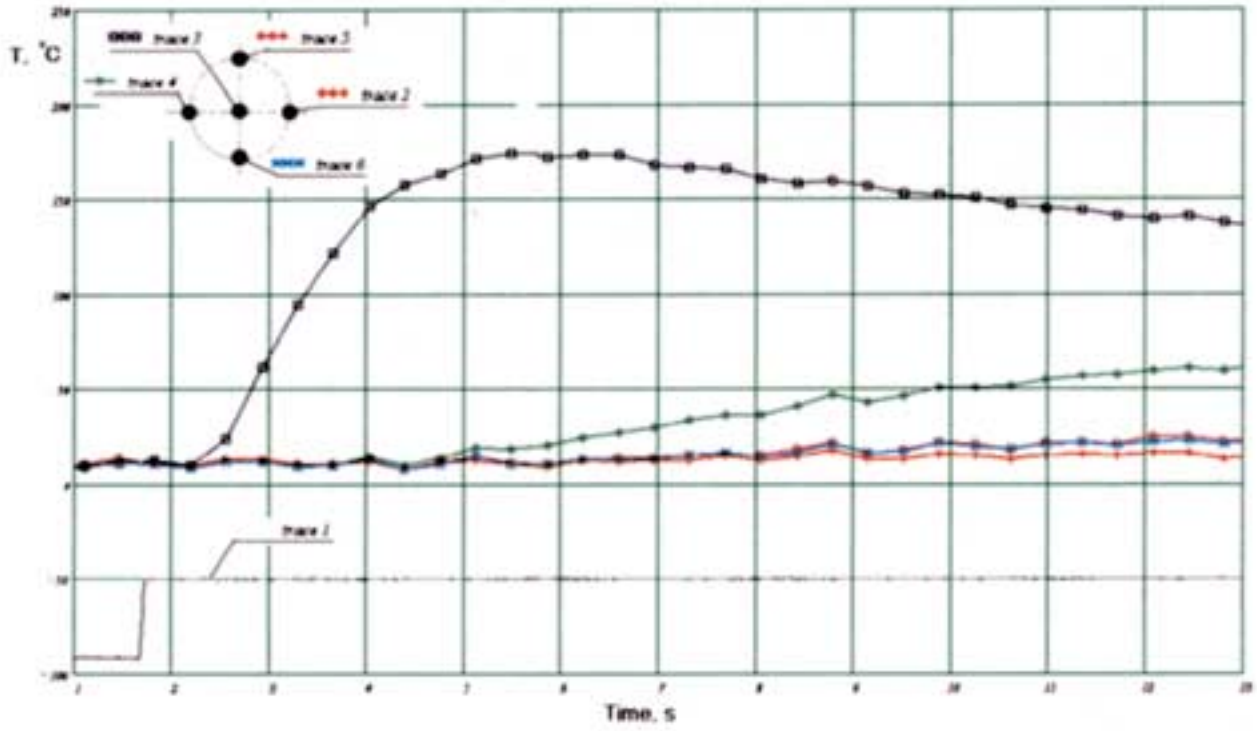

Fig.2.9. Shot # 2 (I_{max}=13.3 kA, t=200ms, steel).
Results of temperature measurement of the inner cylinder wall: trace 1 is sinchrosignal (pulse onset agrees with the beginning of the synchrosignal in the arc current oscillogram); trace2, trace 3, trace4, trace5, trace6 are temperature records at the probe locations (pointed by black circles)

Fig 2.10. Shot # 2 (I_{max}=11.3 kA, t=200ms, steel)
Picture of the cylinder region affected by the arc

2.3. Shot # 3

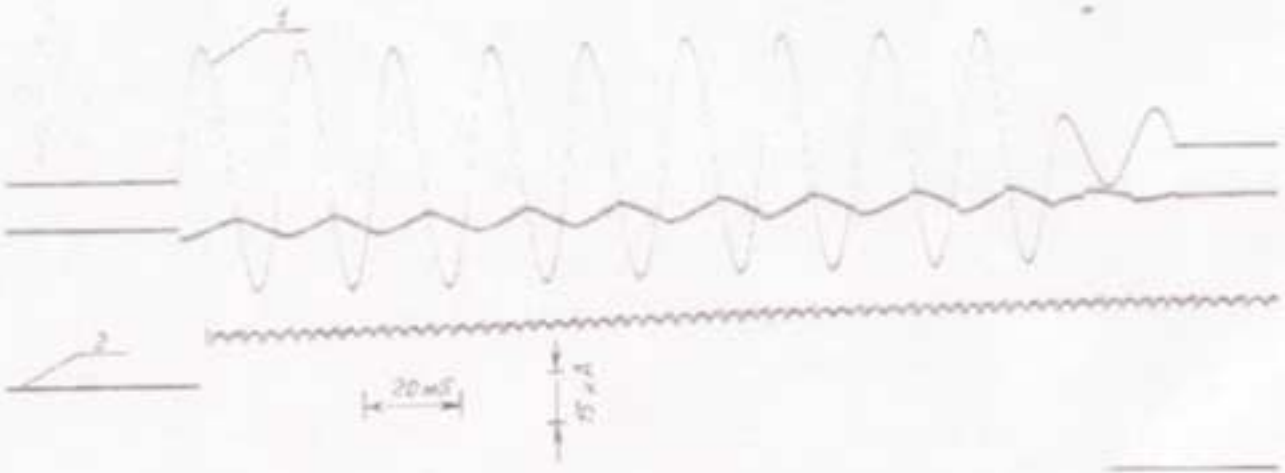

Fig.2.11. Shot # 3 (I_{max}=36.9 kA, t=200ms, steel).
Arc current oscillogram: 1 is arc current, 2 is sinchrosignal

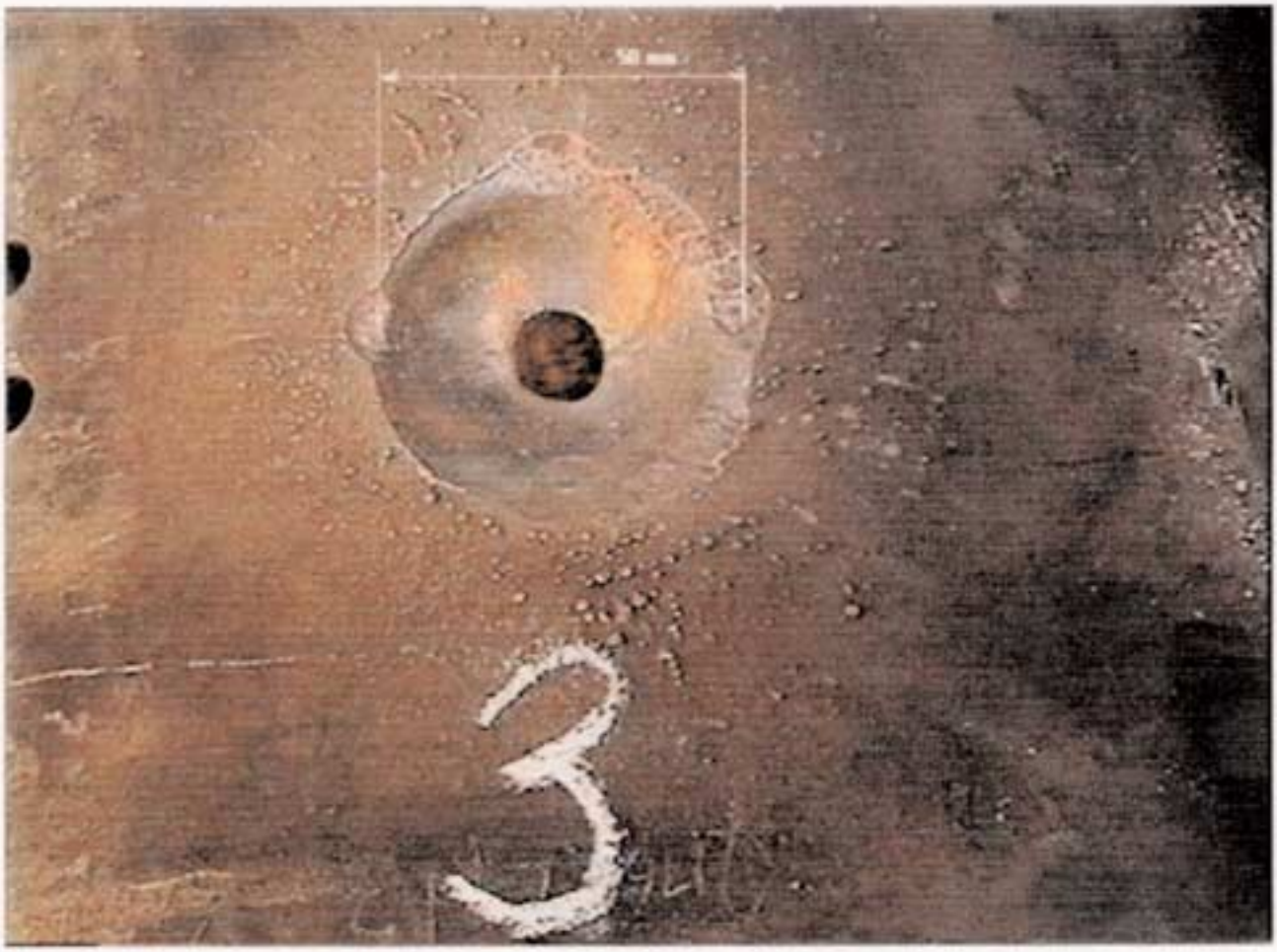

Fig.2.12. Shot # 3 (I_{max}=36.9 kA, t=200ms, steel).
Picture of the cylinder region affected by the arc.

2.4. Shot # 4

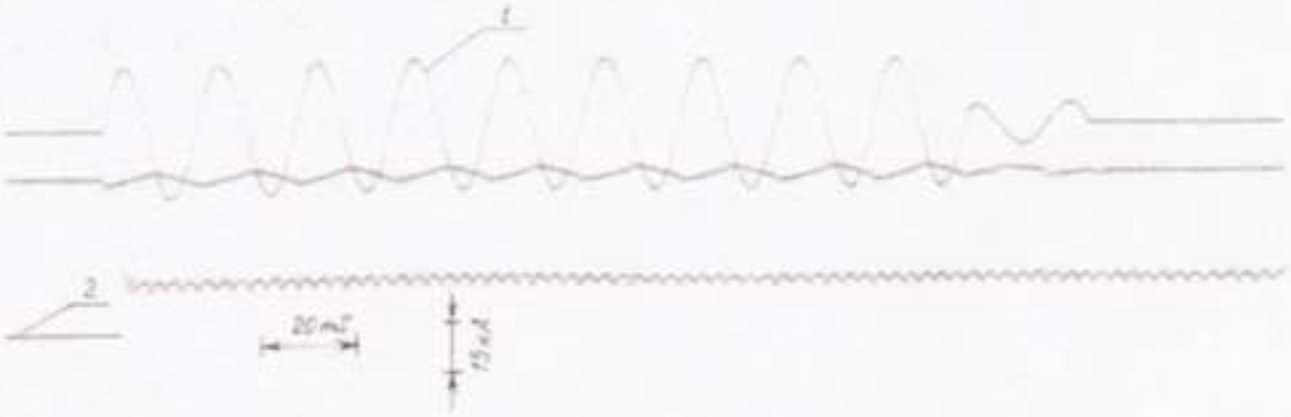

Fig.2.13. Shot # 4 (I_{max}=19.4 kA, t=200ms, aluminum alloy).
Arc current oscillogram: 1 is arc current, 2 is sinchrosignal

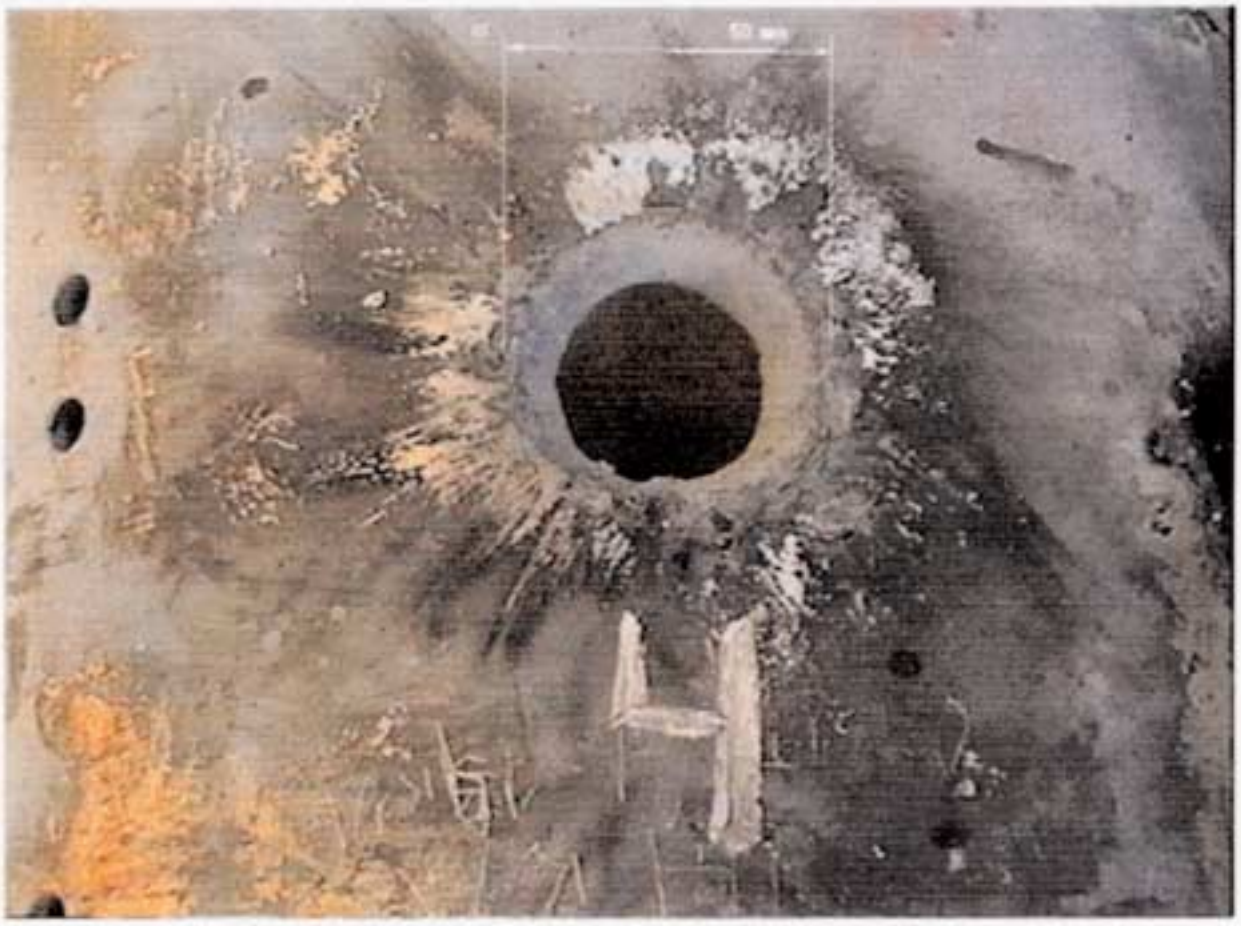

Ffig.2.14. Shot # 4 (I_{max}=19.4 kA, t=200ms, aluminum alloy).
Picture of the cylinder region affected by the arc.

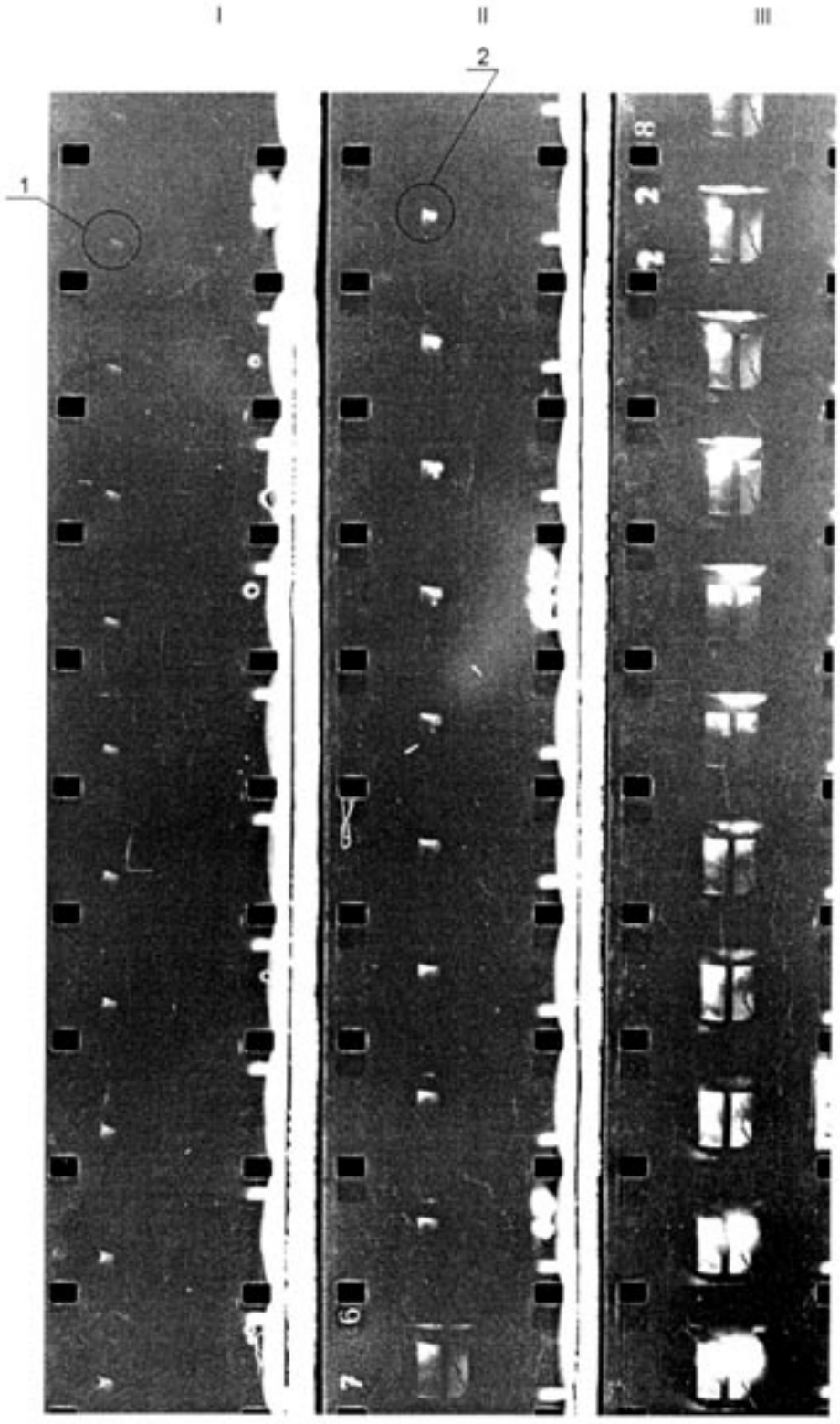

Fig.2.15. Shot # 4 (I_{max}=19.4 kA, t=200ms, aluminum alloy).

Motion picture record of the cylinder burning though process. Frame frequency is 2500 frames/s. The frame column I shows the beginning of the arc effect on the cylinder. Position 1 denotes the glow appeared at the time of the arc ignition. Frame columns II and III show the process of hole formation and growth in the process of arc effect. Glow appearance (denoted by 2) results from hole formation in the cylinder hole. Time interval from the beginning of arc glow to hole formation is 52±1 ms.

2.5. Shot # 5

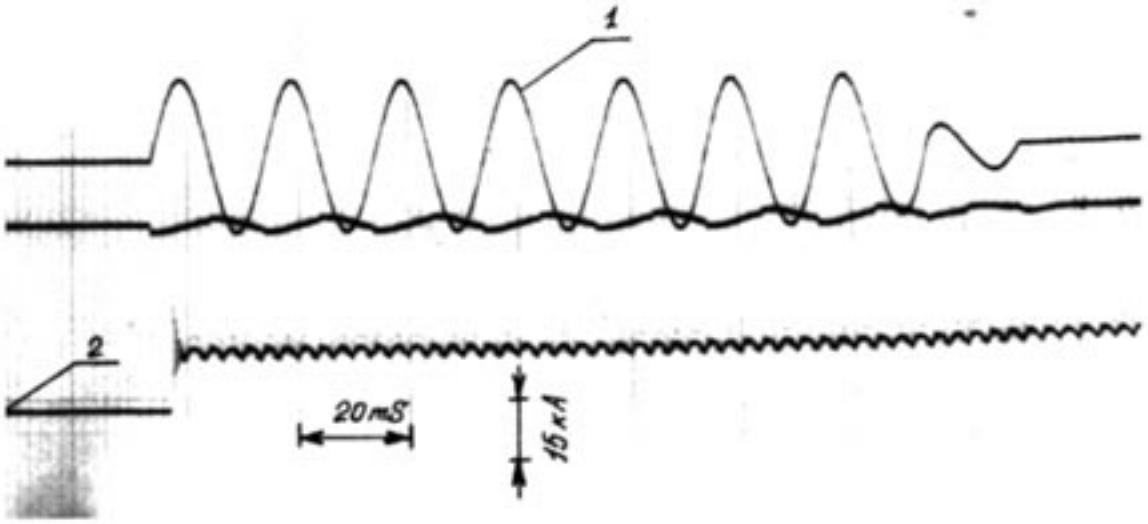

Fig. 2.16. Shot # 5 (I_{max}=19.4 kA, t=150ms, aluminum alloy).
Arc current oscillogram: 1 is arc current, 2 is sinchrosignal

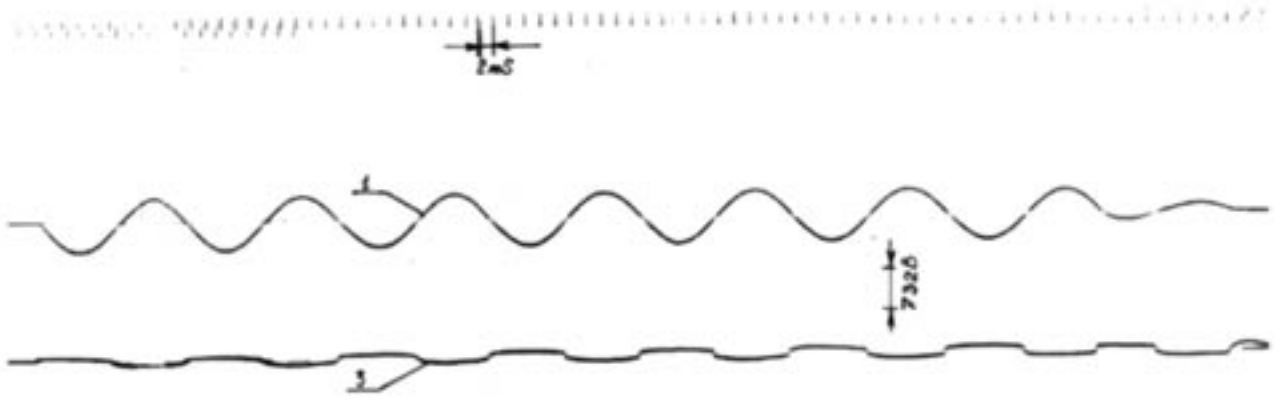

Fig. 2.17. Shot # 5 (I_{max}=19.4 kA, t=150ms, aluminum alloy).
Arc voltage oscillogram: 1 is arc current, 3 is arc voltage

Fig. 2.18. Shot # 5 (I_{max}=19.4 kA, t=150ms, aluminum alloy).
Picture of the cylinder region affected by the arc.

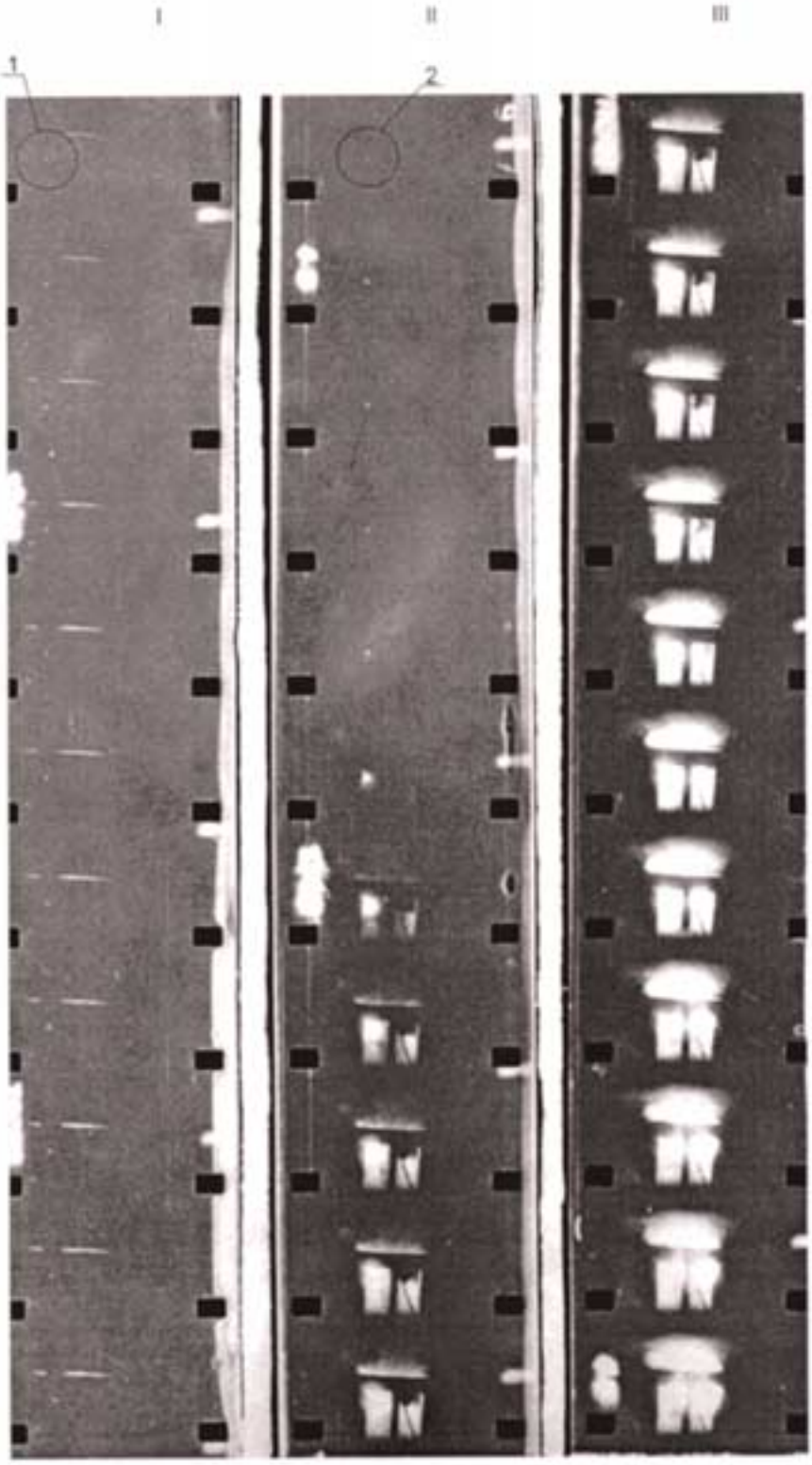

Fig.2.19. Shot # 5 (I_{max}=19.4 kA, t=150ms, aluminum alloy).

Motion picture record of the cylinder burning though process. Frame frequency is 2500 frames/s. The frame column I shows the beginning of the arc effect on the cylinder. Position 1 denotes the glow appeared at the time of the arc ignition. Frame columns II and III show the process of hole formation and growth in the process of arc effect. Glow appearance (denoted by 2) results from hole formation in the cylinder hole. Time interval from the beginning of arc glow to hole formation is 79 ± 1 ms.

2.6. Shot # 6

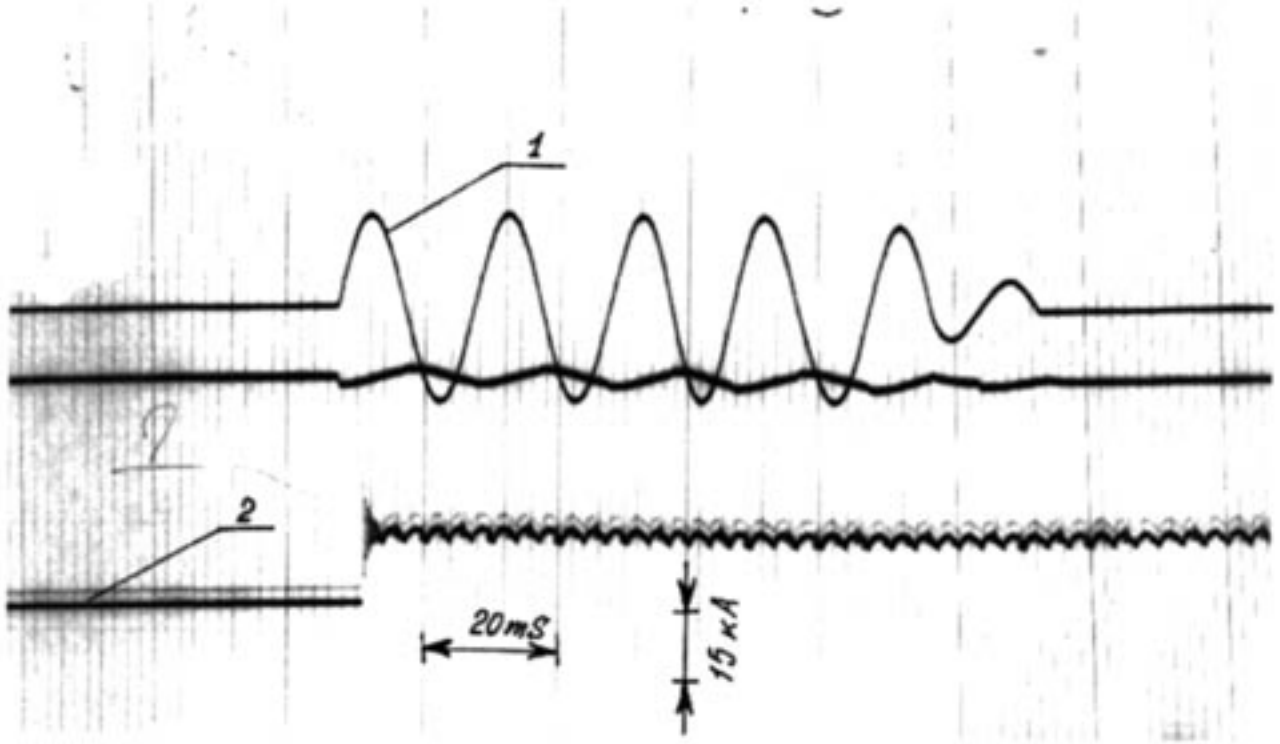

Fig.2.20. Shot # 6 (I_{max}=19.4 kA, t=100ms, aluminum alloy).
Arc current oscillogram: 1 is arc current, 2 is sinchrosignal

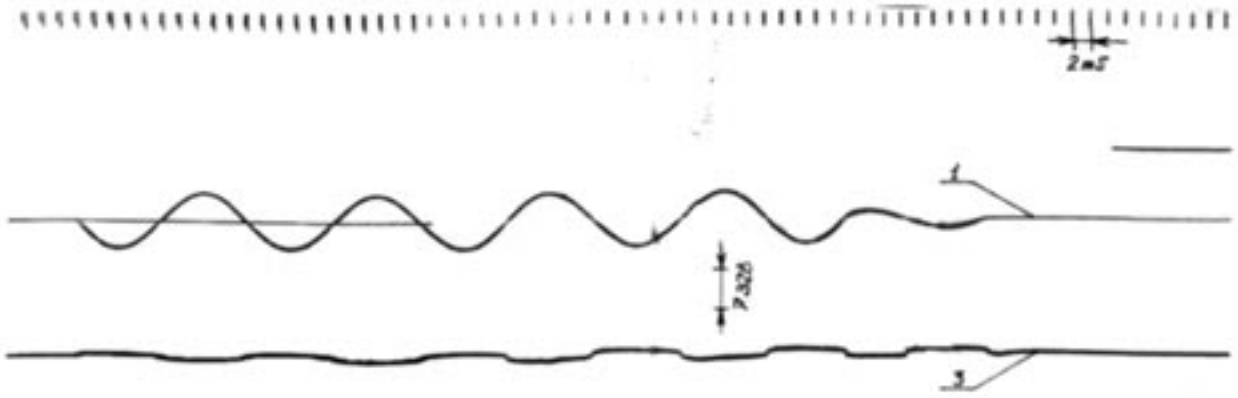

Fig.2.21. Shot # 6 (I_{max}=19.4 kA, t=100ms, aluminum alloy).
Arc voltage oscillogram: 1 is arc current, 3 is arc voltage

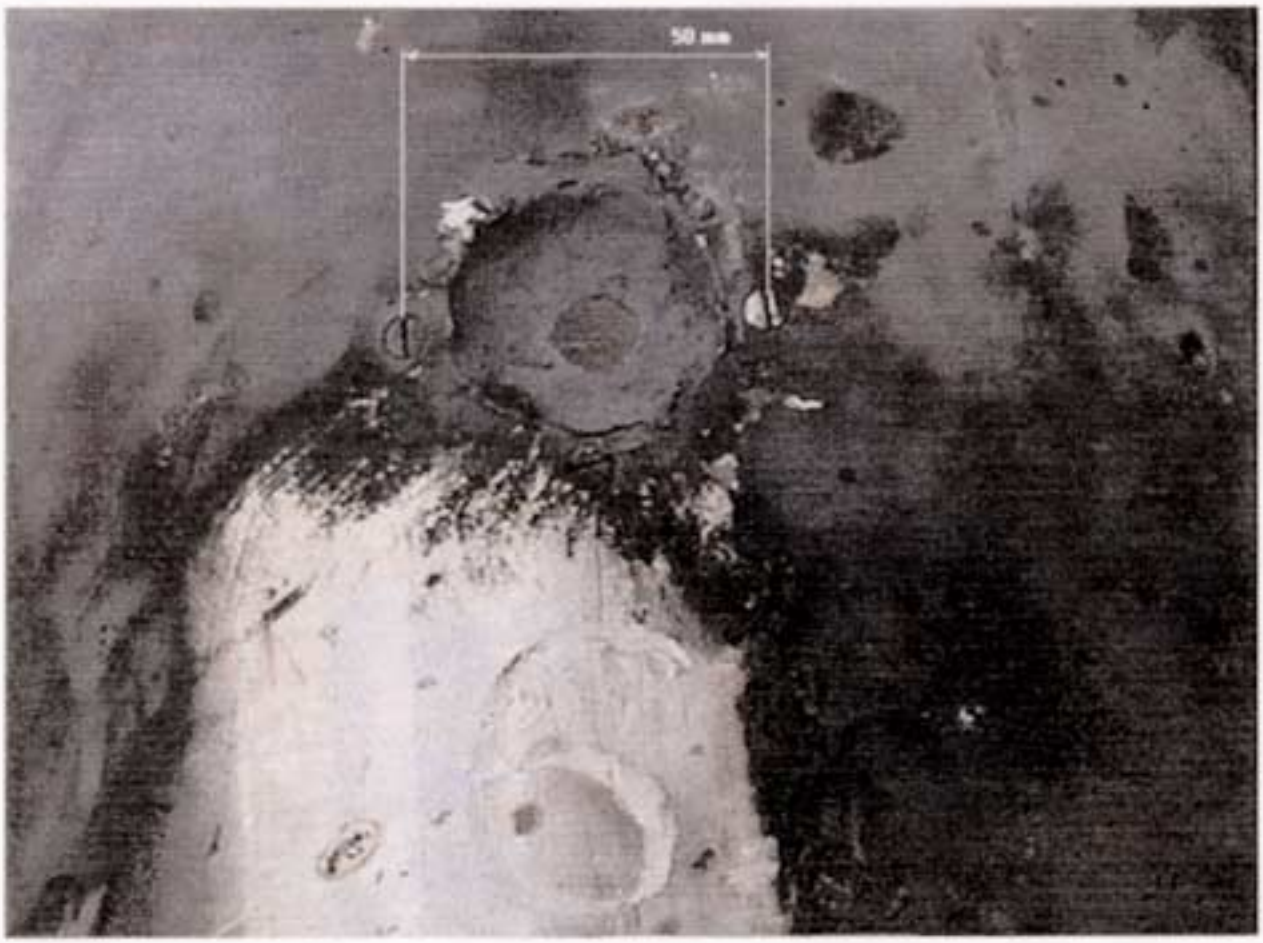

Fig.2.22. Shot # 6 (I_{max}=19.4 kA, t=100ms, aluminum alloy).
Picture of the cylinder region affected by the arc.

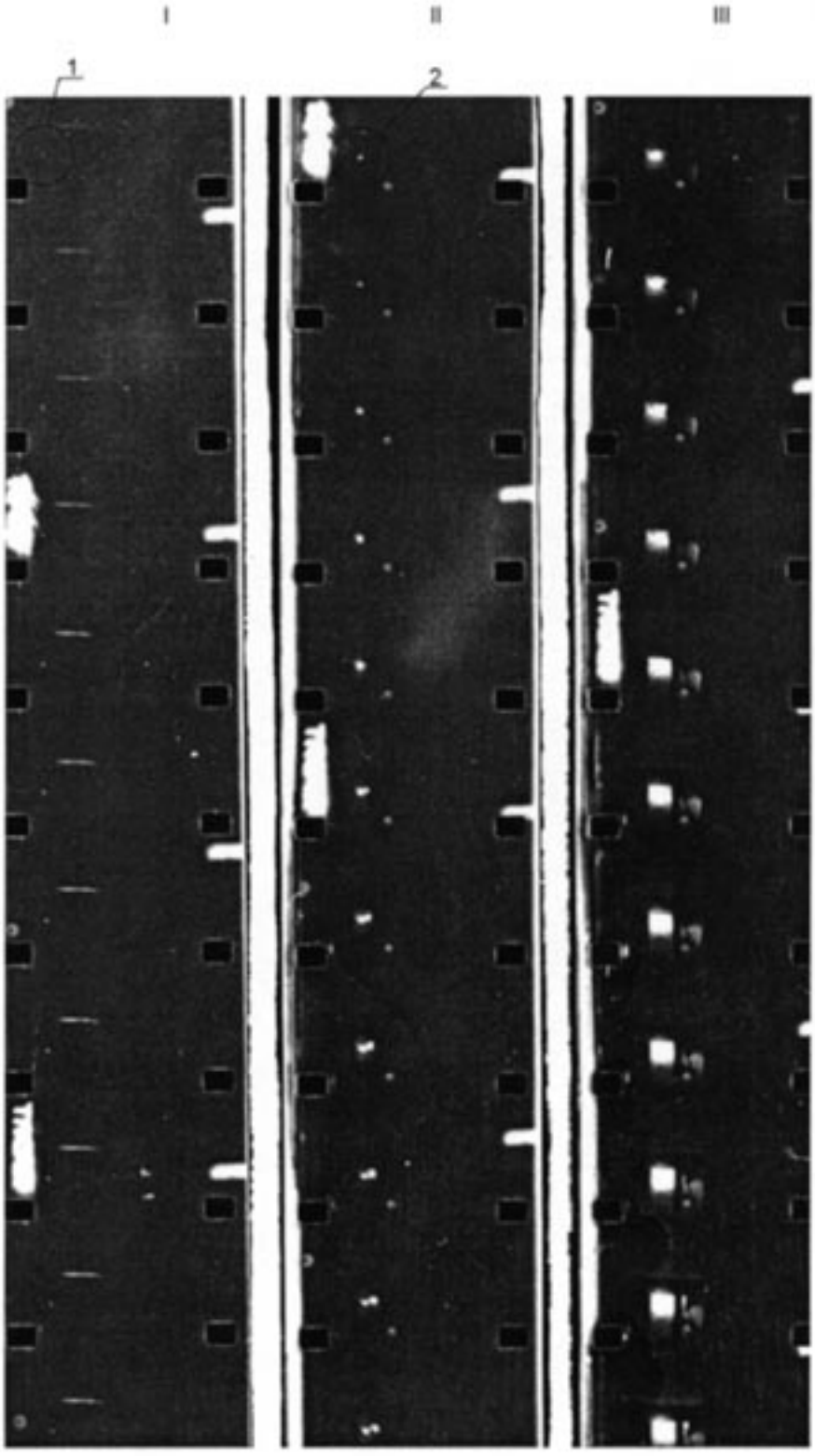

Fig.2.23. Shot # 6 ($(I_{max}$=19.4 kA, t=100ms, aluminum alloy).

Motion picture record of the cylinder burning though process. Frame frequency is 2500 frames/s. The frame column I shows the beginning of the arc effect on the cylinder. Position 1 denotes the glow appeared at the time of the arc ignition. Frame columns II and III show the process of hole formation and growth in the process of arc effect. Glow appearance (denoted by 2) results from hole formation in the cylinder hole. Time interval from the beginning of arc glow to hole formation is 89 ± 1 ms.

2.7. Shot # 7

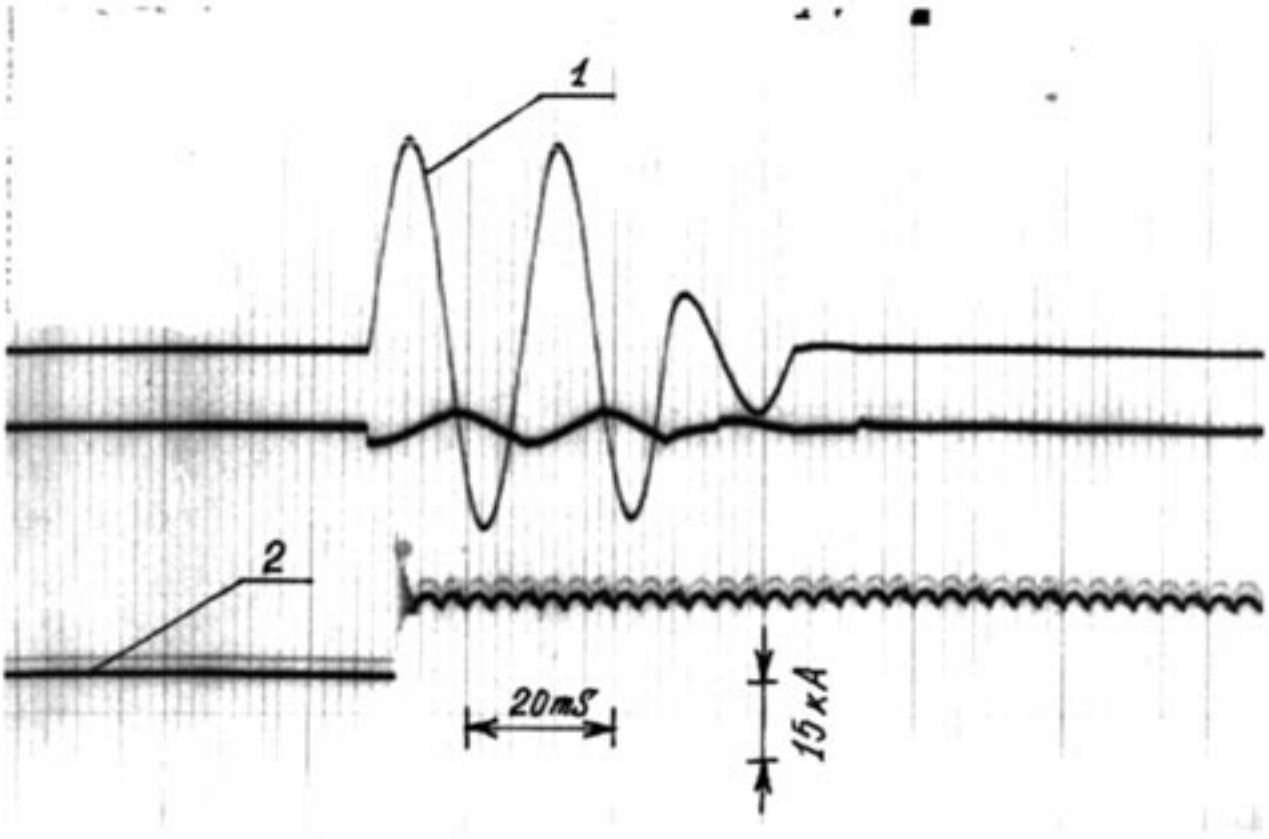

Fig.2.24. Shot # 7 (I_{max}=36,9 kA, t=50ms, aluminum alloy).
Arc current oscillogram: 1 is arc current, 2 is sinchrosignal

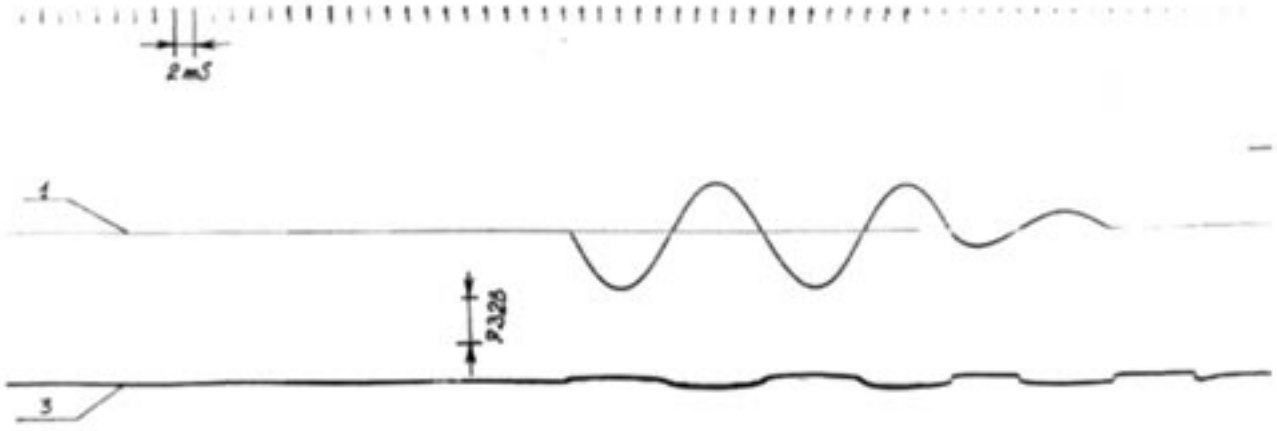

Fig.2.25. Shot # 7 (I_{max}=36,9 kA, t=50ms, aluminum alloy).
Arc voltage oscillogram: 1 is arc current, 3 is arc voltage

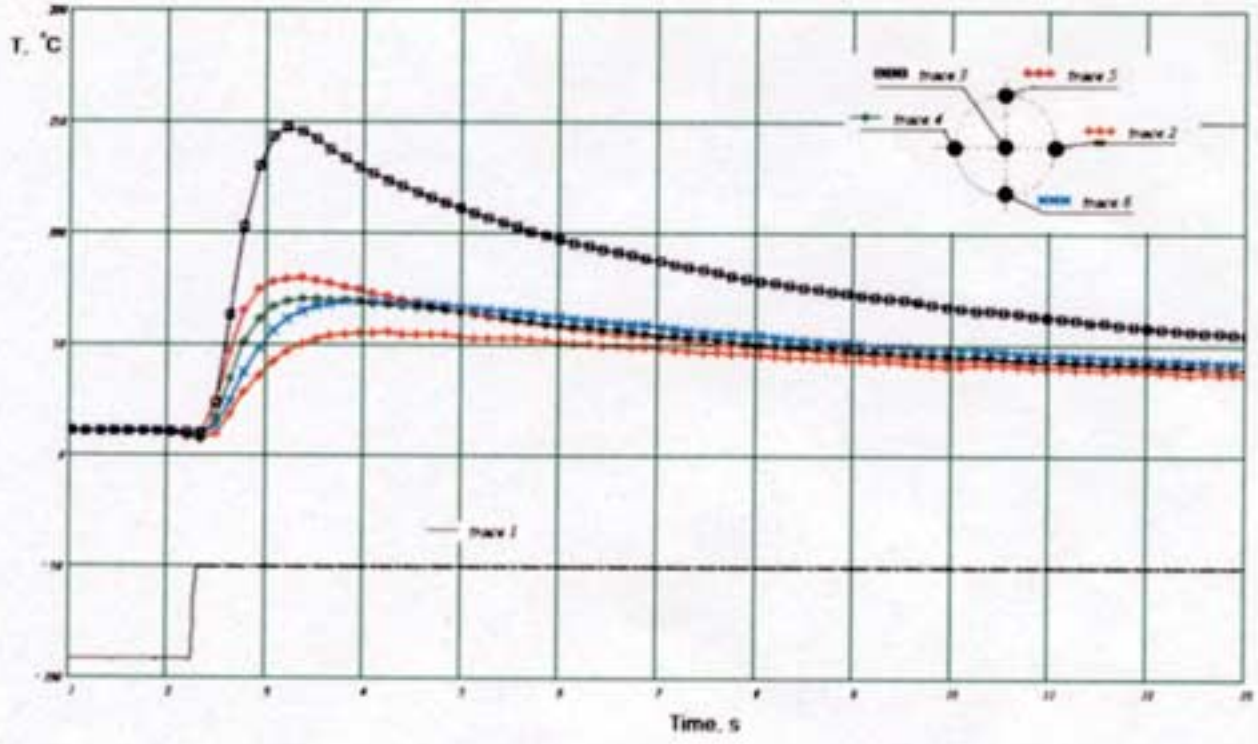

Fig.2.26. Shot # 7 (I_{max}=36,9 kA, t=50ms, aluminum alloy).

Results of temperature measurement of the inner cylinder wall: trace 1 is sinchrosignal (pulse onset agrees with the beginning of the synchrosignal in the arc current oscillogram); trace2, trace 3, trace4, trace5, trace6 are temperature records at the probe locations (pointed by black circles)

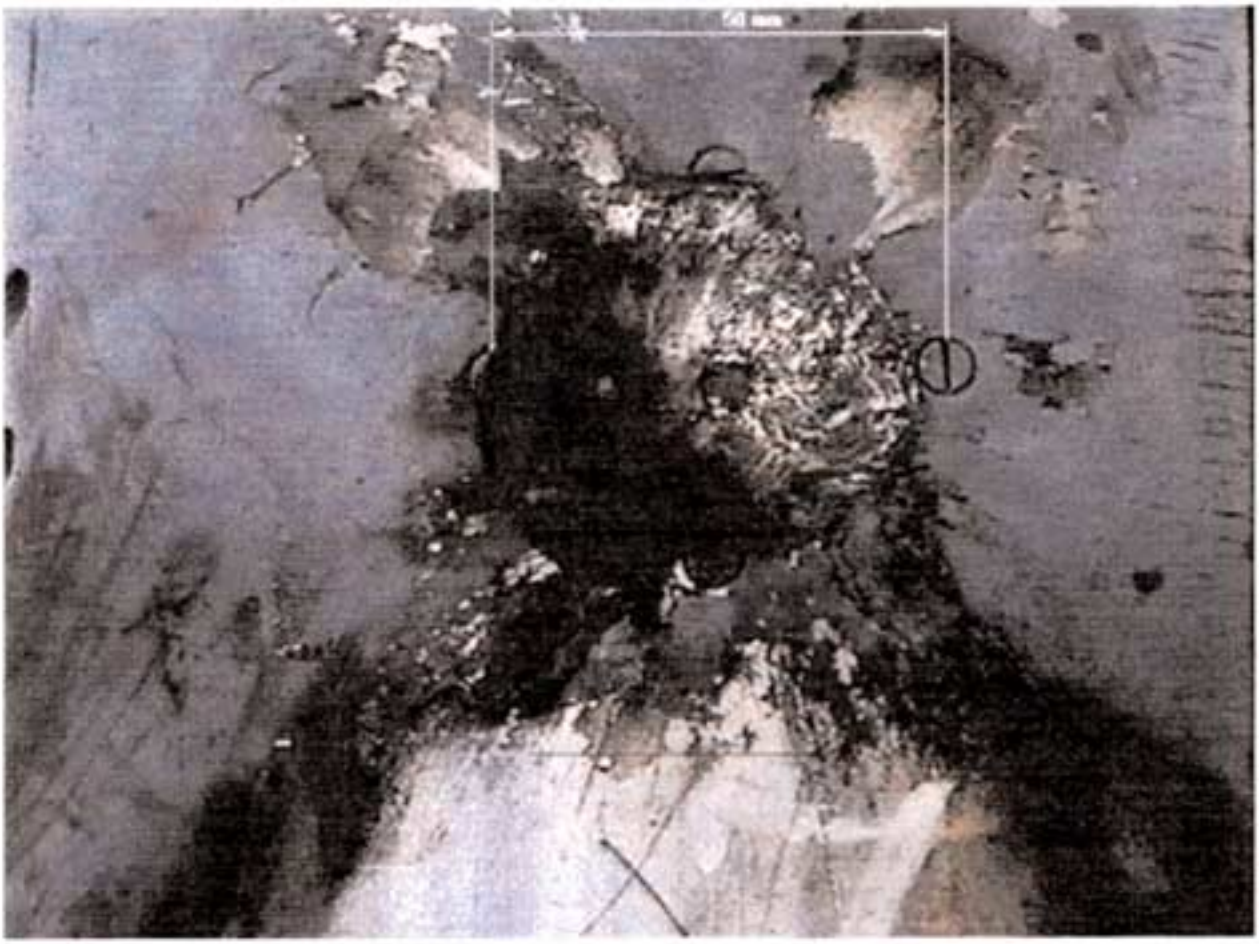

Fig. 2.27. Shot # 7 ($I_{r.m.s.}$=36.9 kA, t=50ms, aluminum alloy).
Picture of the cylinder region affected by the arc.

2.8. Shot # 8

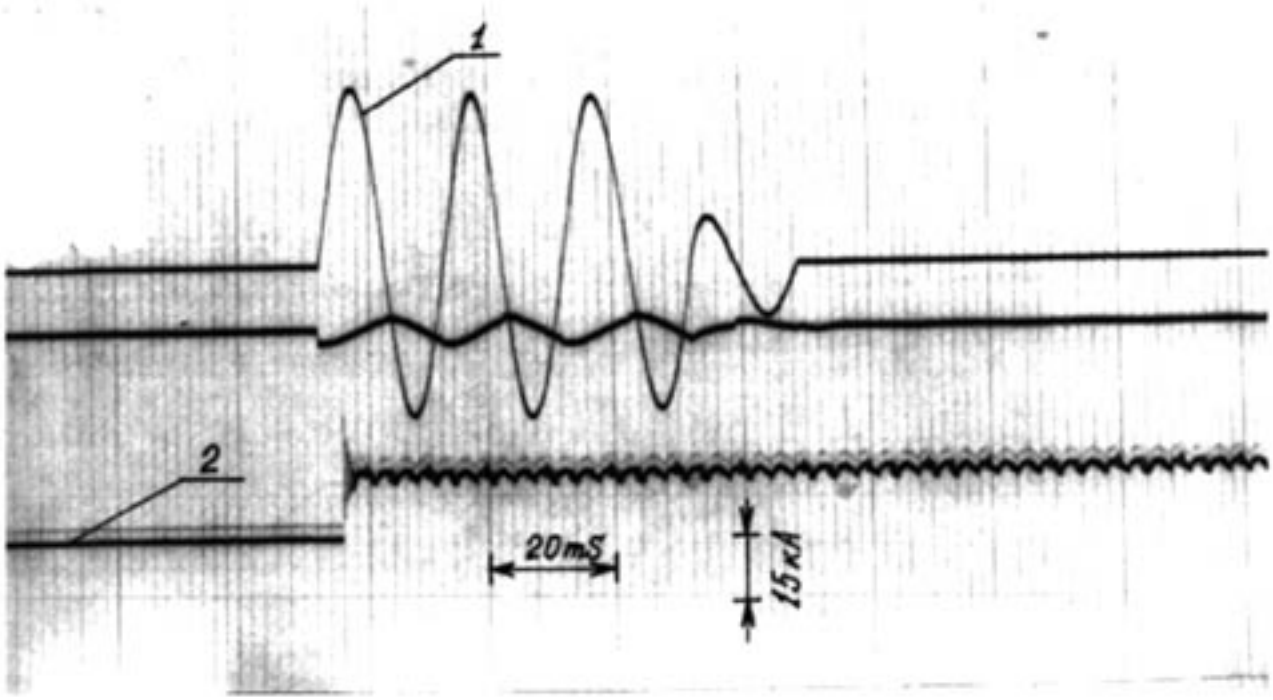

Fig.2.28. Shot # 8 (I_{max}=36,9 kA, t=70ms, aluminum alloy).
Arc current oscillogram: 1 is arc current, 2 is sinchrosignal

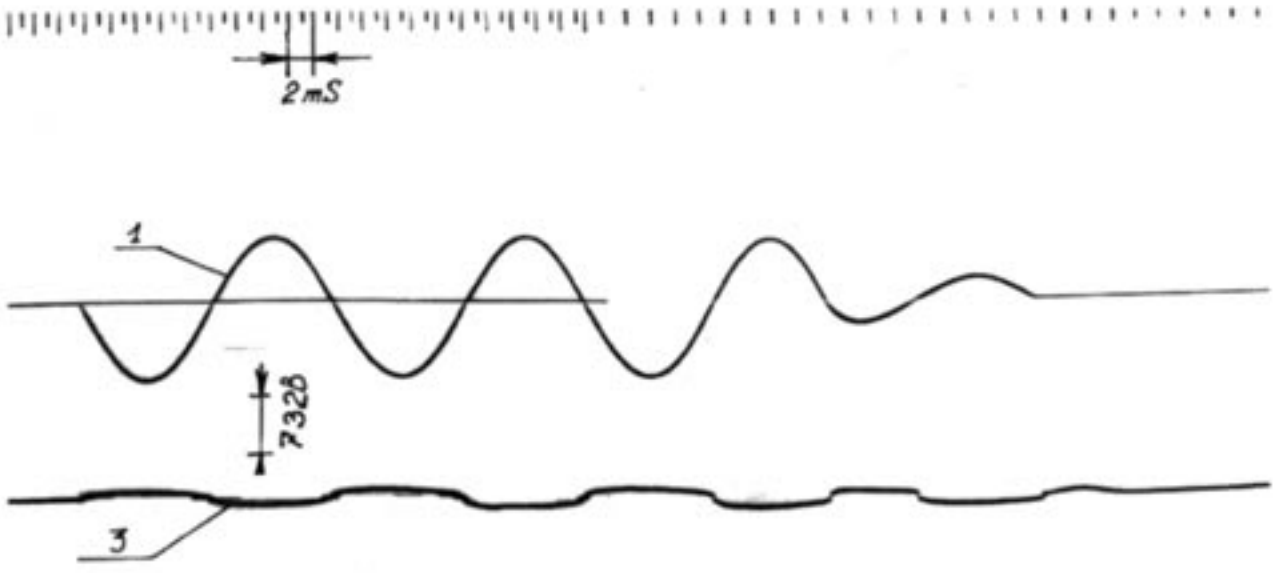

Fig. 2.29. Shot # 8 (I_{max}=36,9 kA, t=70ms, aluminum alloy).
Arc voltage oscillogram: 1 is arc current, 3 is arc voltage

Fig. 2.30. Shot # 8 (I_{max}=36,9 kA, t=70ms, aluminum alloy).
Picture of the cylinder region affected by the arc.

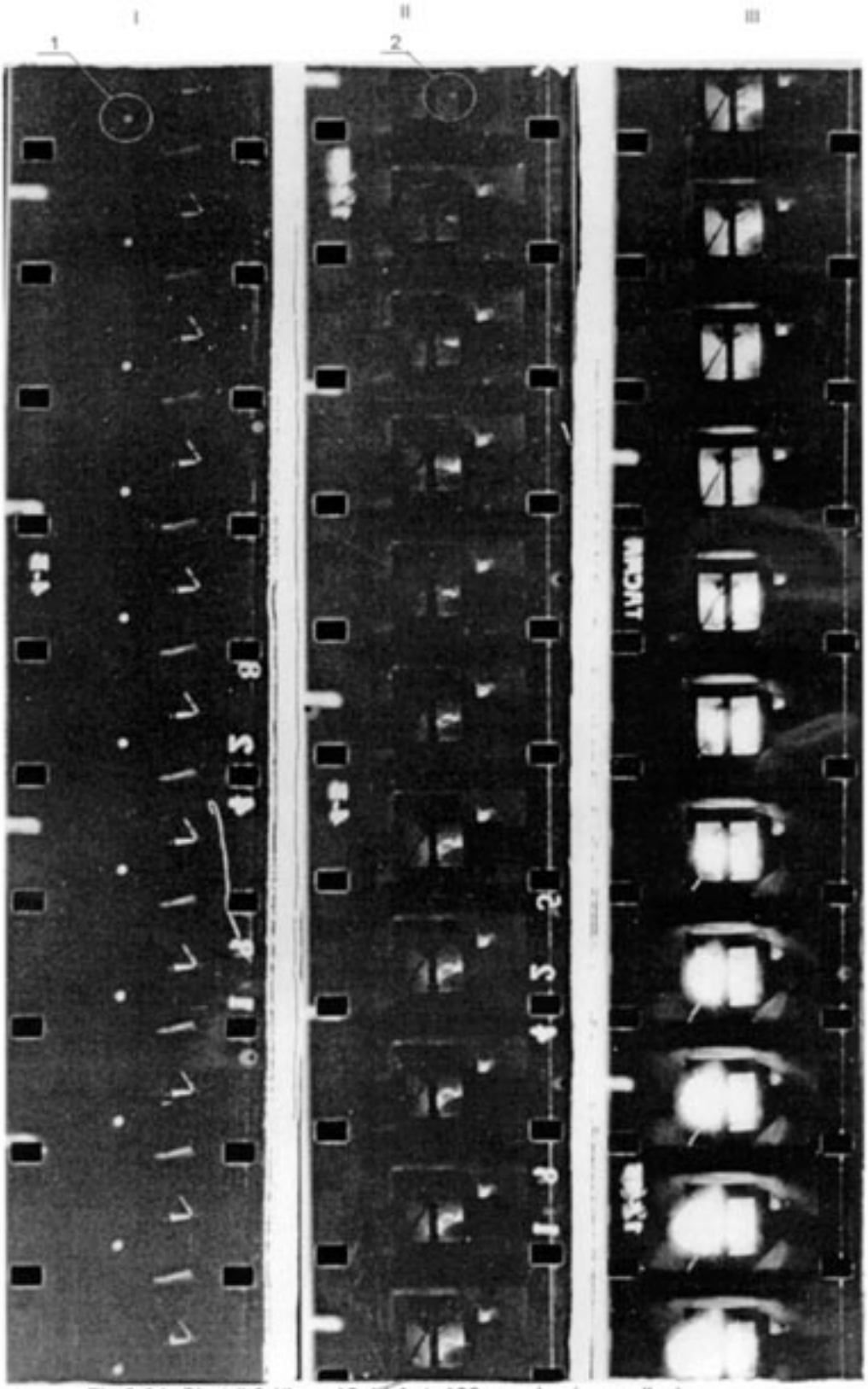

Fig.2.31. Shot # 8 (I_{max}=19.4 kA, t=100ms, aluminum alloy).

Motion picture record of the cylinder burning though process. Frame frequency is 2500 frames/s. The frame column I shows the beginning of the arc effect on the cylinder. Position 1 denotes the glow appeared at the time of the arc ignition. Frame columns II and III show the process of hole formation and growth in the process of arc effect. Glow appearance (denoted by 2) results from hole formation in the cylinder hole. Time interval from the beginning of arc glow to hole formation is 48 ± 1 ms.

2.9. Shot # 9

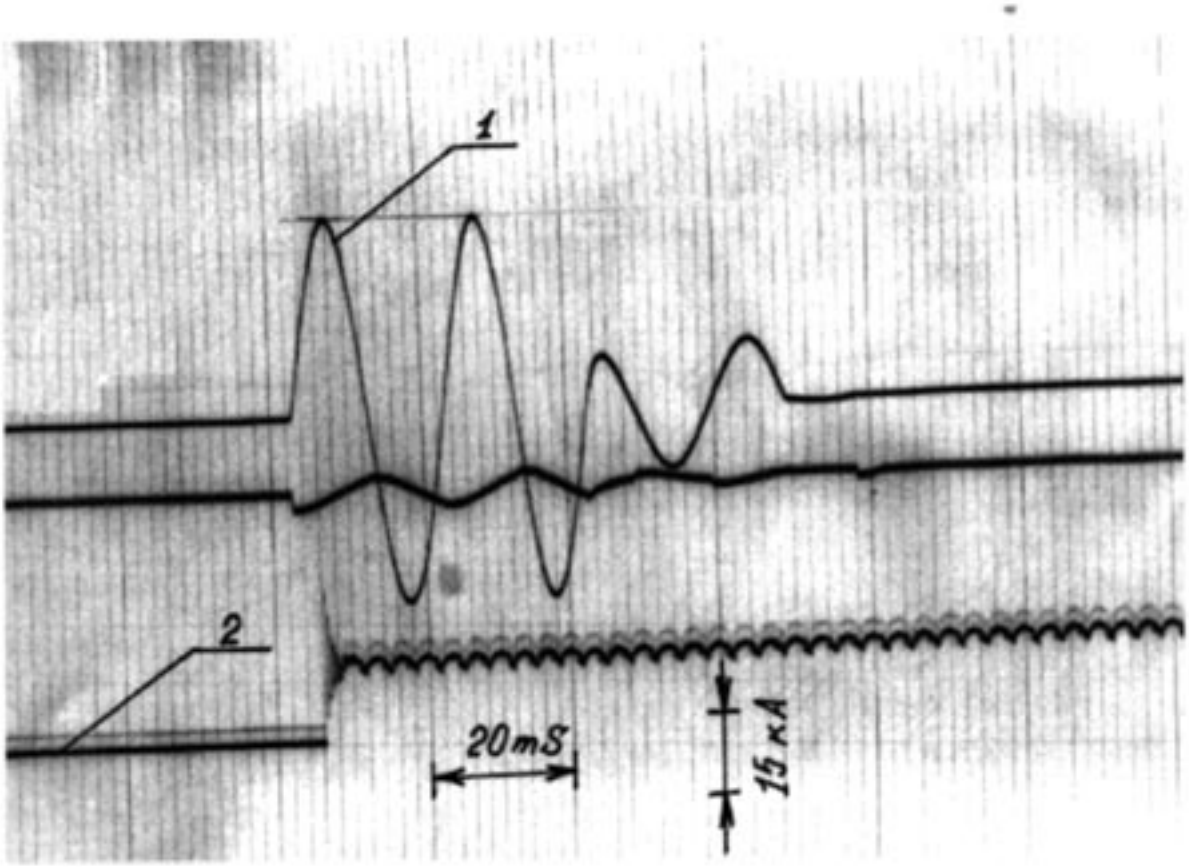

Fig.2.32. Shot # 9 (I_{max}=36,9 kA, t=60ms, aluminum alloy).
Arc current oscillogram: 1 is arc current, 2 is sinchrosignal

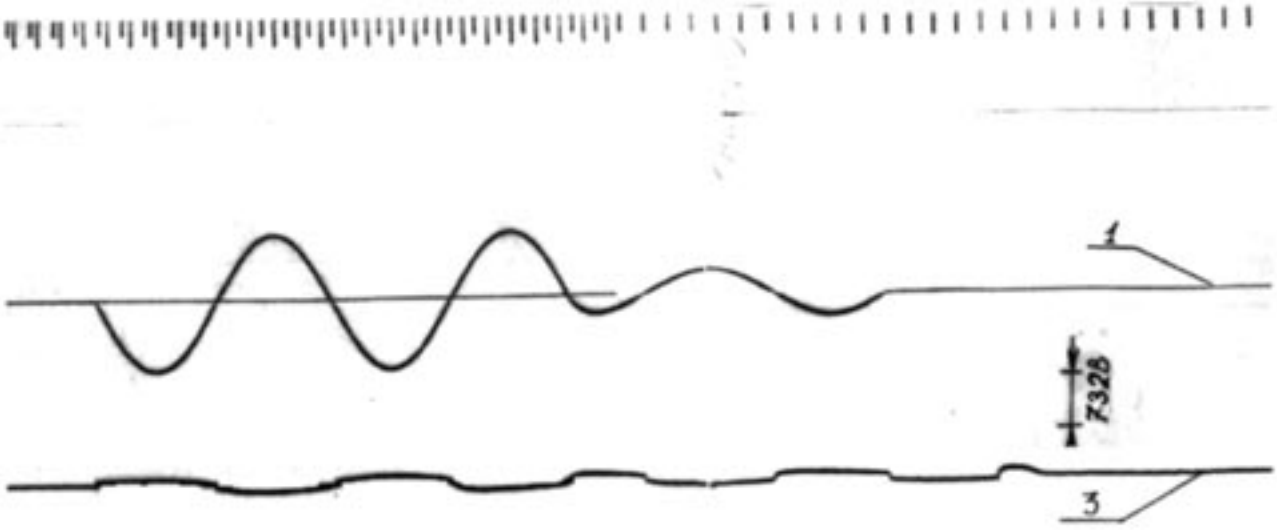

Fig. 2.33. Shot # 9 (I_{max}=36,9 kA, t=60ms, aluminum alloy).
Arc voltage oscillogram: 1 is arc current, 3 is arc voltage

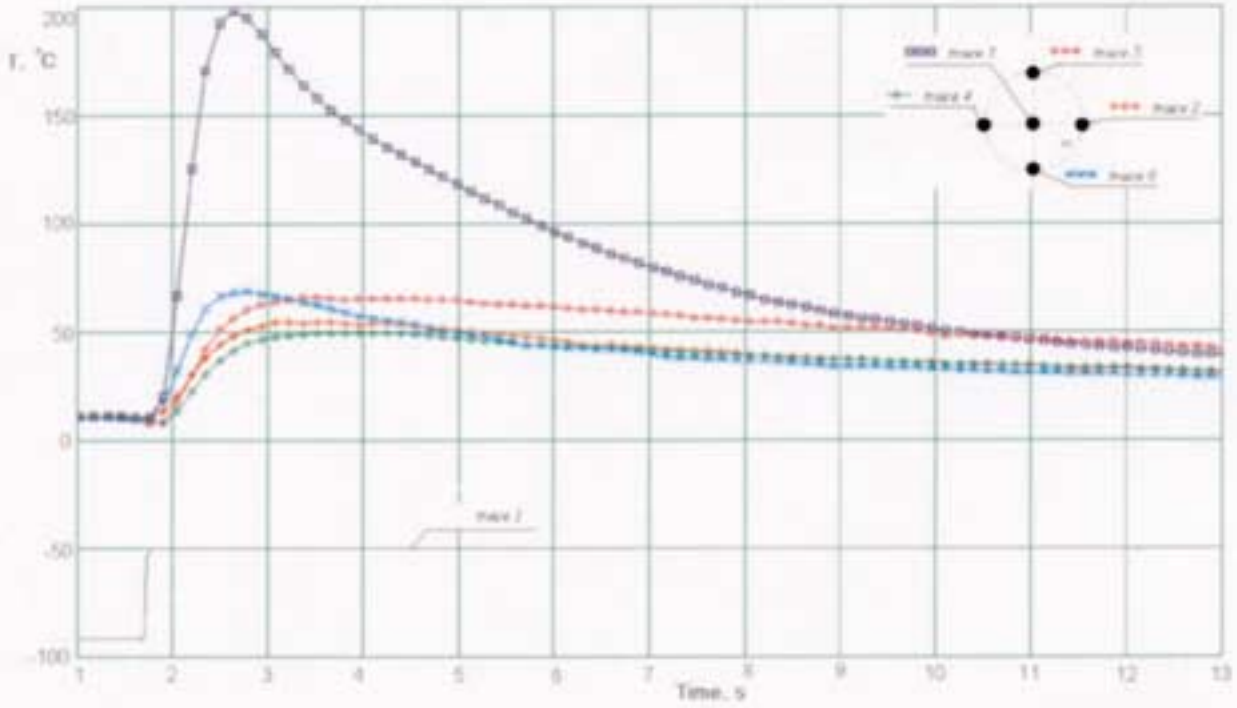

Fig. 2.34. Shot # 9 (I_{max}=36,9 kA, t=60ms, aluminum alloy).

Results of temperature measurement of the inner cylinder wall: trace 1 is sinchrosignal (pulse onset agrees with the beginning of the synchrosignal in the arc current oscillogram); trace2, trace 3, trace4, trace5, trace6 are temperature records at the probe locations (pointed by black circles)

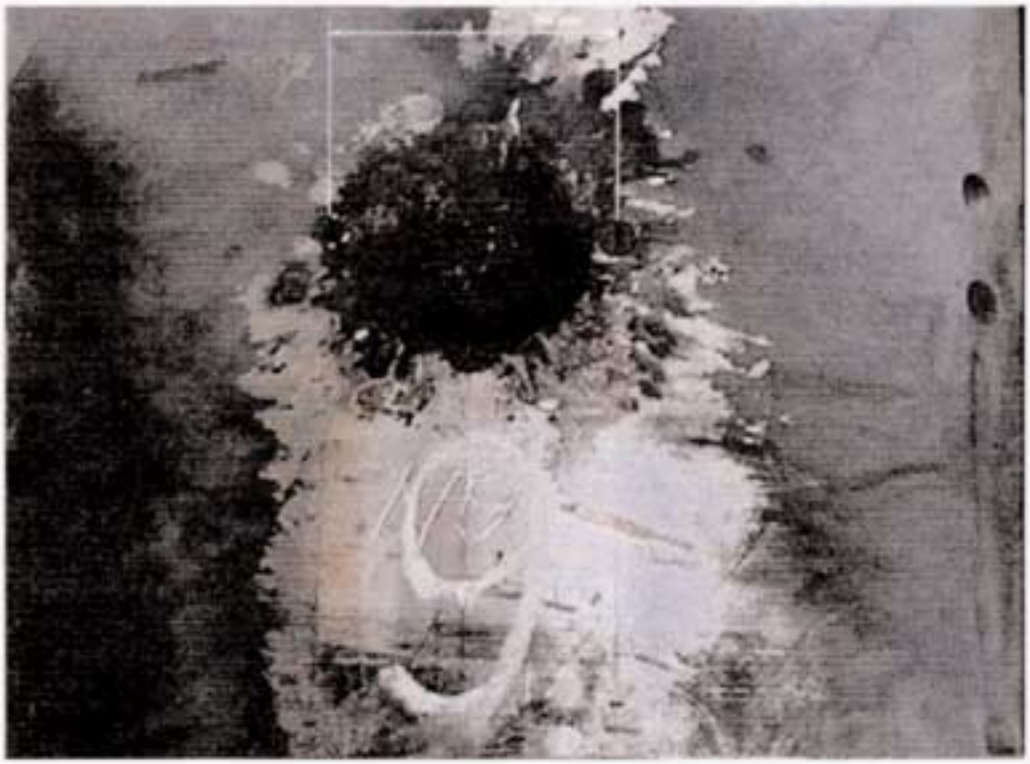

Fig. 2.35. Shot # 9 (I_{max}=36,9 kA, t=60ms, aluminum alloy).

Picture of the cylinder region affected by the arc.

2.10. Shot # 10

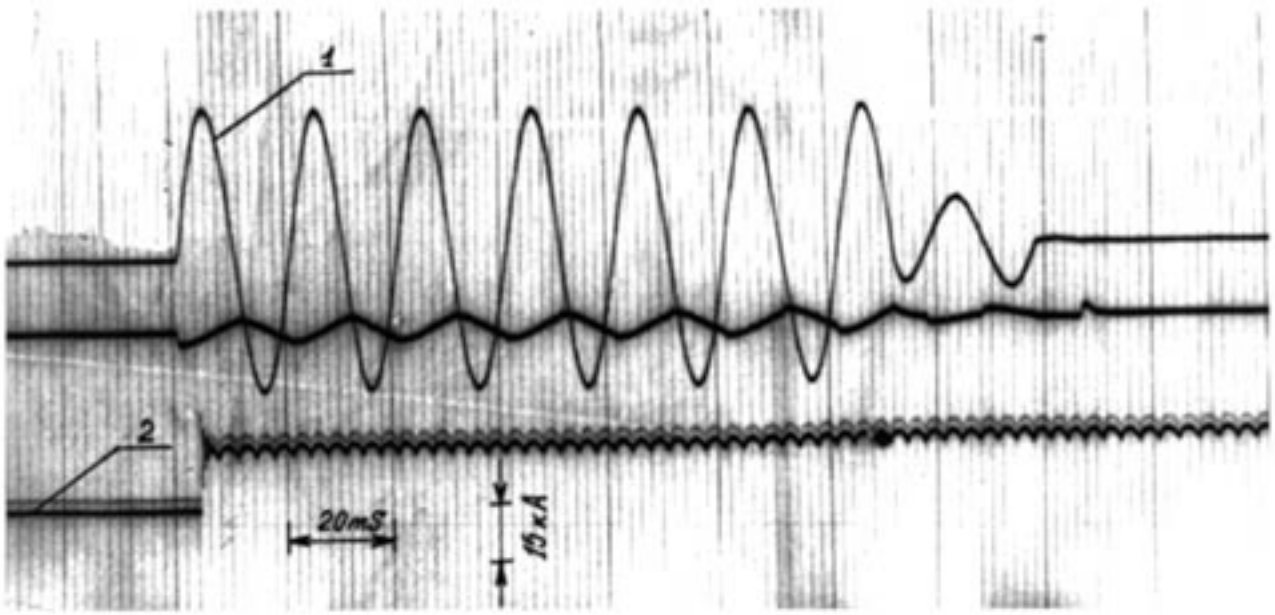

Fig. 2.36. Shot # 10 (I_{max}=36,9 kA, t=150ms, ~~aluminum alloy~~ steel).
Arc current oscillogram: 1 is arc current, 2 is sinchrosignal

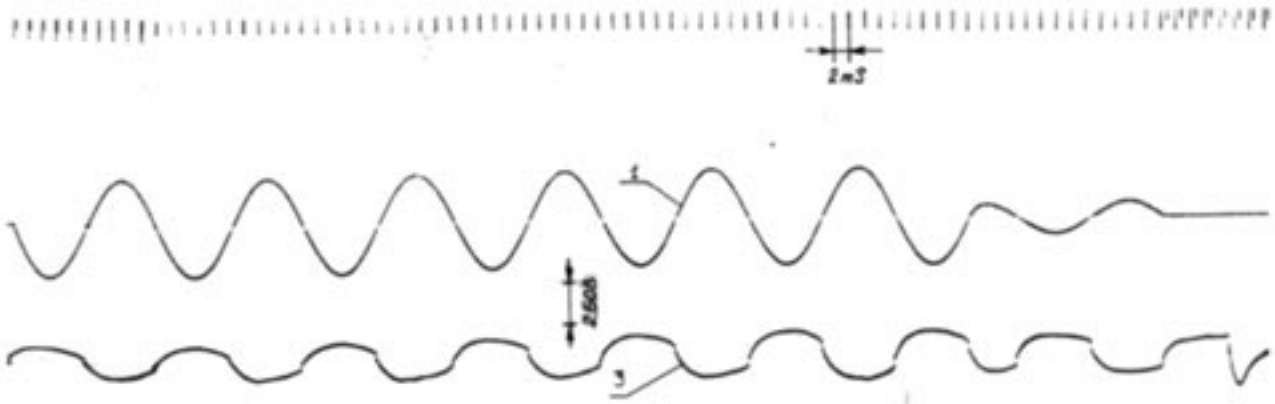

Fig. 2.37. Shot # 10 (I_{max}=36,9 kA, t=150ms, steel)).
Arc voltage oscillogram: 1 is arc current, 3 is arc voltage

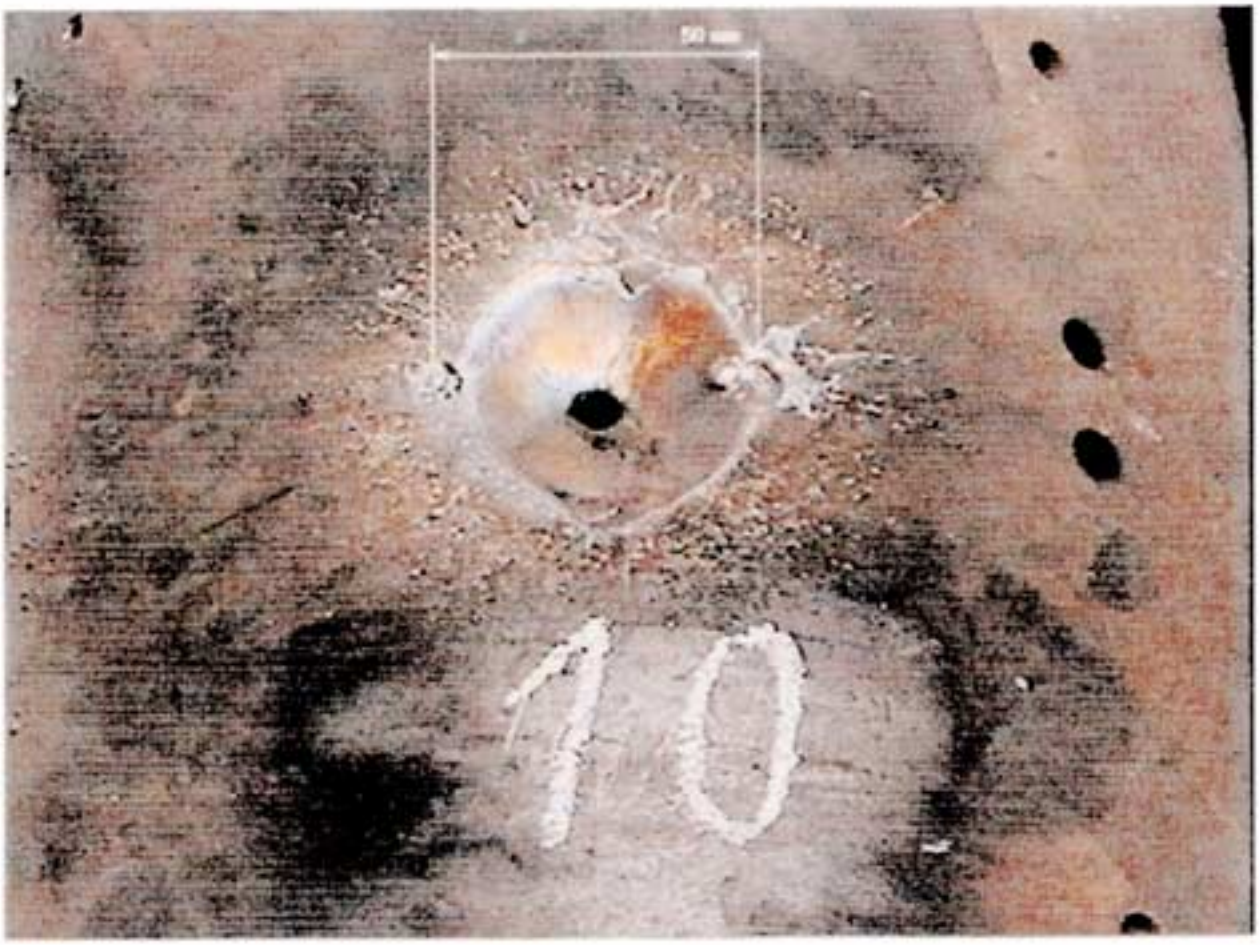

Fig. 2.38. Shot # 10 (I_{max}=36,9 kA, t=150ms, steel)).
Picture of the cylinder region affected by the arc.

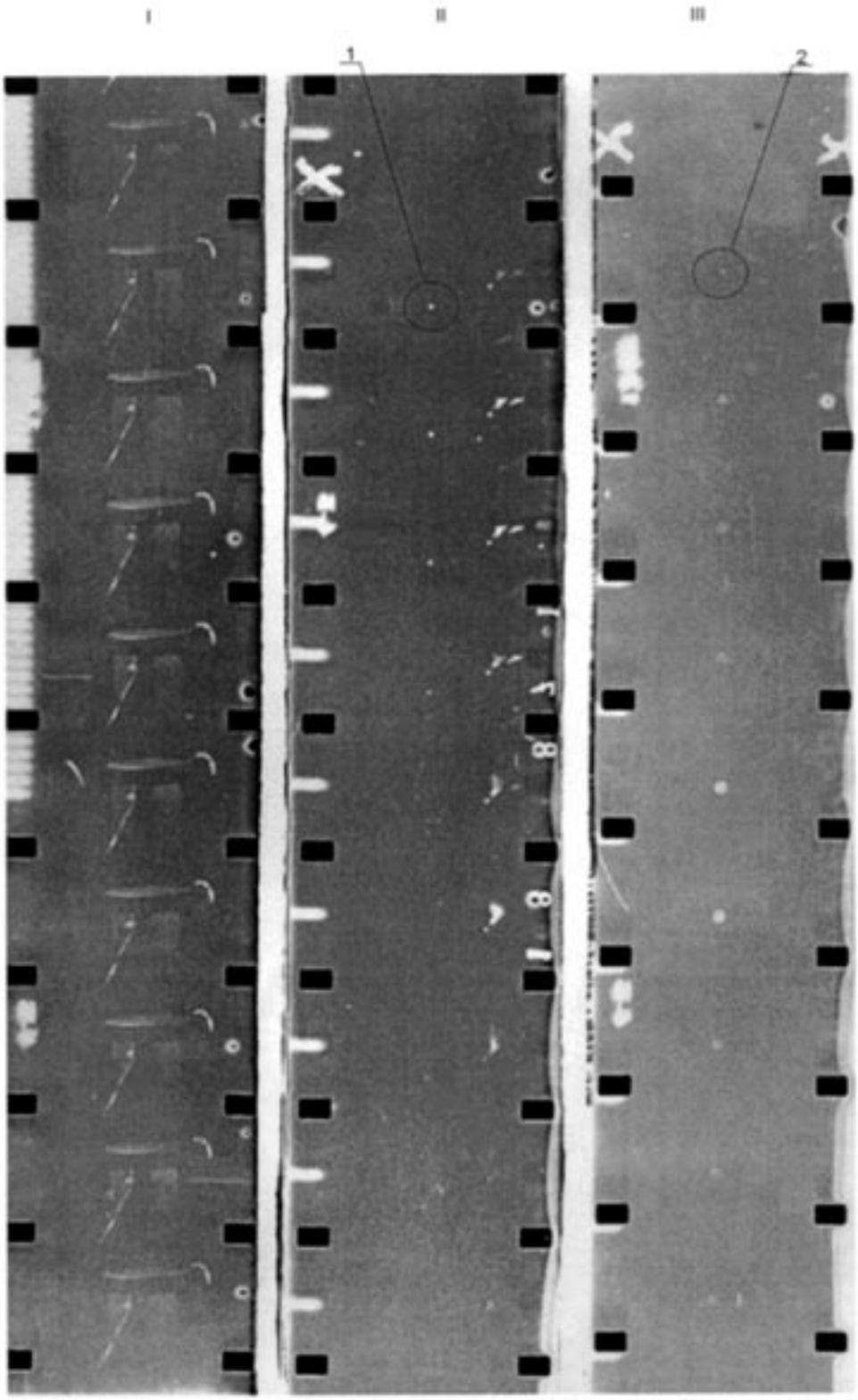

Fig. 2.39. Shot # 10 (I_{ma}=36.9kA, t =150 ms, steel)).

Motion picture record of the cylinder burning though process. Frame frequency is 1000 frames/s. The frame column I shows the cylinder before shot. The frame column II shows the beginning of the arc effect on the cylinder. Position 1 denotes the glow appeared at the time of the arc ignition. Frame column III show the process of hole formation and growth in the process of arc effect. Glow appearance (denoted by 2) results from hole formation in the cylinder hole. Time interval from the beginning of arc glow to hole formation is 126 ± 1 ms.

2.11. Shot # 11

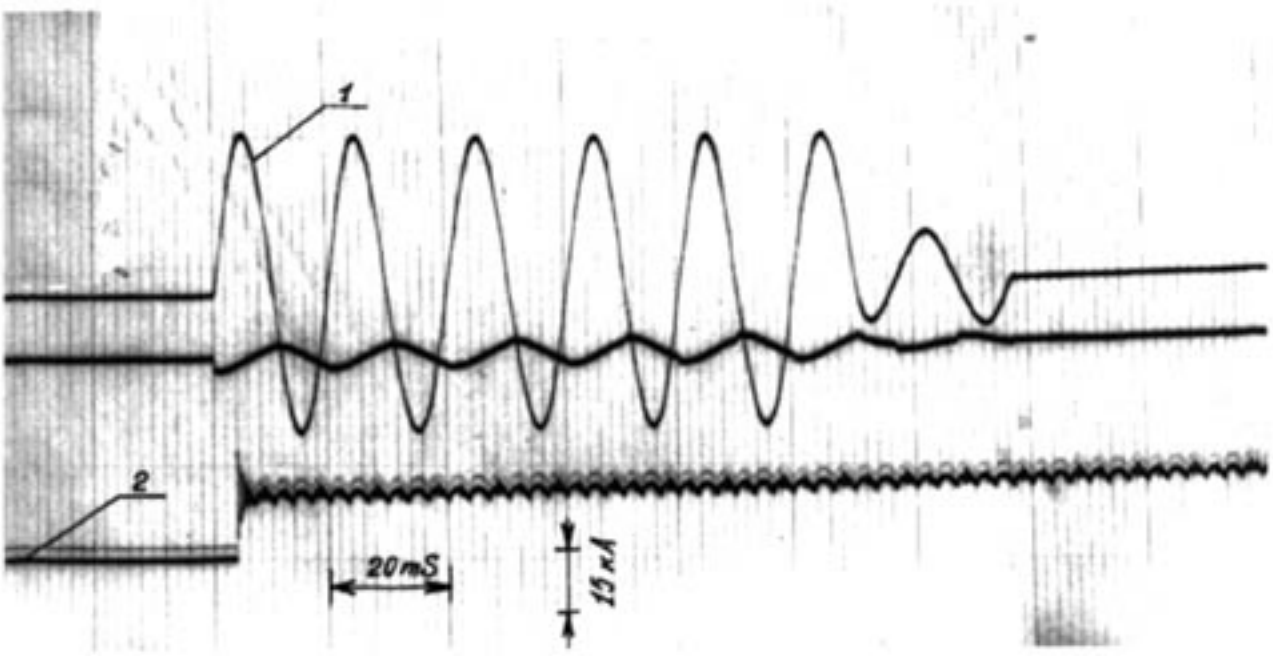

Fig. 2.40. Shot # 11 (I_{max}=36,9 kA, t=130ms, steel).
Arc current oscillogram: 1 is arc current, 2 is sinchrosignal

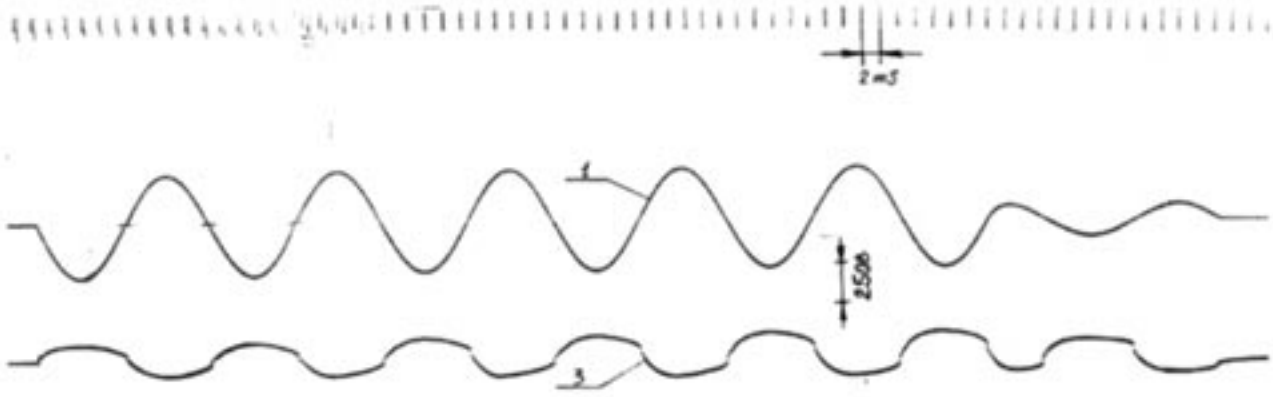

Fig. 2.41. Shot # 10 (I_{max}=36,9 kA, t=150ms, steel).
Arc voltage oscillogram: 1 is arc current, 3 is arc voltage

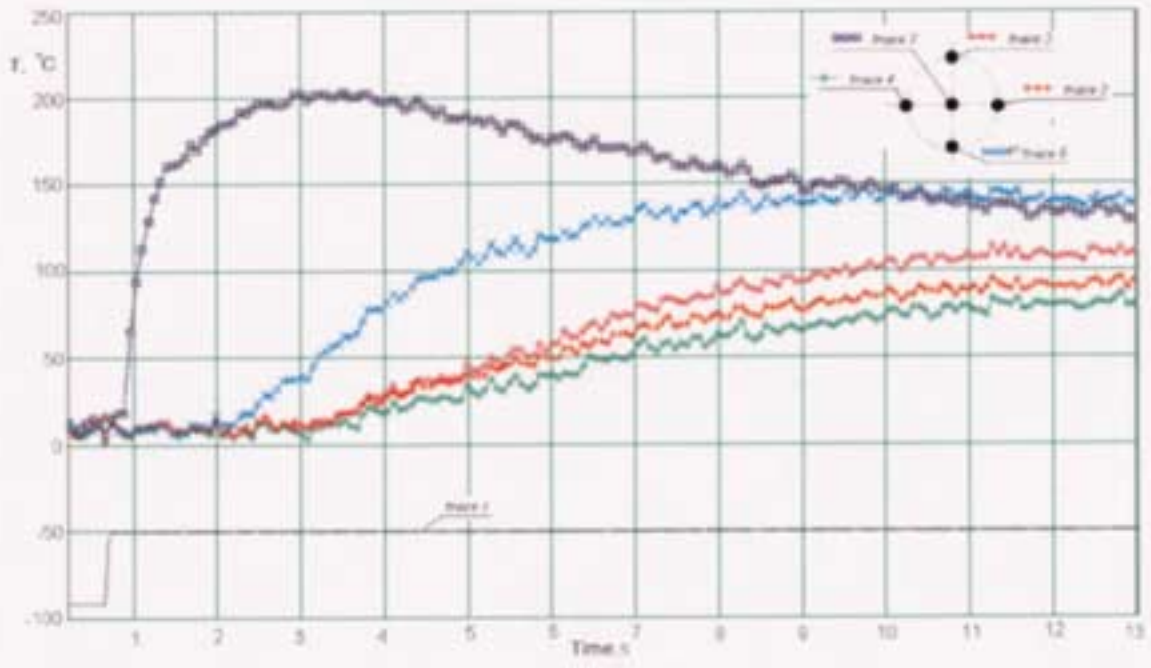

Fig. 2.42. Shot # 11 (I_{max}=36,9 kA, t=130ms, steel).

Results of temperature measurement of the inner cylinder wall: trace 1 is sinchrosignal (pulse onset agrees with the beginning of the synchrosignal in the arc current oscillogram); trace2, trace 3, trace4, trace5, trace6 are temperature records at the probe locations (pointed by black circles)

Fig. 2.43. Shot # 11 (I_{max}=36,9 kA, t=130ms, steel).

Picture of the cylinder region affected by the arc.

2.12. Shot # 12

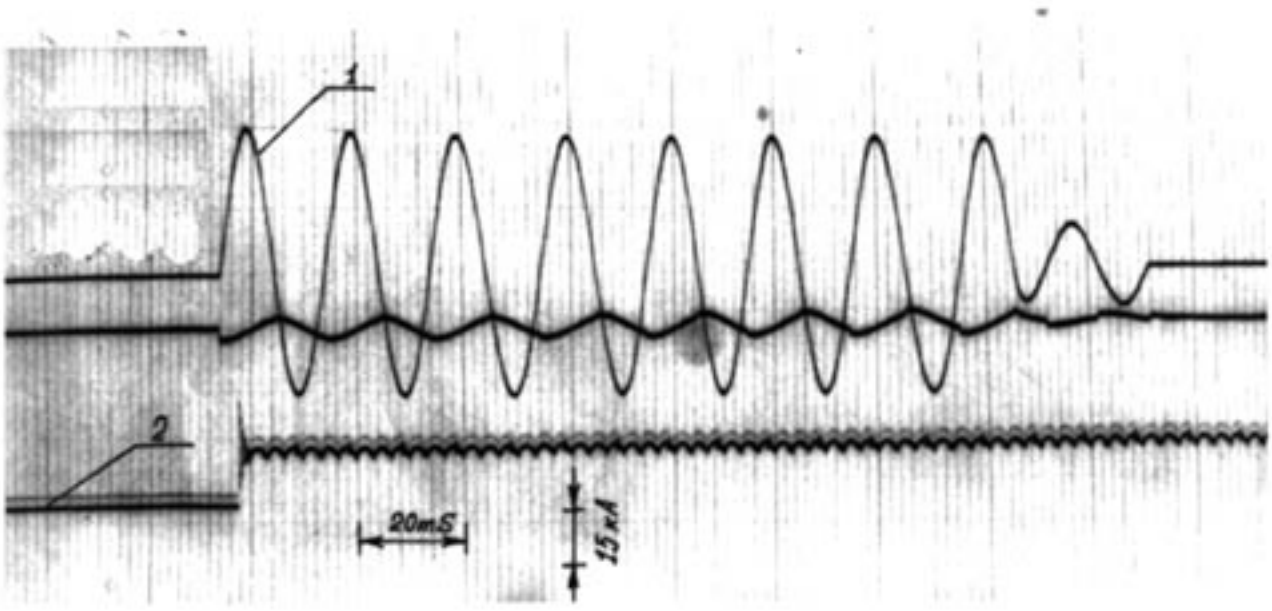

Fig. 2.44. Shot # 12 (I_{max}=36,9 kA, t=170ms, steel).
Arc current oscillogram: 1 is arc current, 2 is sinchrosignal

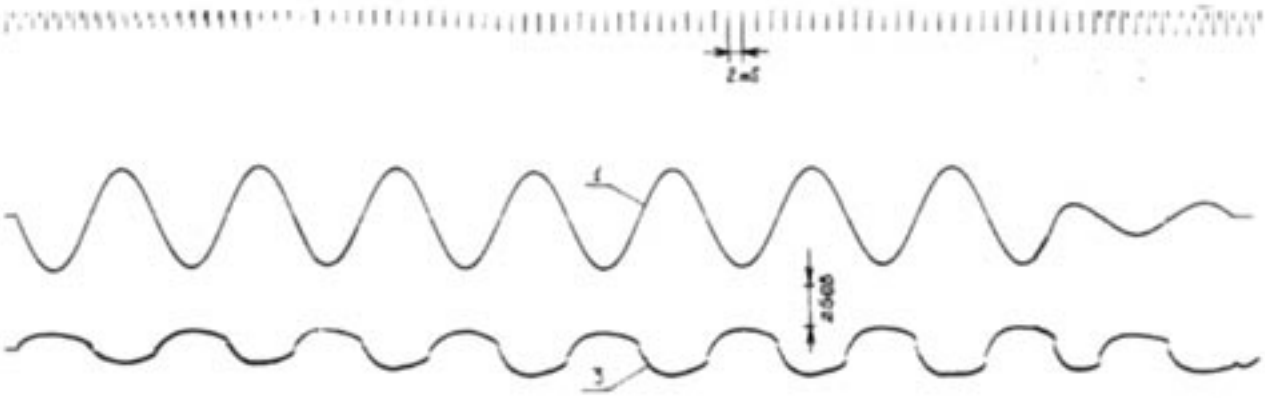

Fig. 2.45. Shot # 12 (I_{max}=36,9 kA, t=170ms, steel).
Arc voltage oscillogram: 1 is arc current, 3 is arc voltage

Fig. 2.46. Shot # 12 (I_{max}=36,9 kA, t=170ms, steel).
Picture of the cylinder region affected by the arc.

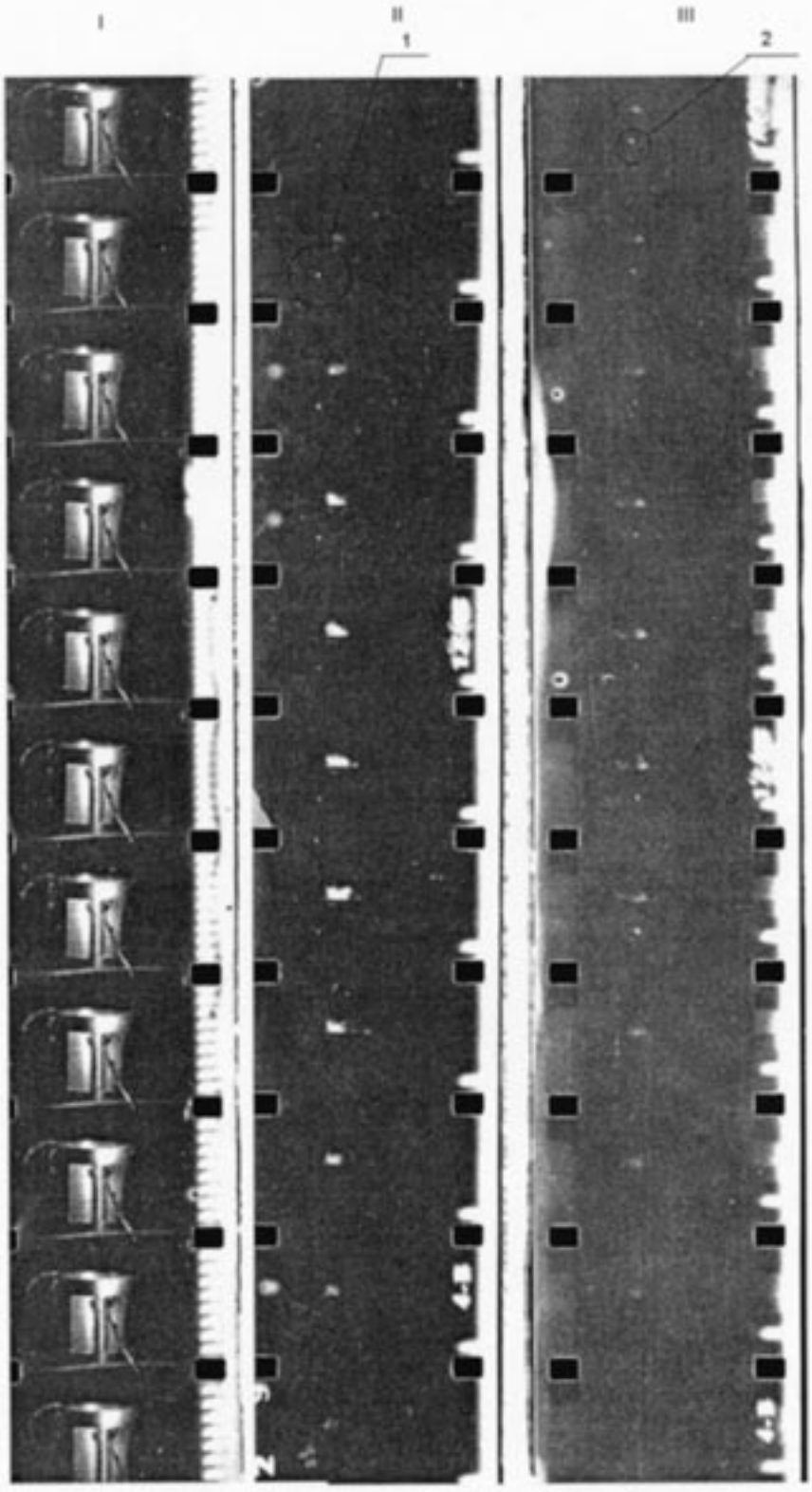

Fig. 2.47. Shot # 12 (I_{max}=36,9 kA, t=170ms, steel).

Motion picture record of the cylinder burning though process. Frame frequency is 1000 frames/s. The frame column I shows the cylinder before shot. The frame column II shows the beginning of the arc effect on the cylinder. Position 1 denotes the glow appeared at the time of the arc ignition. Frame column III show the process of hole formation and growth in the process of arc effect. Glow appearance (denoted by 2) results from hole formation in the cylinder hole. Time interval from the beginning of arc glow to hole formation is 125 ± 1 ms.

CHAPTER 3

Calculated estimation of electric arc thermal effect on metal shells

3.1. Theoretical model

3.1.1. To perform calculated estimation of electric arc thermal effect on metal shells, the initial problem geometry presented in Fig. 3.1, can be reduced to axissymmetrical (see Fig. 3.2), if to ignore the cylinder lateral surface curvature. It is quite permissible, since /1/

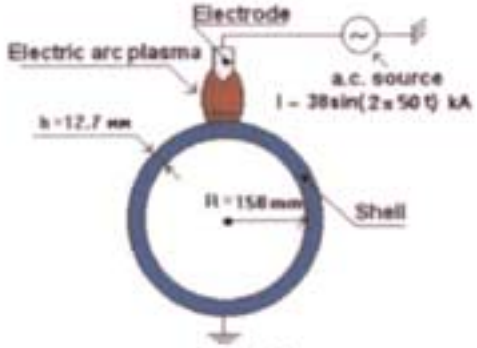

Fig. 3.1

$$h \ll R,\ \sqrt{\frac{k}{\rho c} t_q} \ll R,$$

where k,ρ,c are cylinder material heat conductivity, density and heat capacity, respectively, t_q is current duration.

In axisissymmetrical schematic of Fig. 3.2 only one way of heat delivery stands out i.e., source q, resulted by the heat flux from the arc channel zone. Volumetric heat sources may be neglected as is shown in /2/.

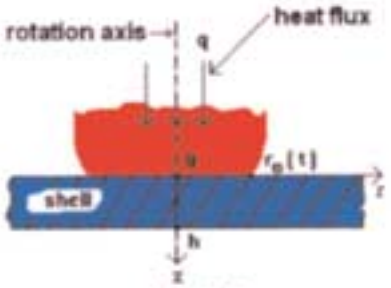

Fig. 3.2

Assume the following hypothesis about the nature of heat flux density distribution q over the radius within the electric arc channel zone (see Fig. 3.3) /3/:

- $q(r \in [0, r_0(t)]) = q_0 = \text{const}$ (3.1)
- $q(r) = q_m \exp(-\zeta^2 r^2 / r_0^2)$ (3.2)

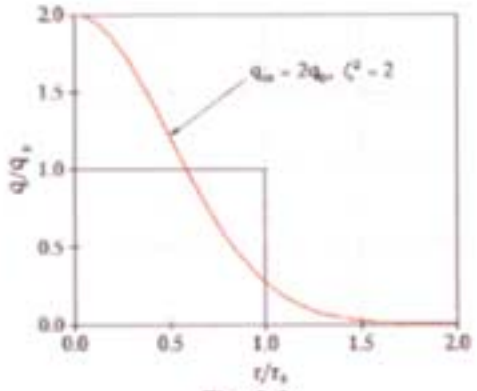

Fig. 3.3

The heat flux density within the center of the heat flux q_m and its concentration coefficient ζ are determined from the conditions of heat flux equality (3.1) and (3.2):

$$\int_0^{2\pi} d\varphi \int_0^{\infty} dr\ r q_m \exp(-\zeta^2 r^2 / r_0^2) = \pi r_0^2 q_0 \qquad (3.3)$$

i.e.

$$q_m = \zeta^2 q_0$$

Usually /3,4/ take $\zeta^2=2$, i.e.

$$q_m = 2q_0 \qquad (3.4)$$

According to the theory /5/ and experimental data /1,3,4/ the radius of the electric arc channel zone is subject to the ratio

$$r_0(t) = k_c\sqrt{|I(t)|}\ ,\ k_c = \text{const} \qquad (3.5)$$

It should be mentioned that q_0 and k_c depend on the shell material and polarity of the current flowing along the arc channel.

3.1.2. At currents characteristic for short closure (amplitude ≥10kA) almost the entire melted metal formed under the effect of the arc is removed as a result of sputtering affected by electric dynamic forces /1/.

For numerical calculations of one-D temperature distribution within a metal shell over the axis of the heat flux (see Fig. 3.2) it is possible to use a mathematical model developed in /2/:

$$\begin{cases} \rho\left(c + \lambda\delta\left(T - T_p\right)\right)\dfrac{\partial T}{\partial t} = \dfrac{\partial}{\partial z}\left(k\dfrac{\partial T}{\partial z}\right),\ z_o \le z \le h \\ T(z, t = 0) = T_o \\ -k\dfrac{\partial T}{\partial z} = q, \qquad z = z_o(t) \\ -k\dfrac{\partial T}{\partial z} = \mu\left(T - T_o\right), \quad z = h \\ z_o(t):\quad T\left(z_o(t), t\right) = T_b \\ z_o(t = 0) = 0 \end{cases} \qquad (3.6)$$

In the system (3.6) λ is shell material fusion heat (phase transition), T_p is fusion temperature, T_b is the temperature at which the melted metal is thrown out ($T_b \ge T_p$), μ is a heat exchange coefficient between the internal shell and air, z_0 is the current coordinate of the interface «arc plasma-shell» over the arc axis.

The first equation within the system (3.6) represents heat conductivity non-linear equation combined with the equation of interface motion /6,7/. The second ratio gives the initial, the third and the forth give boundary conditions. Two last ratios (3.6) give non-explicitly the equation of interface motion «arc plasma-shell».

In a finite-differential analogue (3.6) ejection of the melt is implemented by removal of point from a calculation grid in which $T \ge T_b$.

3.1.3. To resolve (3.6) the method of finite differences can be used.

Before building finite-difference analogue, let us make some simplifications. First of all, we shall ignore air heat exchange (μ=0).

Note: Calculations based on analytical methods, developed in /2/, show that the effect of heat exchange on the temperature distribution picture is insignificant at any times, if they are not significantly higher than the time of heat effect.

Second, we shall introduce new designations and change variables:

$$\begin{cases} c + \lambda\delta\left(T - T_p\right) \overset{def}{=} \tilde{c} \\ T \to U = T - T_o \\ U \to \upsilon(U) = \int_o^U \rho\tilde{c}\,dU \end{cases}$$

With these designations the system (3.6) relatively function υ looks the following way

$$\begin{cases} \dfrac{\partial\upsilon}{\partial t} = \dfrac{\partial}{\partial z}\left(a(\upsilon)\dfrac{\partial\upsilon}{\partial z}\right), \quad a(\upsilon) = \dfrac{k}{\rho\tilde{c}} \\ \upsilon(z, t=0) = 0 \\ -a(\upsilon)\dfrac{\partial\upsilon}{\partial z} = q, \qquad z = z_o(t) \\ \dfrac{\partial\upsilon}{\partial z} = 0, \qquad z = h \\ z_o(t): \ \upsilon(z_o(t), t) = \upsilon_b = \int_o^{\tau_b - \tau_o} \rho\tilde{c}\,dU \\ z_o(t=0) = 0 \end{cases} \tag{3.7}$$

3.1.4. We shall assume that τ is a step in time, d is a grid step, in this case absolutely stable finite-difference scheme for (3.7) is

$$\begin{cases} \dfrac{\hat{y}_i - y_i}{\tau} = \dfrac{1}{d}\left[a_{i+1}(y)\dfrac{\hat{y}_{i+1} - \hat{y}}{d} - a_i(y)\dfrac{\hat{y}_i - \hat{y}_{i-1}}{d}\right] \\ \hat{y}_i = y_i^{j+1}; \ y_i = y_i^j; \ a_i(y) = 0.5\left(a(y_{i-1}) + a(y_i)\right) \\ \left\{y_i^o = 0\right\}_{i=0}^N \\ \hat{y}_{i_o} = \hat{y}_{i_o+1} + \dfrac{qd}{a_{i_o}(y)} \\ \hat{y}_N = \hat{y}_{N-1} \\ i_0: \ \begin{cases} y_{i_o} \geq \upsilon_b \\ y_{i_o+1} < \upsilon_b \end{cases} \end{cases} \tag{3.8}$$

y_i^j in (3.8) is a finite-difference analogue of the function υ in the spatial point i across a time layer t_j, N is a number of grid points covering the range [0,h].

For (3.8.) solution we shall use the method of the right run.

If to introduce parameter $\gamma = \tau / d^2$ and deduce finite-difference analogues of heat conductivity and boundary condition equations to the canonical form:

$$A_i y_{i-1} - C_i y_i + B_i y_{i+1} = -F_i, \quad i = i_o + 1, N - 1$$
$$y_{i_o} = \chi_{i_o+1} y_{i_o+1} + \mu_{i_o+1}, \ y_N = \chi_2 y_{N-1} + \mu_2,$$

it is easy to build the calculation scheme:

$$
\begin{cases}
j = 0: \quad \{y_i^j\}_{i=0}^N = 0 \\
j > 1 \\
A_i = \gamma a_i(y^{j-1});\ C_i = 1 + \gamma\{a_i(y^{j-1}) + a_{i+1}(y^{j-1})\};\ B_i = \gamma a_{i+1}(y^{j-1});\ F_i = y_i^{j-1} \\
\alpha_{i_0+1} = \chi_{i_0+1} = 1;\ \beta_{i_0+1} = \mu_{i_0+1} = \dfrac{qd}{a_{i_0}(y^{j-1})} \\
\chi_2 = 1,\ \mu_2 = 0 \\
\overset{(\rightarrow)}{\alpha}_{i+1} = \dfrac{B_i}{C_i - \alpha_i A_i},\ i = i_0 + 1, N-1 \\
\overset{(\rightarrow)}{\beta}_{i+1} = \dfrac{A_i\beta_i + F_i}{C_i - \alpha_i A_i},\ i = i_0 + 1, N-1 \\
\hat{y}_N = \dfrac{\mu_2 + \chi_2\beta_N}{1 - \alpha_N\chi_2} \\
\overset{(\leftarrow)}{\hat{y}}_i = \alpha_{i+1}\hat{y}_{i+1} + \beta_{i+1},\ i = N-1, i_0 \\
i_0: \begin{cases} y_{i_0} \geq \upsilon_b \\ y_{i_0+1} < \upsilon_b \end{cases}
\end{cases}
\tag{3.9}
$$

3.2. Calculation data on temperature distribution within the shell of alloy B93

3.2.1.In calculations of temperature distribution within the shell of the alloy B93 having the thickness h=12.7mm we used λ and q_0(as an average according to the arc current period) known for aluminum /3,8/:

$$\lambda = 393488 \text{ J/kg};\ q_0 = 1.95 \cdot 10^8 \text{ W} / \text{m}^2.$$

Alloys do not have definite fusion temperature, fusion is characterized by the temperature of fusion beginning (solidus) and fusion end (liquidus). The data on alloy B93 are missing in literature, thus, we used in calculations the data for the alloy B95 (close to B93 in terms of composition) /8/:

$$T_p \in [477, 638]\ \text{C}$$

Various references /9,10,11,12,13/ give different data on temperature dependence of heat conductivity, heat capacity and density of alloy B93, thus in calculations we used the averaged data for k(T) and c(T) (see Table 3.1), density ρ was calculated by the formulae

$$\rho \approx \frac{\rho_o(T_o)}{1 + 3\alpha(T - T_o)},$$

where $\alpha = 26.8 \cdot 10^{-6} \text{C}^{-1}$ /9/, and $\rho_o = 2.84 \cdot 10^3 \text{ kg} / \text{m}^3$.

Table 3.1

T, C	k, $\frac{W}{m \cdot C}$	c, $\frac{J}{kg \cdot C}$	ρ, $10^3 \frac{kg}{m^3}$
20	-	795	2.84
25	163	-	-
100	167	879	2.82
200	172	963	2.80
300	167	1047	2.78
400	163	1130	2.76
500	-		2.73
600	-		2.71
700	-		2.69

3.2.2.Below Table 3.2 presents the data on the melting time for the shell of alloy B93 (t_p), performed at different conditions. Calculations were performed at τ=0.025ms, d=0.1mm. Time t_p was determined from the condition $T(z=h, t_p)=T_p$. The time of the heat source acting was not limited.

Table 3.2

λ, $\frac{J}{kg}$	q, $\frac{W}{m^2}$	T_p, C	T_b, C	t_p, s	hypothesis about q(r)
393488 393488	$1.95 \cdot 10^8$ $3.90 \cdot 10^8$	480 480	480 480	0.1543 0.0776	$q(r)=q_o$ $q(r) = 2q_o e^{-2r^2/r_q^2}$
0 0	$1.95 \cdot 10^8$ $3.90 \cdot 10^8$	640 640	640 640	0.1163 0.0584	$q(r)=q_o$ $q(r) = 2q_o e^{-2r^2/r_q^2}$

It is seen from the Table 3.2 that the results of one-dimensional calculations significantly depend on the hypothesis about the density distribution nature of the heat flux along the radius within the arc zone (see (3.1) and (3.2)). Apparently, this is the result of the fact that if the current is ≥10kA the entire melted mass affected by electric dynamic forces practically instantly is removed from the arc channel zone. Melting process becomes quicker, thus two times difference in the heat flux density along the arc channel results in the same difference in melting time. In this connection the works /3/ and /4/ should be noted, which qualify that at low currents calculations using hypothesis about uniform and gaussian flux q distribution provide difference in melting time about 10-20%.

The next important result which can be concluded from comparison of Table 3.2 and the experimental data (section 2) is the following: the use in heat calculations phase transition heat (λ) for alloys is unreasonable.

a) heat calculations for alloys are necessary to be performed at the zero heat of the phase transition;

b) when choosing the heat flux density across the axis of the arc channel zone for one-D calculations it is necessary to take the doubled average flux q_o (corresponding to the Gaussian distribution $q(r) = 2q_o e^{-2r^2/r_o^2}$ at $r=0$).

3.2.3. Below the pictures 3.4-3.7 show the plots of temperature distribution, obtained at variations of t_q (time of heat flux action).

Al the calculations have been performed in accordance with p.3.2.2.1. at $\lambda=0$ and $q = 2q_o = 3.9 \cdot 10^8 \, W/m^2$.

Fig. 3.4 presents temperature dynamics at the inner side of the shell ($T(z=h,t)$) depending on time.

It should be noted that t_q=0.0584s corresponds to the shell melting time, when the heat source act on a continuous basis, the other t_q=0.04672s and t_q=0.03504s are decreased by 20% and 40 %, respectively from the value t_q=0.0584s.

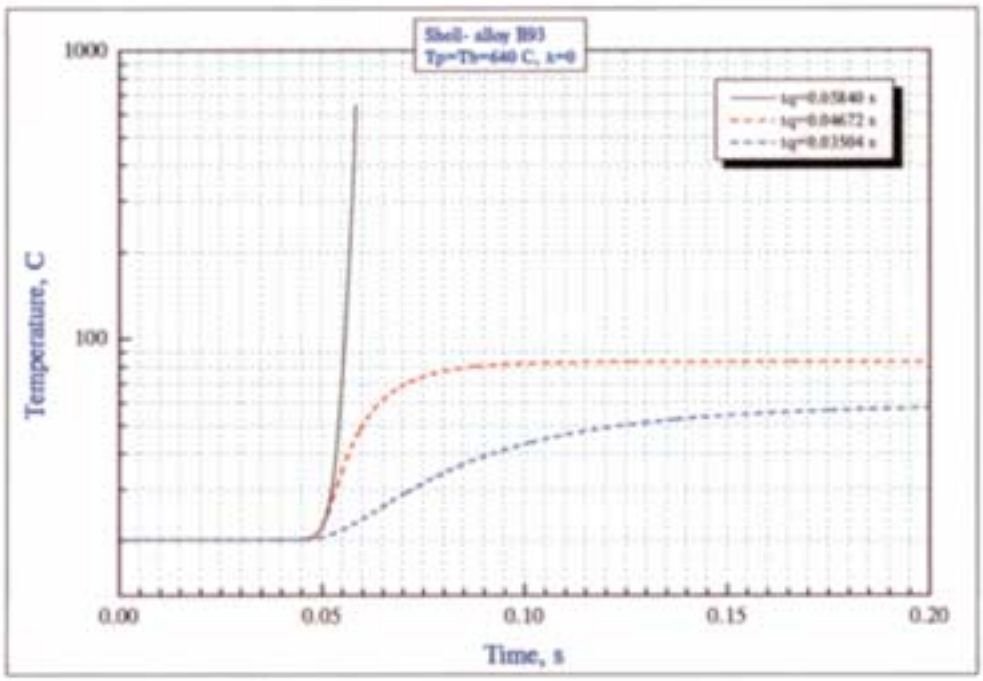

Fig. 3.4

Fig. 3.5, 3.6, 3.7 show temperature distributions over the shell cross section at various times for three cases: for t_q=0.0584s, t_q=0.04672s and t_q=0.03504s, respectively.

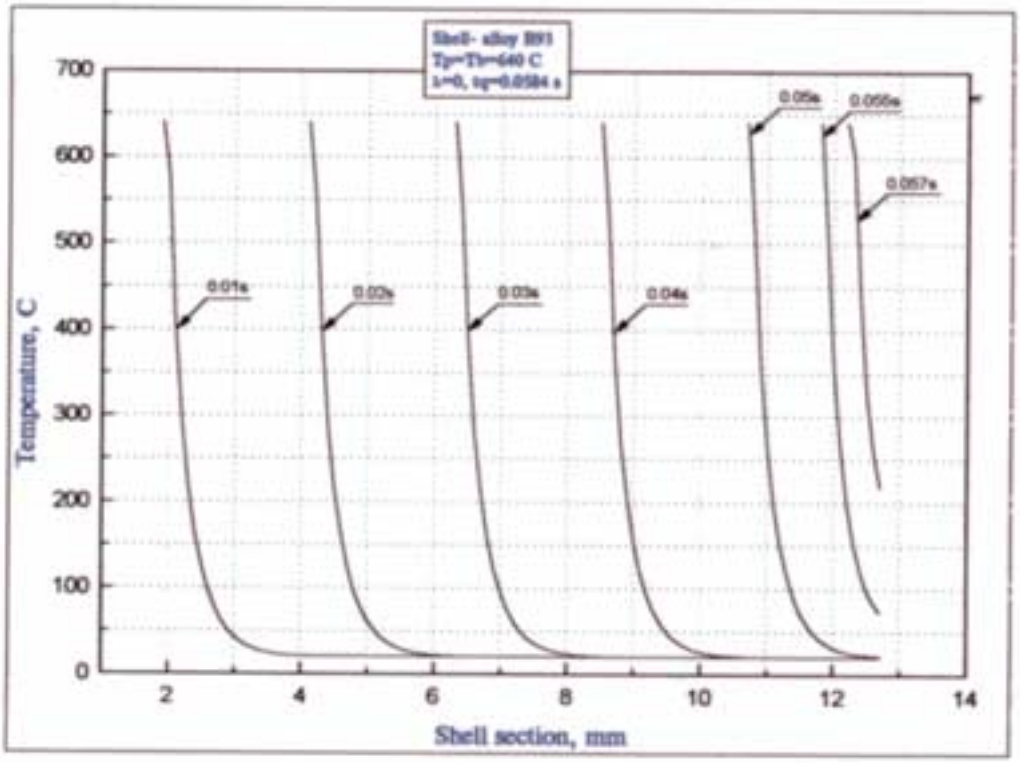
Shell- alloy B93
Tp=Tl=640 C
λ=0, tg=0.0584 s
0.05s
0.055s
0.057s
0.01s
0.02s
0.03s
0.04s
Temperature, C
Shell section, mm

Fig. 3.5

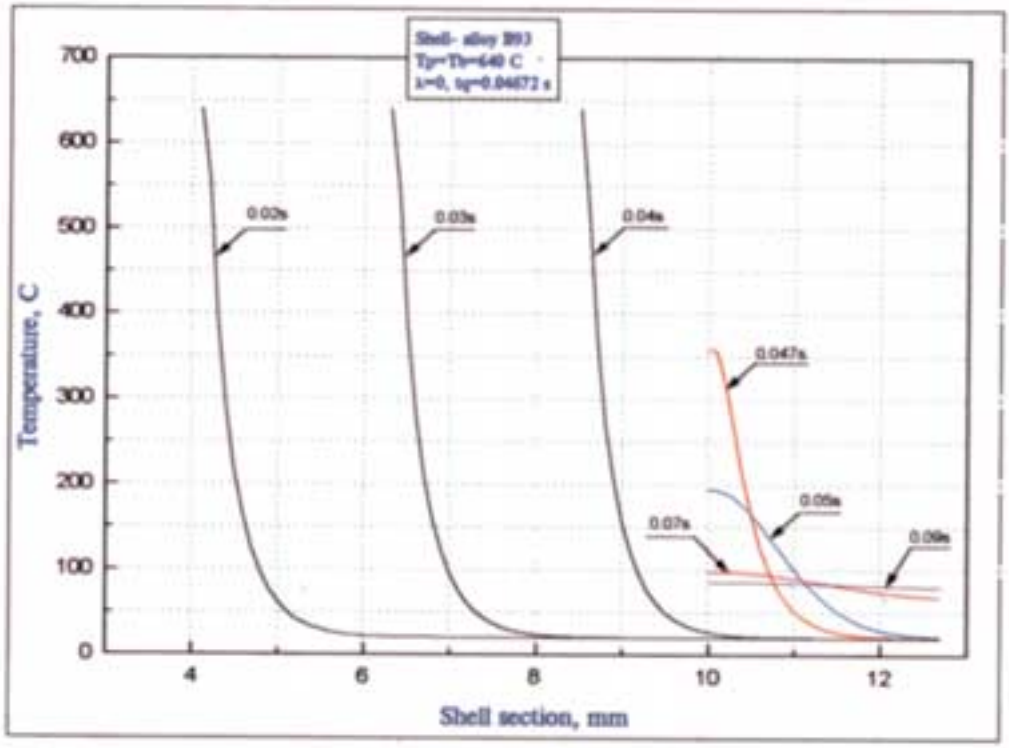
Shell- alloy B93
Tp=Tl=640 C
λ=0, tg=0.04672 s
0.02s
0.03s
0.04s
0.047s
0.05s
0.07s
0.09s
Temperature, C
Shell section, mm

Fig. 3.6

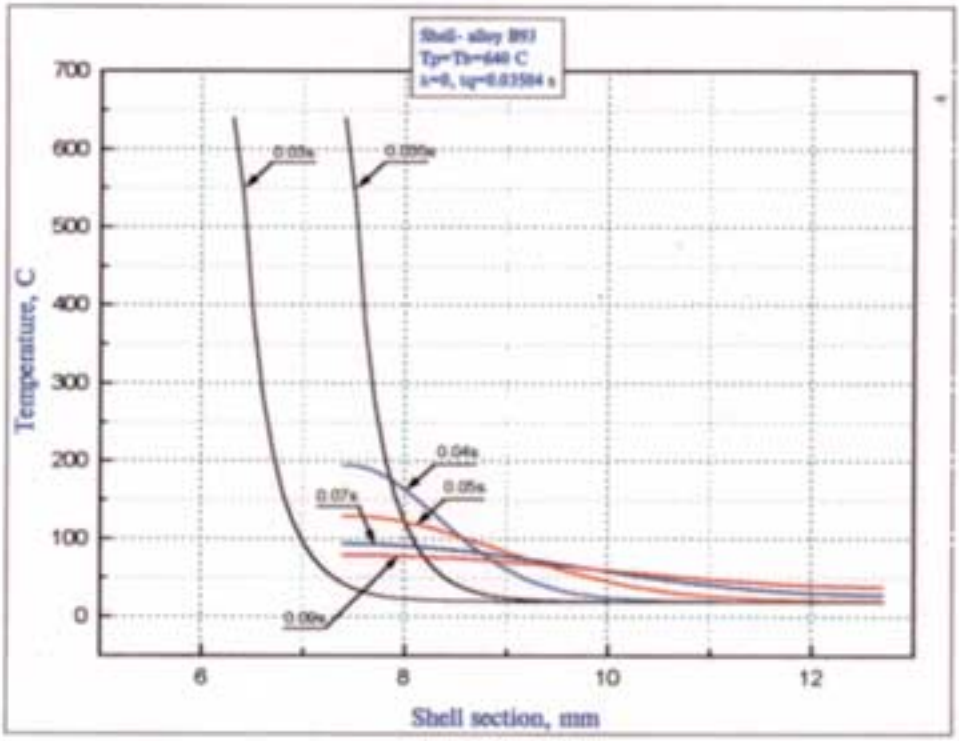

Fig. 3.7

3.3. Calculation data on temperature distribution within the steel shell 12X18H10T

3.3.1. In the calculations on temperature distribution within the steel shell 12X18H10T having the thickness h=12.7mm we used q_0 (as an average over arc current period) for steel St-3/3/:

$$q_o = 1.7 \cdot 10^8 \, W / m^2.$$

In accordance to the references the melt ending temperature (liquidus) of the steel 12X18H10T is 1400C /8,14/.

Temperature dependencies of heat physical characteristics for the steel 12X18H10T are known only for heat conductivity, that is why heat capacity and density within the range $[T_o, T_p]$ were set as constant (see Table 3.3)

Table 3.3

T, C	k, $\frac{W}{m \cdot C}$	c, $\frac{J}{kg \cdot C}$	ρ, $10^3 \frac{kg}{m^3}$
20	-	502.32	8.05
26.85	15.1	-	-
326.85	19.8	-	-
626.85	26.6	-	-
826.85	27.8	-	-

3.3.2. Below Table 3.4 shows the data on the melting time for the shell of steel 12X18H10T (t_p), performed under various conditions; calculations were made at τ=0.025s, d=0.1mm. The time t_p was determined from the condition $T(z=h, t_p)=T_p$=1400C. Heat flux effect time was not limited.

Table 3.4

$\lambda, \frac{J}{kg}$	$q, \frac{W}{m^2}$	T_p, C	T_b, C	t_p, s	hypothesis about q(r)
0	$1.7 \cdot 10^8$	1400	1400	0.4199	$q(r)=q_o$
0	$3.4 \cdot 10^8$	1400	1400	0.2105	$q(r) = 2q_o e^{-2r^2/r_o^2}$

3.3.3 Below Fig. 3.8-3.10 show the plots of temperature distribution, obtained when varying t_q (heat flux effect time). All the calculations were performed at λ=0 and $q = 2q_o = 3.4 \cdot 10^8 W/m^2$.

Fig. 3.8 shows temperature dynamics across the inner shell side (T(z=t,h)) depending on time. The time t_q=0.2105s corresponds to the time of shell melting at the continuous heat source effect, t_q=0.1684s is time decreased by 20% from t_q=0.2105s.

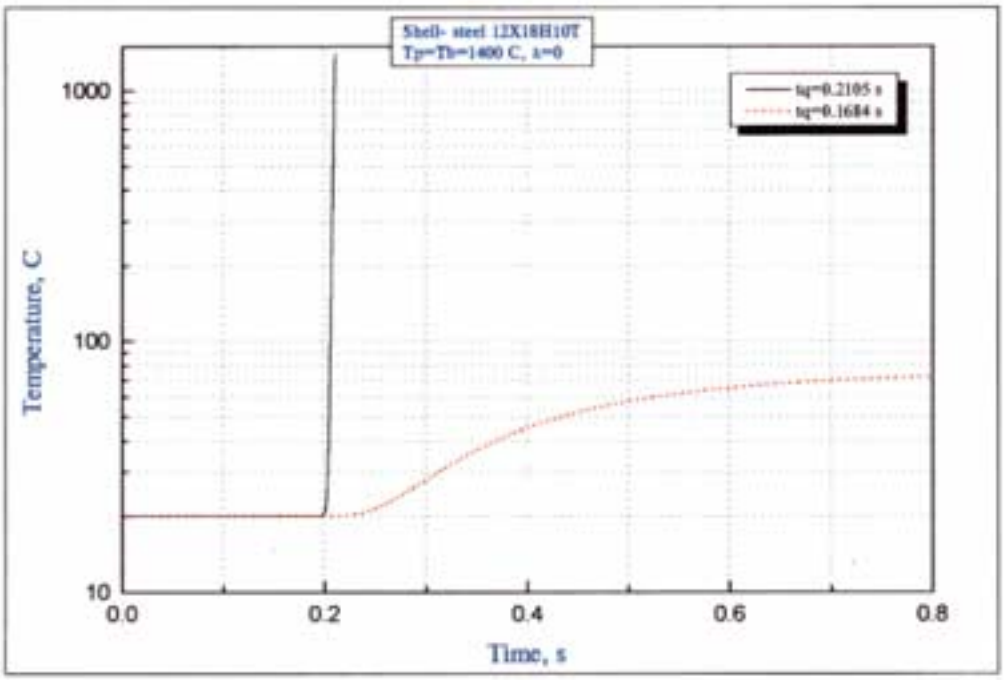

Fig. 3.8

Fig. 3.9 and 3.10 show temperature distribution over the shell section at different times for the case t_q=0.2105s and t_q=0.1684s, respectively.

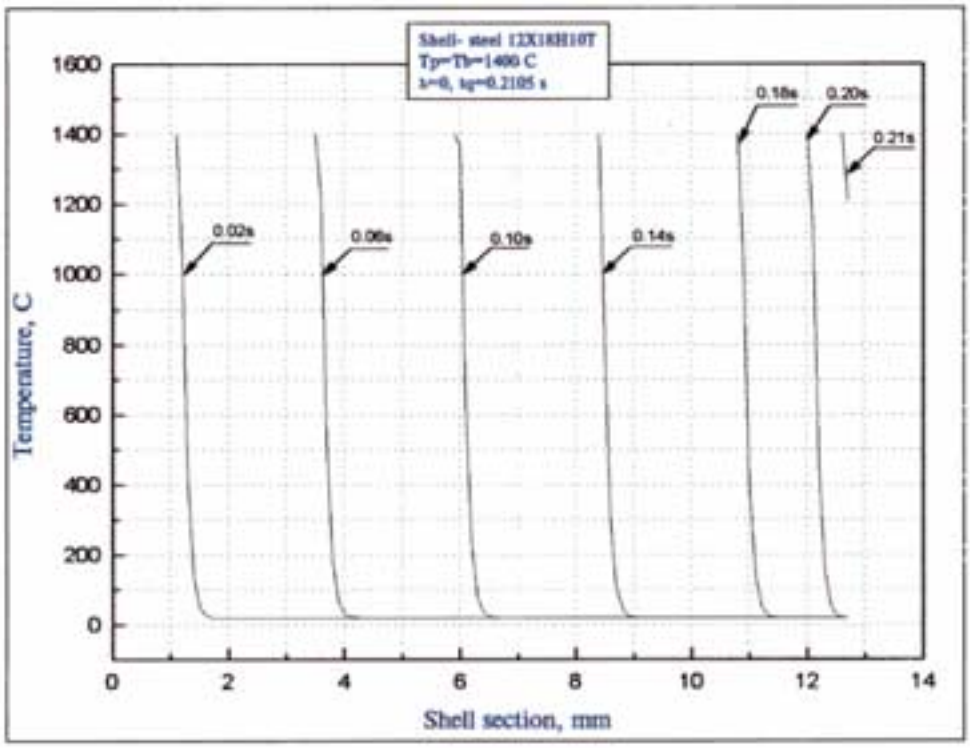

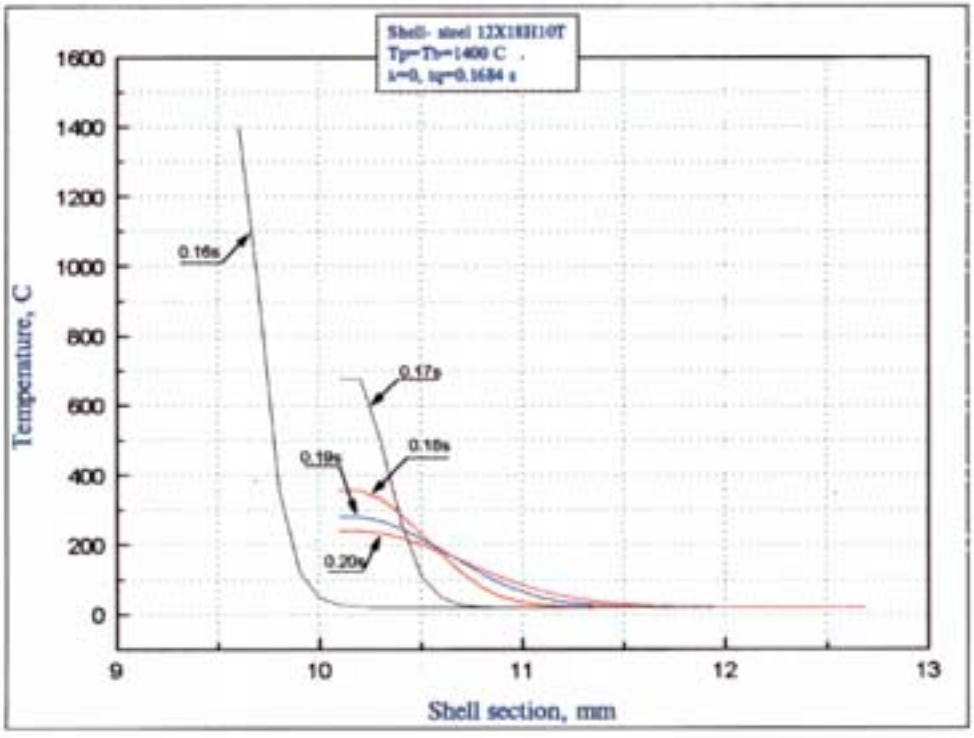

Fig. 3.10

CHAPTER 4

Data discussion

4.1. Experiments

The experiments prove that the localized arc of the shorted current in the supply line can be very destructive.

When the amplitude current value is $I_{max} \approx 37kA$, the time of through hole formation in the cylinder made of aluminum alloy having a wall thickness of ≈13mm is ≈50ms, in the steel cylinder of the same thickness it is ≈130ms. The experiments confirm the hypothesis expressed in /15/ that the hole formation time does not has a strong dependence on the current amplitude. At currents of $I_{max} \approx 37kA$ and $I_{max} \approx 19kA$ approximately the same minimum times of hole formation in the aluminum cylinder were measured. However, it should be noted that at a current of $I_{max} \approx 19kA$ in some experiments we measured the hole formation time significantly higher (in the shots #5 and #6 times were of ≈80 and ≈90ms, respectively).

Arc voltage in the experiments is 100V and less for aluminum cylinders and 165V and less for steel. This indicates that a high current arc may burn in the distributing mains of low voltage. We also measured that the arc voltage gradually increases in the process of action. This fact can be explained by gap increase between the electrode and the shell as a result of erosion from the arc.

Temperature measurements of the inner cylinder surface show that if a through hole is not formed, the temperature of inner walls remain low. The experiments did not measure the temperature higher than 200C.

4.2. Theoretical models

The report presented some estimates on the theoretical model, proposed and justified in /2/. Calculations showed that in the model when using the hypothesis on heat flux distribution according to the formulae $q(r) = 2q_o e^{-2r^2/r_o^2}$ the calculated and experimental data have a good agreement. The calculated time of burning through the aluminum cylinder is ≈58ms, the experimental result is 48ms. The calculated time in case of steel cylinder is 210ms, the experimental time is from 130ms to 140ms. Taking into account that thermal properties of cylinder materials as well as the heat fluxes from arc zone are known roughly (primarily it concerns steel cylinders), the agreement should be interpreted as satisfactory.

REFERENCES

1.Г.В. Буткевич и др. Электрическая эрозия сильноточных контактов и электродов. М., Энергия, 1978.

2.Electric Arc Effect On Explosive Safety (contract AV-5840), Document 0613OTN8-98, 1998

3.Н.Р.Абрамов, И.П.Кужекин, В.П.Ларионов, Характеристики проплавления стенок металлических объектов при воздействии на них молнии, Электричество, N 11, 1986.

4.Н.Р.Абрамов, Расчет теплового воздействия канала молнии на металлические объекты, Изв. АН СССР, Энергетика и транспорт, N1, 1986.

5.Ю.П. Райзер, Физика газового разряда, М., Наука, 1987.

6.А.Н.Тихонов, А.А.Самарский, Уравнения математической физики, М., Наука, 1977.

7.А.А.Самарский, Теория разностных схем, М., Наука, 1977.

8.Таблицы физических величин, Справочник под ред. И.К.Кикоина, М., Атомиздат, 1986.

9.Промышленные деформируемые, спеченные и линейные алюминиевые сплавы, под ред. Ф.И.Квасова и И.Н.Фридляндера, М., Металлургия, 1972.

10.Справочник по авиационным материалам под ред. А.Т.Туманова, т.2, ч.1, М., Машиностроение, 1965.

11.Авиационные материалы, Справочник, т.4, Алюминиевые и бериллиевые сплавы, ч.1, Деформируемые алюминиевые сплавы и сплавы на основе бериллия, кн.2, под ред. Р.Е.Шалина, М., ОНТИ, 1983.

12.Теплопроводность твердых тел, Справочник под ред. А.С.Охотина, М., Энергоатомиздат, 1984.

13.В.С.Чиркин, Теплофизические свойства материалов, М., Г из-во физ. мат. лит., 1959.

14.Физические величины, Справочник под ред. И.С.Григорьева и Е.З.Мейлихова, М., Энергоатомиздат, 1991.

15.Electric Arc Effect On Explosive Safety (contract AV-5840), Document 0613OTN3-98, 1998

Distribution

1	MS0319	S. D. Nicolaysen, 2613
1	MS0405	M. P. Bohm, 12333
1	MS0491	J. P. Hoffman, 12345
1	MS0428	D. D. Carlson, 12300
1	MS0492	D. R. Olson, 12332
15	MS0492	D. H. Loescher, 12332
1	MS0836	D. Dobranich, 9116
5	MS1213	R. E. Smith, 5328
1	MS9405	L. A. Bertram, 8728
1	MS9018	Central Technical Files, 8945-1
2	MS0899	Technical Library, 9616
1	MS0612	Review and Approval Desk, 9612 for DOE/OSTI